INSTITUTO TECNOLÓGICO DE AERONÁUTICA



Luis Felipe Silva Rezende Soares

EXTENDED STARING SPOTLIGHT - A NEW SAR METHOD OF ACQUISITION VIA CONCURRENT IMAGING

Final Paper 2025

Course of Electronic Engineering

Luis Felipe Silva Rezende Soares

EXTENDED STARING SPOTLIGHT - A NEW SAR METHOD OF ACQUISITION VIA CONCURRENT IMAGING

Advisor

Prof. Dr. Renato Machado (ITA)

Co-advisor

João Pedro Turchetti Ribeiro (KIT)

ELECTRONIC ENGINEERING

São José dos Campos Instituto Tecnológico de Aeronáutica

Cataloging-in Publication Data

Documentation and Information Division

Soares, Luis Felipe Silva Rezende

Extended Staring Spotlight - A new SAR method of acquisition via Concurrent Imaging / Luis Felipe Silva Rezende Soares.

São José dos Campos, 2025.

111p.

Final paper (Undergraduation study) — Course of Electronic Engineering—Instituto Tecnológico de Aeronáutica, 2025. Advisor: Prof. Dr. Renato Machado. Co-advisor: João Pedro Turchetti Ribeiro.

- 1. Radar. 2. SAR. 3. Imaging. 4. Acquisition. I. Instituto Tecnológico de Aeronáutica.
- II. Extended Staring Spotlight A new SAR method of acquisition via Concurrent Imaging.

BIBLIOGRAPHIC REFERENCE

SOARES, Luis Felipe Silva Rezende. Extended Staring Spotlight - A new SAR method of acquisition via Concurrent Imaging. 2025. 111p. Final paper (Undergraduation study) – Instituto Tecnológico de Aeronáutica, São José dos Campos.

CESSION OF RIGHTS

AUTHOR'S NAME: Luis Felipe Silva Rezende Soares

PUBLICATION TITLE: Extended Staring Spotlight - A new SAR method of acquisition via Concurrent Imaging.

PUBLICATION KIND/YEAR: Final paper (Undergraduation study) / 2025

It is granted to Instituto Tecnológico de Aeronáutica permission to reproduce copies of this final paper and to only loan or to sell copies for academic and scientific purposes. The author reserves other publication rights and no part of this final paper can be reproduced without the authorization of the author.

Luis Felipe Silva Rezende Soares Rua H8E, Ap. 206 12.228-461 – São José dos Campos–SP

EXTENDED STARING SPOTLIGHT - A NEW SAR METHOD OF ACQUISITION VIA CONCURRENT IMAGING

This publication was accepted like Final Work of Undergraduation Study Luis Felipe Silva Rezende Soares Author Renato Machado (ITA) Advisor João Pedro Turchetti Ribeiro (KIT) Co-advisor

For the Lord, my family and my friends. How amazing it is, to live life alive!

Acknowledgments

To God, for bringing me life, health, wisdom, and my family - in hoc signo vinces.

Then, my parents - Marcelo and Jozaine - and my sister - Ana Flávia - for never doubting me, not even for a single second, and for loving me, in such a way that I never doubted that every second was the most precious there was, until the next one.

Meine Schwester, Valquíria, for trailing all paths alongside me for so long. For being one of the cornerstones of my life, the tail to my head of the coin.

My godfather, Jaques, whose support was absolutely fundamental for this thesis to even exist.

To all friends I made during these years at ITA - and may God let these bonds never erode over time, but strengthen brighter as age flies by.

I'd also like to acknowledge the immense gratitude towards Prof. Dr. Alberto Moreira for the unique opportunity of producing this thesis in the *Deutsches Zentrum für Luft-und Raumfahrt*, in Oberpfaffenhofen, working alongside some of the finest minds in the entire world and having my chance to push, even if for a few humble inches, the field of SAR technology forward. I extend this gratitude to Herr Manfred Zink for selecting me for the position, and to my Bachelor's supervisor Prof. Dr. Renato Machado for the suggestion to attend DLR, years earlier.

And finally, I would like to thank all my peers and colleagues of my research team in DLR - Herr Thomas Kraus and Herr Markus Bachmann - for their invaluable comments and suggestions, but most importantly, I'd like to thank my supervisor, friend, and soon-to-be Dr. João Turchetti, for giving me the freedom to explore and research, while supporting me with top-tier expertise - the field of SAR is well served with a one-of-a-kind engineer.

While hard to finally leave ITA and H8 behind, I do so gratefully.

Because the man who wastes his days dreading the arrival of the night shall never smile to a single sunset.



Resumo

No campo de Radares de Abertura Sintética (SAR), o uso dessa tecnologia para aquisição de imagens detalhadas da superfície da Terra sempre esteve limitado a uma restrição em particular – a conversão entre máxima área obtenível e a mais precisa resolução possível. Técnicas como ScanSAR conseguem extrair amplos trechos de terra ao custo da degradação significativa da resolução de imagem, ao passo que outras como Staring Spotlight entregam imagens detalhadas com área extremamente limitada. Mediante uso de uma nova técnica de emissão de pulsos – o Imageamento Concorrente – esta tese propôs e comprova a possibilidade prática do Staring Spotlight Estendido (Extended Staring Spotlight - EST): um novo modo de aquisição o qual é capaz de entregar o dobro da área de um imageamento convencional realizado por Staring Spotlight, enquanto mantém seu alto nível de detalhamento de imagem.

Abstract

Within the field of Synthetic Aperture Radar (SAR), its use for acquiring detailed images on Earth's surface has always been constrained by a particular trade-off - the one between maximum obtainable area and finest possible resolution. Techniques such as ScanSAR can achieve wide swaths of land but degrading significantly image resolution, while other methods such as Staring Spotlight yield detailed images with extremely limited surface area. With the usage of a novel pulse emitting technique - Concurrent Imaging - this thesis proposed and proves the feasibility of the Extended Staring Spotlight (EST): a new acquisition mode which yields double the size of a conventional Staring Spotlight scene, while maintaining its high-level of detail throughout the image.

List of Figures

FIGURE 1.1 –	General trend for the trade-off between resolution and scene area. The Spotlight mode extracts higher resolution of the image at the cost of scene size, while Stripmap provides broader coverage and worse image resolution. The resolution used is not technical, just a conceptual notion for quality and image definition	21
FIGURE 1.2 -	Depiction of both Stripmap (SM) and Staring Spotlight (ST) modes in action. The first mode (SM) has the antenna fixed at a particular angle (usually zero) at all times, leading to a broader image size but less time of illumination of any particular point on the ground. The second mode (ST) has the antenna being steered in such a way that the beam center always points towards a rotation center (C), which in the case of ST is on the center of the scene we wish to acquire. This reduces the <i>azimuth</i> length of the image acquired, but all points are illuminated during the entire movement of the platform, which itself boosts resolution. If C was geometrically below the ground, however, it would be a <i>Sliding Spotlight</i> (SL), being an intermediate case between SM and ST in both scene size and resolution	22
FIGURE 1.3 –	Depiction of the Extended Staring Spotlight mode (EST) proposed in this thesis. By leveraging Concurrent Imaging, one can synthesize two acquisitions, each done respectively in ST and towards their respective scene centers. By doing so, we double the length of the image in the azimuth direction, whilst keeping the resolution of ST	20
FIGURE 2.1 –	acquisitions throughout the whole picture	23
	demning a plane that is perpendicular to the direction of propagation.	40

LIST OF FIGURES x

FIGURE 2.2 –	Irradiation diagram of an antenna element (Two-Way - the wave travels forth and back to the equipment). The intensity is measured for every angle with respect to the boresight direction - the maximum intensity direction. The intensity pattern follows the trend of lobes - the Main Lobe, the first Side Lobes, the second Side Lobes, and so on	33
FIGURE 2.3 –	Array of irradiators linearly spaced by a physical distance of δ . Each irradiator with index k is fed by a specific current $I_k = \Gamma_k \cdot e^{j(\phi_k)}$. When all are applied to the array antenna simultaneously, a composite electric field is generated by the vector sum of all individual electric fields. This final field is the one used to illuminate a specific direction by the antenna.	35
FIGURE 2.4 –	Irradiation diagram of an antenna array, which points in a direction of $+1.0^{\circ}$ the element's maximum power direction (called <i>boresight</i> , in blue), the original radiation diagram of a single radiating element (in orange), and the multiplicative factor of the <i>Array Factor</i> (in green), which is applied throughout the radiator's diagram	38
FIGURE 2.5 –	Irradiation diagram (in blue) for the same antenna array of Fig. 2.4, but with a pointing angle of $+2.2^{\circ}$. Note how the array gain displays two power peaks: one at $+2.2^{\circ}$ (our intended direction) and -2.2° . This other power peak is unintended, as it's called a Grating Lobe - a byproduct of the shift in pointing angle, which shifts the array factor curve (in green) to the right, being modulated in value by the element irradiation diagram (in orange)	39
FIGURE 2.6 –	Diagram of a conventional radar's $Echo\ Window$. Pulses are transmitted (\mathbf{Tx}) , with a width of τ_p , periodically in a time interval of PRI. During this interval, no signal is sent to accommodate received signals (\mathbf{Rx})	41
FIGURE 2.7 –	Depiction of the emission of pulses from source O. Two wavefronts are highlighted, with points T_1 and T_2 both collinear to O. τ_p is the temporal width of the pulse emitted (in blue), and d the spatial distance between T_1 and T_2 . If d is too small, both points would be mapped by the same pulse, within the same τ_p , being indistinguishable from each other. Hence, there must be a minimal distance between the two points (radially) for them to be resolved as two	40
	separate points, and not mistakenly interpreted as the same one.	48

LIST OF FIGURES xi

FIGURE 3.1 –	Acquisition of a SLAR system. The platform moves with a constant velocity V_s and its direction of movement is the azimuth direction. It has embedded within it an antenna, of horizontal and vertical apertures of L_a and W_a respectively. The beam footprint of the antenna pulses (in red) has a near-range (\mathbf{N}) and a far-range (\mathbf{F}) extremes, as well as the scene center (\mathbf{C}). The distance between \mathbf{N} and \mathbf{F} is called the Swath Width (\mathbf{SW}) and A_L is the azimuth length of the footprint. Finally, R_0 is the slant range of the scene and $\theta_r \approx \frac{\lambda}{W_a}$ is the angular beam with in the range direction, with β standing for the elevation angle between the slant range and nadir. The grey plane is defined by the azimuth direction and the range	
	direction	52
FIGURE 3.2 –	Elevation geometry of pulse spread	53
FIGURE 3.3 –	Beam footprint under the resolvability grid of the acquired image	56
FIGURE 3.4 –	Resolvability under the resolution grid - two objects not sufficiently apart from one another in one direction will not be resolved	57
FIGURE 3.5 –	Schematic of a SAR/SLAR acquisition, with \mathbf{C} as scene center and \mathbf{P} as particular point of interest, at the same range but x apart from it in the azimuth direction, forming an angle of α_p in along-track. $v_{s,c}$ and $v_{s,p}$ are the components of velocity v_s seen from \mathbf{C} and \mathbf{P} respectively, with R_0 being the slant range at maximum proximity of the platform with \mathbf{C} and $R(t)$ the slant range of \mathbf{P}	58
FIGURE 3.6 –	Effect of reflected power from ambiguities (in blue) on the image of the focused scene (in red). These specific spots on the ground are positioned as such that their signals will overlap with the main scene's signal, leading to a degraded image. If the Ambiguity-to-Signal Ratio (ASR) is too high, the extract data is deemed not suitable and it is discarded. The darker pixels in the grid represent the ambiguities effect on the image extracted of the target scene - all should be red, but other blue scenes on the ground leak into the main scene, mixing with it and making it purple	63
FIGURE 3.7 –	Depiction of a satellite transmitting a train of pulses to points P, Q and T, in elevation. Point T is the acquisition target, since it is illuminated by the main lobe (in red). The train of pulses is colored such that the first transmitted pulse is red, the second is blue and the third is green. The satellite travels in azimuth, entering the	
	paper plane	64

LIST OF FIGURES xii

FIGURE 3.8 –	Reflected trains of pulses. The train of P is advanced in one pulse related to T, while T is advanced in two pulses from Q. The circles show how these signals will now arrive in S at the same time, so it will have the reflected signals of P, T and Q mixed	64
FIGURE 3.9 –	Depiction of the emergence of frequency shifting due to the Doppler Effect. All points on the ground which are not coincident to C will experience a different signal frequency due to the movement of the platform. In particular, some specific points $(A := \{A_k\}, k \in \mathbb{Z}^* will experience a shifted frequency which, when processed back to the satellite, will be processed as the same frequency as the target's (center C). These points are call Azimuth Ambiguities$	67
FIGURE 3.10	Stripmap acquisition depiction - the antenna keeps steered at a particular solid angle, never changing its squint	70
FIGURE 3.11 -	Depiction of a Staring Spotlight acquisition, where the antenna keeps steering towards a particular landscape in spite of the movement of the platform	72
FIGURE 3.12 -	Geometry of a Staring Spotlight acquisition, in function of the steering limit angles	73
FIGURE 4.1 –	When acquiring two consecutive ST images, the satellite needs to steer completely within its steering angle range, and only when it is finished doing so, it can point frontward to the next scene, with the same starting angle as the first scene. This inevitably leaves a gap Δ_{az} between both scenes	77
FIGURE 4.2 –	Possible consecutive acquisition of two ST images. The satellites now travel a narrow path during the illumination of a specific scene before imaging the next one, which heavily impacts resolution	77
FIGURE 4.3 –	Usual acquisition of a desired scene. All pulses emitted are following the schedule of one, and one one, acquisition mode. In the case of Stripmap, all pulses are emitted at a fixed antenna angle, while for Spotlight all pulses are emitted focusing on one, and only one, scene center	79
FIGURE 4.4 –	Representation of a dual acquisition. Instead of mapping solely one scene with all the available pulses, the hardware sends interleaved pulses - one towards C_1 and one towards C_2 - being then doable to acquire two scenes at the same time	80

LIST OF FIGURES xiii

FIGURE 4.5 –	Concurrent acquisition of two Staring Spotlight modes. The scenes 1 and 2 (red and blue) are juxtaposed azimuth-wise, but maintaining the same elevation angle. Note how scene 1 and scene 2 receive pulses in an interleaved manner. The beams from earlier and later positions of the platform were drawn less vibrantly to avoid pollution.	83
FIGURE 4.6 –	Image depicting the emergence of Nadir beams. Since pulses propagate in spherical wavefronts, they will hit the ground in all available positions, regardless of gain. In the case of Nadir beams, they are the first to return to the system, but since their incidence angle is so low, most of the energy emitted is transmitted back with the Rx pulse, in spite of the low gain associated with it	87
FIGURE 4.7 –	Diagram of a transmission pulse schedule and its echo window. The blue rectangle corresponds to the transmitted pulse, with a duty cycle of 18% and PRF=6000 Hz, the large indigo rectangle accounts for the received signal from a scene on the ground, and the narrow purple rectangle is the Nadir received pulse. The Rx pulse doesn't overlap with the transmission pulse, and Nadir does not overlap with the Rx pulse as well, aside from the tail-end τ_p (dashed line), which is dismissed in pulse compression	88
FIGURE 4.8 –	Timing Diagram of availability of scene acquisition for a given pair of (θ_i, PRF) , stretching from 15° to 60° of incidence angle and 1000 Hz to 6500 Hz of PRF. The red lines represent the pairs where there will be Nadir interference, while the green lines do the same but for the Tx Interference. Any blank space is a valid zone to start a conventional imaging technique, from a timing perspective alone. Notice the distortion around 34° - this is the region of higher terrain on the ground, such as Mount Everest. This simulation is a proof of concept only, as conventional mountains would not distort the diagram this much. We use a proof-of-concept topographic model of Earth, where terrain variations such as mountains are present, with an ellipsoidal approximation of the WGS84 computational model of the planet	89
FIGURE 4.9 –	Transmission diagram of a EST acquisition. Both scenes have a 5 km swath width, acquired at an incidence angle of $\theta_i = 37^{\circ}$, with PRF=3000 Hz and 9% duty cycle for each Tx pulse. There are no Tx nor Nadir pulses overlapping with any receiving signals, and each pulse is locked within a echo window. Each mode has an echo	09
	window that occupies 50% of the PRI (aside from the Tx Pulses)	91

LIST OF FIGURES xiv

FIGURE 4.10	–Picture of a Stripmap acquisition of the city of Piúma, in Brazil, obtained by TerraSAR-X. Many bright spots can be seen outside of landmass, due to the ambiguous signals coming from the city, which overlap with the received signal of the ocean. This is an example of the necessity of minimizing ambiguity power as much as possible in SAR acquisitions. This image was extracted from (Ribeiro, 2021)	92
FIGURE 4.11	-Map of all the points which are capable of imaging an EST image at $\theta_i = 27^{\circ}$, with a swath width of 5 km (blue). Note how the majority of pairs which are able to concurrently acquired two ST images lie in the $\eta_1 = 0.5$ axis	93
FIGURE 4.12	–Simulation for the RASR of an Extended Staring Spotlight image, which is 2.5 km in azimuth and 5.0 km in elevation (only half of the scene is present). This was collected for an incidence angle of $\theta_i = 27^{\circ}$, $\eta_1 = 0.5$, and PRF = 5000 Hz. In the particular case of this simulation, a grid of 400x400 pixels was built, and each one is associated with a specific value of RASR. All values of ambiguous power are in dB	96
FIGURE 4.13	-PRF map of Fig. 4.11, with each pair of parameters associated with the worst extractable RASR value of the EST image (first half of the extended scene). The EST acquisition is done at 27 degrees of incidence angle and has a swath width of 5 km	97
FIGURE 4.14	Distribution of ambiguous power (AASR) coming from azimuth ambiguities throughout the first half of the extended scene. The AASR is shown in dB, and it is approximately symmetrical at $\mathbf{x}=0$, since range differences in distance do not alter the influence of azimuth ambiguities. The worst values of azimuth ambiguities will always be symmetrically at the boarders. For this particular simulation, the worst AASR value of the whole grid is -24 dB	98
FIGURE 4.15	AASR map built from associating every pair of Fig. 4.11 with the worst AASR value extracted from the respective image grid. For any kind of Staring Spotlight acquisition, as PRF increases the AASR quality of the image tends to increase. Note how the AASR value does not change with a variation of η_1	99
	4000 1100 offiniso with a variation of 1/1	

LIST OF FIGURES xv

FIGURE 4.16 -	-ASR map, obtained by summing all ambiguities which overlap with	
	the intended scene (RASR and AASR maps are combined). Notice	
	how almost all points on the map yield far too high of an ambiguity	
	power to be considered suitable to an acquisition, since the majority	
	of them are in the red-orange color scheme. Still, there is a wide col-	
	lection of points with reasonable quality (yellow-green range) which	
	can be utilized to acquire an EST product as specified	100
FIGURE 4.17	-Collection of pairs whose ambiguity power is lower than -17 dB,	
	therefore being considered suitable for an EST acquisition of 5 km $$	
	swath width, 5 km extended azimuth length, at $\theta_i = 27^{\circ}$	102
FIGURE 5.1 –	Best extractable ASR (in blue) utilizing the Extended Staring Spot-	
	light method to acquire an extended scene of 5 km swath width	
	by 5 km composite azimuth length, for all incidence angles within	
	TerraSAR-X's full-performance span. The data is presented along	
	with a tendency curve (in orange), which depicts the upward trend	
	of the ambiguity power. The minimum threshold of -15.5 dB (in red)	
	is satisfied by all incidence angles below 40°, proving the feasibility	
	of the EST method for a variety of scenarios	109

List of Tables

TABLE 5.1 –	Table results of simulations for an EST acquisition, with 5 km of swath width and 5 km in total azimuth length. Until 35°, the ambiguity quality is below the minimum quality threshold of -17 dB. Precision: $(\Delta \eta_1, \Delta PRF, \Delta ASR = \pm 0.01, \pm 10 \text{ Hz}, \pm 0.2 \text{ dB}). \ldots 1$.05
TABLE 5.2 –	Table results of simulations for an EST acquisition, with 5 km swath width and 5 km total azimuth length. After 35°, the ambiguity power struggles to hit the quality threshold of -17 dB, and after 40° not even the minimum tolerable limit of -15.5 dB. Precision: $(\Delta \eta_1, \Delta PRF, \Delta ASR = \pm 0.01, \pm 10 \text{ Hz}, \pm 0.2 \text{ dB})$.06
TABLE 5.3 –	Table results of simulations for an EST acquisition, with 5 km of swath width and 5 km in total azimuth length. This table displays the necessary η_1 to achieve maximum image quality at the first half of the extended scene, but not for the entire picture. Until 35°, the ambiguity quality is below the minimum quality threshold of -17 dB. Precision: $(\Delta \eta_1, \Delta PRF, \Delta ASR = \pm 0.01, \pm 10 \text{ Hz}, \pm 0.2 \text{ dB}). \ldots 1$.07
TABLE 5.4 –	Table results of simulations for an EST acquisition, with 5 km of swath width and 5 km in total azimuth length. This table displays the necessary η_1 to achieve maximum image quality at the first half of the extended scene, but not for the entire picture. After 35°, the majority of sampled incidence angles does not fit the quality threshold of -17 dB. After 40°, the minimum threshold of -15.5 dB is not met as well, aside from some specific directions. Precision:	
	$(\Delta \eta_1, \Delta PRF, \Delta ASR = \pm 0.01, \pm 10 \text{ Hz}, \pm 0.2 \text{ dB}). \dots \dots$.08

Contents

1	Int	ROI	DUCTION	20
2	An	TEN	NA AND RADAR FUNDAMENTALS	25
	2.1	Elec	etromagnetism	26
	2.2	Ant	ennas	29
	2.3	Ant	enna Array	34
	2.3	.1	Composite Field of Array	34
	2.4	Gra	ting Lobes	38
	2.5	Intr	oduction to Radars	40
	2.5	.1	Transmission (Tx) and Reception (Rx)	40
	2.5	.2	SNR	41
	2.5	.3	Point-Target Localization	43
	2.6	Wav	ve Interaction with Materials	44
	2.6	.1	Amplitude	45
	2.6	.2	Phase Shifts	45
	2.7	Res	olution and Coverage	47
	2.7	.1	Resolution	47
	2.7	.2	Coverage	49
	2.8	Sun	nmary	50
3	Syn	NTH:	ETIC APERTURE RADAR	51
	3.1	Side	e-Looking Airborne Radar (SLAR)	51
	3.2	Syn	thetic Aperture Radar (SAR)	57
	3.3	Am	biguities	62

	3.3.1	Range Ambiguities	63
	3.3.2	Range Ambiguity-to-Signal Ratio (RASR)	65
	3.3.3	Azimuth Ambiguities	66
	3.3.4	Azimuth Ambiguity-to-Signal Ratio (AASR)	69
	3.4 Acc	quisition Modes	69
	3.4.1	Stripmap (SM)	69
	3.4.2	Spotlight	71
4	Exten	DED STARING SPOTLIGHT	76
	4.1 Dis	continuity in Traditional ST	76
	4.2 Con	ncurrent Imaging	78
	4.2.1	Core Concepts	78
	4.2.2	Limitations on Concurrent Imaging	81
	4.3 Ext	ending the Staring Spotlight	82
	4.3.1	The Extension Method	83
	4.3.2	Technical Analysis	84
	4.4 Me	thodology	86
	4.5 Tin	ning Analysis	86
	4.5.1	Conventional Timing Analysis	87
	4.5.2	Concurrent Timing Analysis	89
	4.5.3	Asymmetrical Concurrent Imaging	91
	4.5.4	PRF Maps	93
	4.6 Am	biguity Power	94
	4.6.1	Range Ambiguities Assessment	95
	4.6.2	Azimuth Ambiguities Assessment	97
	4.6.3	Ambiguity Signal Ratio	99
	4.6.4	Threshold filtering	101
	4.7 Imp	plementation	103
5	GENER	BAL RESULTS	104

CONTENTS										xix								
6	Conclusion													•				110

1 Introduction

The current state-of-the-art technology for digital imagery of the surface of the Earth is subdivided in many different fields, each leveraging its technical properties and algorithmic implementations to better pursue a minimum of detail and image quality as a product, whilst not sacrificing the size of the acquired area. Conventional airborne radar hardware has embedded within it a fixed size antenna which emits electromagnetic pulses towards a particular region of interest on Earth's curvature, capturing the received signals with the same antenna. While simpler in implementation when comparing to other methods and cheaper in terms of data storage and data down-link, the resolution of the image acquired via this method demands a large-sized antenna (dozens of meters) for a decent level of details - but still requires some polishing of the received signals in terms of frequency distortions.

A particular niche in telecommunications - specially radar technology - which is currently experiencing a golden age is a particular set of radars - the Synthetic Aperture Radars, or SAR. This type of radar is able to exploit the movement of the antenna equipment with clever algorithmic techniques to emulate a broader antenna, providing a much finer resolution in the direction of movement (azimuth), regardless of the distance of the mobile unit from the target area. The usage of algorithms such as the Range-Doppler algorithm to correct distorted frequencies also brings significant power to SAR systems, enabling acute measurements regardless of weather conditions or day and night time.

When it comes to the usage of SAR for ground image acquisition, we may scan an area exploiting different techniques, particularly by maneuvering the direction of the antenna beam as the platform (airplane or satellite) passes by. Depending on how this maneuvering is executed (alongside other more refined techniques of acquisitions), the image obtained will have a determined size and resolution. Typically, techniques which extract larger image areas do so while degrading its level of detail. Likewise, methods whose focus is obtaining better resolution values deliver images with high levels of quality, but at the cost of small acquisitions. This is one of the most relevant trade-offs a client needs to account for when requesting to scan an image of the ground - an improvement in resolution will come at the cost of a smaller image size, and vice-versa.

In the current state-of-the-art acquisitions done by satellites, the two most common modes for ground scanning are **Stripmap** (**SM**) and **Spotlight**. The former is capable of acquiring a large portion of the scenery at the cost of azimuth resolution, while the latter ensures one of the highest possible values of definition (aside from the Circular SAR technique¹) but limits the size of the ground image to a narrow length in the direction of movement. Fig. 1.1 displays the general trend of the resolution trade-off for both modes.

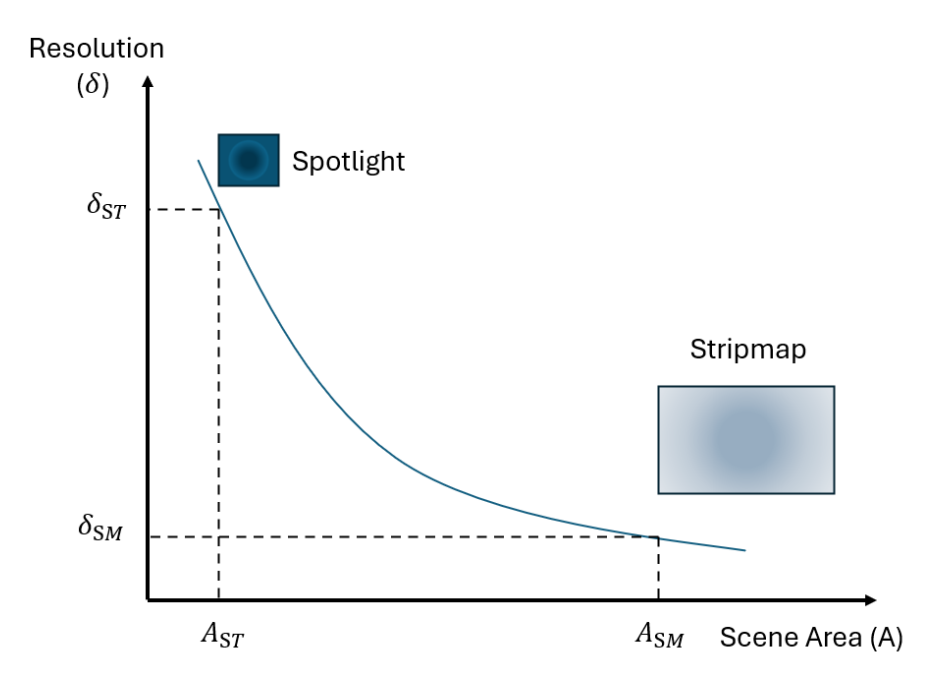


FIGURE 1.1 – General trend for the trade-off between resolution and scene area. The Spotlight mode extracts higher resolution of the image at the cost of scene size, while Stripmap provides broader coverage and worse image resolution. The resolution used is not technical, just a conceptual notion for quality and image definition.

The Stripmap mode of acquisition is done such that while the platform moves, the antenna maintains a fixed angle (usually zero) with the normal axis, while the Spotlight mode keeps the antenna focused to a point on the ground (Staring Spotlight or ST) or beneath it (Sliding Spotlight or SL). Fig. 1.2 depicts both SM and ST process being executed. During the whole acquisition, the mode chosen to operate will lock the specifications of the image obtained, forcing the designer to choose whether it is more desirable to sacrifice area over resolution or the other way around.

In the mid-2010s, however, a new and innovative SAR-focused technique called **Concurrent Imaging** was proposed, and with it the possibility of imaging *multiple* areas on the ground, roughly at the same time. Areas far apart could be scanned with the same device, without needing a second trip of the satellite. Additionally, each of the images

¹Circular SAR is a method of acquisition where a platform embedded with a SAR system moves in a circular path above the ground, pointing its antenna towards the projection of the center onto the ground. It is considered to provide the best azimuth resolution of all known SAR techniques.

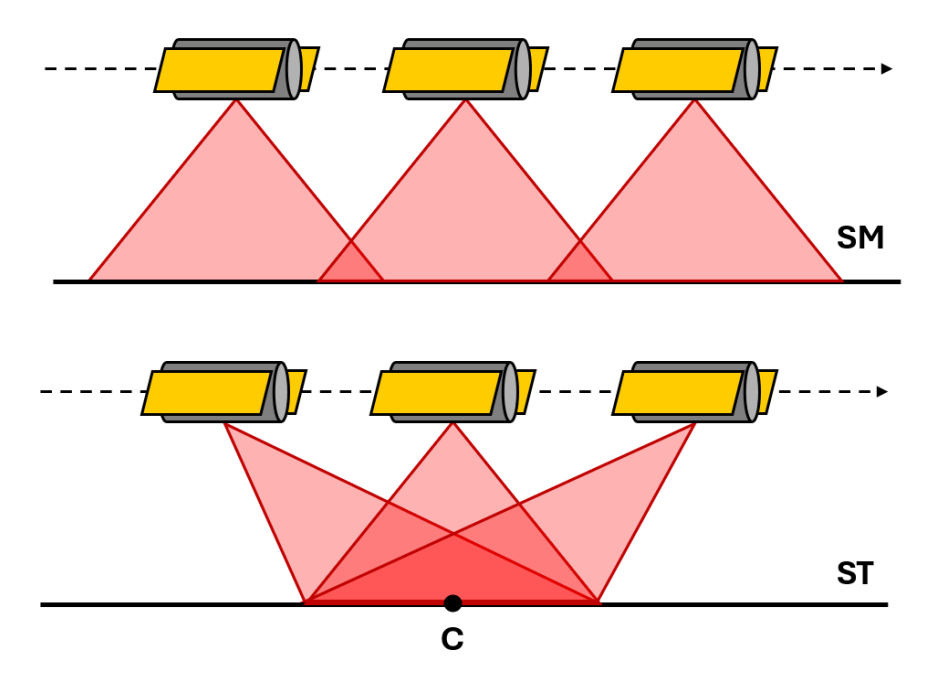


FIGURE 1.2 – Depiction of both Stripmap (SM) and Staring Spotlight (ST) modes in action. The first mode (SM) has the antenna fixed at a particular angle (usually zero) at all times, leading to a broader image size but less time of illumination of any particular point on the ground. The second mode (ST) has the antenna being steered in such a way that the beam center always points towards a rotation center (C), which in the case of ST is on the center of the scene we wish to acquire. This reduces the *azimuth* length of the image acquired, but all points are illuminated during the entire movement of the platform, which itself boosts resolution. If C was geometrically below the ground, however, it would be a *Sliding Spotlight* (SL), being an intermediate case between SM and ST in both scene size and resolution.

could be acquired with its specific mode, allowing for example the acquisition of one scene with the use of Stripmap and another one with the use of the Spotlight mode.

The Concurrent Imaging technique has a broad and yet untapped potential of applications. It has been utilized to scan areas with the so called *heterogeneous complexity* leveraging both Stripmap and Spotlight modes, and for obtaining concurrently two areas far apart from each other, close to the Equator.

However, one application that has not been thoroughly investigated is the usage of Concurrent Imaging in the case of two concurrently acquired scenes, where one is juxtaposed to the next, in the direction of movement of the platform. If done so, and proven to be viable, this would allow a given satellite to extract the maximum possible area of a given acquisition mode whilst conserving the exact same *azimuth* resolution of a conventional acquisition.

In this work, we seek to investigate the viability of a particular use case. By leveraging Concurrent Imaging as a support technique, we wish to *extend* the Staring Spotlight mode, acquiring two different scenes at the same time. These two scenes will be aligned and equally far apart from the satellite, while being juxtaposed in the *azimuth* direction. With each scene acquired by an ST mode, we can combine both and produce an *Extended Staring Spotlight* (EST), where the area of the extracted image could be **doubled** (potentially

quadrupled) with no degradation to resolution whatsoever. Fig. 1.3 shows the general idea of the proposed mode in action.

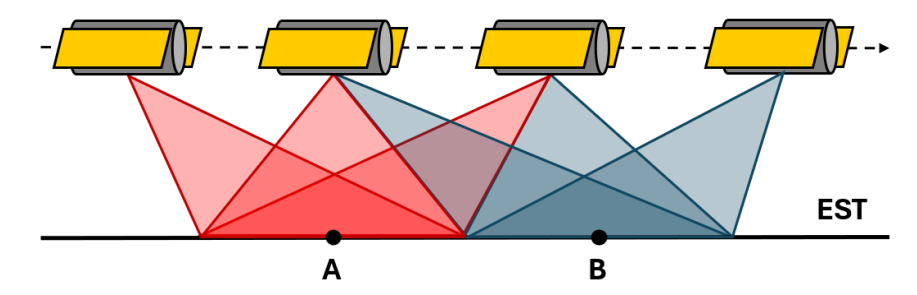


FIGURE 1.3 – Depiction of the Extended Staring Spotlight mode (EST) proposed in this thesis. By leveraging Concurrent Imaging, one can synthesize two acquisitions, each done respectively in ST and towards their respective scene centers. By doing so, we double the length of the image in the azimuth direction, whilst keeping the resolution of ST acquisitions throughout the whole picture.

The core goal of the research presented in this Bachelor Thesis is to propose the *Extended Staring Spotlight*, suggesting a general method for employing it, analyzing the quality results in simulations and the viability of this technique in a production scenario.

In terms of structure, this thesis is subdivided into five main sections:

- In Chapter 1, a brief overview of the main concept of the Extended Staring Spotlight, and its context within telecommunications and SAR imaging techniques.
- In Chapter 2, the necessary context will be given to antenna technology and the main concepts of radar imaging, as both fields must be precisely defined, and its nuances pointed out, to better understand the objectives and limitations of the EST technique.
- In Chapter 3, conventional radar systems such as RAR and SLAR will be defined, but more importantly, Synthetic Aperture Radar (SAR) will be explained, as well as its main constraints Range Ambiguities and Azimuth Ambiguities. The primary methods of image acquisition Stripmap and Spotlight will be depicted, and its parameters demonstrated.
- In Chapter 4, the core of the thesis will be unraveled. We define the current problem with conventional techniques of image acquisition, in particular the problem with Staring Spotlight imaging. We demonstrate its incapability to scale without degrading resolution, leading the way for the introduction of Concurrent Imaging, which will be thoroughly explained. A method which leverages it will be proposed to extend the length of conventional Staring Spotlight images, which then will become the Extended Staring Spotlight technique. Finally, an investigation methodology a workflow - will be detailed to analyze whether an EST acquisition, for a particular incidence angle θ_i , is feasible, both from timing and quality perspectives.

• In the final chapter - Chapter 5 - we compile the computational results of simulations for many incidence angles - from 20° to 45 - and the overall quality performance of the EST acquisition method. We prove that it can double image area while maintaining reasonable quality levels (-17 dB or 2% of spurious power) for the majority of the incidence angle spectrum, hence the Extended Staring Spotlight can be used as a reliable method for acquiring larger areas while maintaining high-grade resolution. The parameters necessary to achieve these quality levels are also put in table, as reference for future clients and designers to implement.

This work was done via collaboration between the Aeronautics Institute of Technology (ITA) and the German Aerospace Center (DLR - Deutsches Zentrum für Luft-und Raumfahrt), utilizing their systems and resources for the completion of the project. It also must be noted that many of the quality criteria and test benchmark standards will be compared to much of their hardware, particularly the TerraSAR-X scanning satellite, launched in 2007.

All the data compiled in Chapter 5 of this thesis was simulated, as TerraSAR-X's native finite state-machine cannot handle the usage of Concurrent Imaging of two different Spotlight modes - only Stripmap/Stripmap, Stripmap/Spotlight. Still, all data presented in this thesis was part of a **peer-reviewed paper**, **published at the IEEE RadarConf 2025** in Krakow, Poland (L. F. S. R. Soares J. P. T. Ribeiro; Bachmann, 2025).

${f 2}$ Antenna and Radar Fundamentals

The use and manipulation of electromagnetic waves for interpreting reality is, in both concept and application, exceedingly ancient yet recurrently modern. A portion of this wave spectrum, which we perceive as light, propagates from the corners of the world and the universe to our eyes—traversing even time itself through the distant past, which becomes visibly present through the observation of stars. While for millennia we observed them with the naked eye, only a few centuries ago we bent their light through refraction, constructing telescopes. Technological progress has made it possible to manipulate and investigate the electromagnetic spectrum for a deeper understanding of our surroundings—whether such *connaissance* arises from military ambitions, scientific curiosity, or even as a pastime.

At the end of the 19th century, the completion of Classical Electromagnetic Theory as a set of mathematical explanations for the behavior of electric and magnetic fields, as well as their mutually coupled interactions, was finalized by Maxwell. From this, the physicist derived the synthesis of field propagation—electromagnetic waves, of which light was postulated to be composed. The equations now modernly known as Maxwell's Equations (2.1) led to the ultimate conclusion that light must be a wave and must possess a defined velocity given by $c_0 = \frac{1}{\sqrt{\mu_0 c_0}}$, or 299,792,458 m/s in a vacuum.

A little over a decade later, Heinrich R. Hertz confirmed the existence of electromagnetic waves, as theorized.

Through the study of the properties of these waves, various techniques were proposed for detecting and characterizing the world and the universe—arguably the most important of which was developed in the 20th century with the invention of radar.

Radar devices are used to detect targets in their vicinity. They are capable of emitting electromagnetic waves—with well-determined frequency and intensity distribution—either toward specific regions of interest or isotropically in all directions. A portion of this energy strikes a target or object of interest and is reflected back to the emitter, allowing us to compute the target's distance from the radar by measuring the time required for the pulse to complete its journey.

This principle, rudimentary as it may be, marked the dawn of a range of new tech-

nologies inspired by the return of emitted energy to obtain information about an imaged target—or terrain.

The refinement of radar technology would soon allow not only the extraction of a point target's instantaneous position but also the complete description of terrains, forests, and landscapes on Earth's surface through the installation of radars on aircraft.

By the late 1950s, the concept of *Synthetic Aperture Radar* was developed, ushering in a new era of remote sensing in which various imaging techniques and methods would be proposed—each with its advantages and also its limitations concerning image quality (noise), level of detail (resolution), and the acquired area.

This bachelor thesis aims to present a new imaging alternative in which high image resolution is maintained while allowing the acquisition area to reach up to four times what is expected with the traditional method.

The following sections of this chapter aim to briefly but solidly present the technological foundations necessary for understanding the central theme of this work.

2.1 Electromagnetism

As briefly presented in the introductory section, by the end of the 19th century, classical electromagnetism had been reasonably well established, and the synthesis of the entire theoretical framework produced culminated in the formulation of Maxwell's Equations (2.1).

$$\begin{cases} \nabla \cdot \vec{D} = \rho \\ \nabla \cdot \vec{B} = 0 \\ \nabla \times \vec{E} = -\frac{\partial \vec{B}}{\partial t} \\ \nabla \times \vec{H} = \vec{J} + \frac{\partial \vec{D}}{\partial t} \end{cases}$$
(2.1)

The vectors \vec{D} and \vec{B} encompass the fluxes of the electric field vector \vec{E} and the magnetic field vector \vec{H} (also referred to as the electric displacement field and the magnetic induction field), and the vector \vec{J} represents the surface density of electric current.

The presented relations mathematically describe the behavior of any field distribution in the universe and express that such fields can only be generated:

- By a region with a non-neutral electric charge density (electric monopole Gauss's Law for Electrostatics);
- By a temporal variation in magnetic flux (Faraday's Law);

• By the existence of a nonzero surface current density (Ampère's Law) and/or by a temporal variation in electric flux, called displacement current, an adjustment made by Maxwell.

Additionally, they also establish ad hoc that the so-called magnetic monopole cannot exist (Gauss's Law for Magnetism).

Maxwell sought to understand the behavior of fields independent of external sources (arbitrarily given), solving the set of equations for the case where $\vec{J}=0$ and $\rho=0$, meaning a region without electric charges or current sources, such as a vacuum. Furthermore, the vacuum can be considered a *simple medium*, allowing us to treat the electric and magnetic fluxes as isotropic. In other words:

$$\vec{D} = \epsilon_0 \vec{E} \Longrightarrow \nabla \cdot \vec{E} = \frac{\rho}{\epsilon_0} ,$$

$$\vec{B} = \mu_0 \vec{H} \Longrightarrow \nabla \cdot \vec{H} = 0 \ .$$

Applying these conditions to (2.1), we can also apply the curl operator $(\nabla \times)$ to equations (2.1.3) and (2.1.4).

Recalling the property $\nabla \times (\nabla \times M) = \nabla(\nabla \cdot M) - \nabla^2 M$, we develop the equations for the cited case where $\rho = 0$ and $\vec{J} = \vec{0}$:

$$\nabla \times (\nabla \times \vec{E}) = \nabla (\nabla \cdot \vec{E}) - \nabla^2 \vec{E} ,$$

$$\frac{\partial}{\partial t}(\nabla \times \vec{B}) = \nabla^2 \vec{E} \ ,$$

$$\frac{\partial}{\partial t}(\mu_0 \vec{\hat{J}} + \mu_0 \epsilon_0 \frac{\partial \vec{E}}{\partial t}) = \nabla^2 \vec{E} \ .$$

Since $\mu_0 \epsilon_0$ has the dimension of the inverse of the square of velocity, defining $c_0 = \frac{1}{\sqrt{\mu_0 \epsilon_0}}$:

$$\boxed{ \therefore \frac{1}{c_0^2} \frac{\partial^2 \vec{E}}{\partial t^2} - \nabla^2 \vec{E} = 0 } \; ,$$

$$\boxed{ \therefore \frac{1}{c_0^2} \frac{\partial^2 \vec{H}}{\partial t^2} - \nabla^2 \vec{H} = 0} \ .$$

The derivation of the magnetic field equation is analogous.

The deduced formulations reveal two second-order partial differential equations, analogous to the equations of wave disturbances in material media, leading Maxwell to conclude that the propagation of light must exhibit **wave-like behavior**. The solutions are given by the vectors:

$$\begin{cases}
\vec{E} = \vec{E_0} \cdot e^{j(\vec{k_0} \cdot \vec{r} - \omega t + \phi_0)} \\
\vec{H} = \vec{H_0} \cdot e^{j(\vec{k_0} \cdot \vec{r} - \omega t + \phi_0)}
\end{cases}$$
(2.2)

In which $\vec{k_0} = \frac{2\pi}{\lambda}\hat{r}$ is the wave vector, a quantity responsible for measuring the phase change of the field based on the measured position; $\omega = 2\pi f_0$ is the angular frequency; and ϕ_0 is the initial phase, for $(t, \vec{r}) = (0, \vec{0})$.

The vectors in (2.2) are the complex analogs of the fields, which are obtained by extracting the respective real parts. For the so-called TEM waves (Transverse Electromagnetic), the electric and magnetic fields are orthogonal to each other, but they are in phase temporally.

Fig. 2.1 graphically represents the behavior of the electromagnetic field in a vacuum, for a linearly polarized wave $(\vec{E_0} = E_0 \hat{y})$.

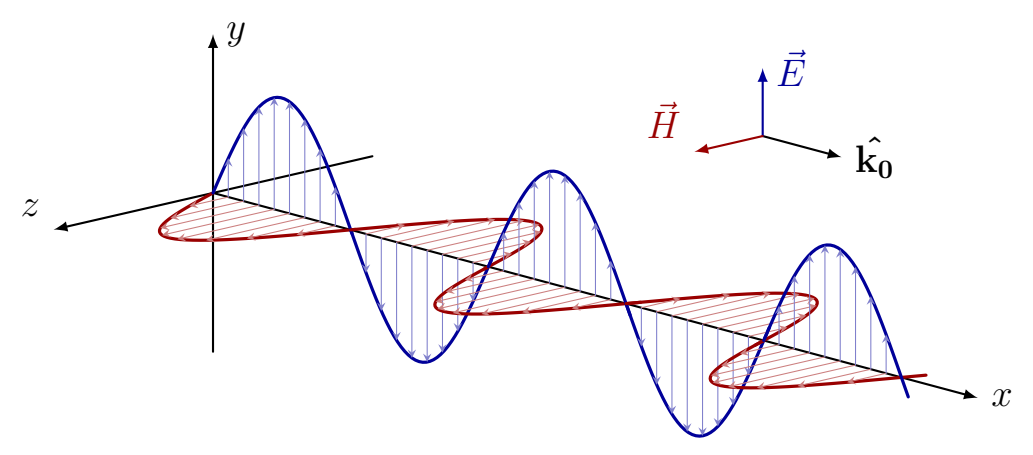


FIGURE 2.1 – An electromagnetic wave being propagated in the vacuumm. There are no charge or current sources, and no electric or magnetic walls are nearby. Under these constraints, the wave behaves as an TEM wave, with vectors \vec{E} and \vec{H} preserving orthogonality between them, and defining a plane that is perpendicular to the direction of propagation.

A fundamental property of any electromagnetic wave is its ability to transmit power intensity, a quantity determined by the Poynting vector, defined as $\vec{S} = \vec{E} \times \vec{H}^*$. Since this product has the dimensions of energy intensity (W/m², in SI), the Poynting vector is understood as the instantaneous power transfer to an infinitesimal local area, in the direction of the wave's propagation. Furthermore, the average radiation intensity can be given as $\langle \vec{S} \rangle$. We will limit the introductory study of power transmission by waves to the vector \vec{S} , without needing deeper analysis.

As will be discussed later, it is through the transmission and reception of power from electromagnetic waves that radars are capable of detecting targets. But more than that – through the tabulation of the dielectric properties of multiple materials, it is possible to even understand the nature of the target and its composition, allowing future use of waves for soil and subsurface imaging.

2.2 Antennas

The behavior of electromagnetic waves in a vacuum or in an isotropic medium is only part of the study of electromagnetism associated with radars – the process of **production** and **emission** of these waves is critical.

Antennas are devices capable of transforming electric currents into electromagnetic waves, emitting them from their structure into the free space, and conversely, they are also capable of transforming received waves into electric currents.

The wave generation process arises from the application of Maxwell's Equations (2.1) to a metallic object crossed by a non-zero surface current density, for the transmitting antenna, and in a region crossed by a magnetic source (variation of the magnetic flux in a closed loop).

Although we can characterize the electromagnetic wave in a vacuum (or in simple isotropic media without losses or sources), the determination of antenna parameters involves electric and magnetic sources – therefore, we are forced to reevaluate Maxwell's Equations under new constraints.

By performing the same procedure that resulted in equations 2.2.1 and 2.2.2, but this time considering ρ and \vec{J} as non-zero, in addition to an isotropic, lossless medium, we obtain the field equations without null sources of current and electric charge – we are disregarding the possibility of magnetic sources and taking all fields and current sources as sinusoidal. Therefore, $\frac{\partial}{\partial t}A = j\omega A$.

$$\nabla^2 \vec{E} + k_0^2 \vec{E} = \frac{\nabla \rho}{\epsilon_0} + j\omega \mu_0 \vec{J} , \qquad (2.3)$$

$$\nabla^2 \vec{H} + k_0^2 \vec{H} = -\nabla \times \vec{J} \ . \tag{2.4}$$

In which we again fall into two second-order partial differential equations, but this time *inhomogeneous*, since the independent terms of both equations are non-zero.

$$\nabla^2 \vec{E} + k_0^2 \vec{E} = \frac{\nabla \rho}{\epsilon_0} + j\omega \mu_0 \vec{J} , \qquad (2.5)$$

$$\nabla^2 \vec{H} + k_0^2 \vec{H} = -\nabla \times \vec{J} \ . \tag{2.6}$$

Thanks to Gauss's Law of Magnetism, in which the *divergence* of the magnetic flux density field \vec{B} is zero, we can assign it a **vector potential** \vec{U} , such that $\vec{B} = \nabla \times \vec{U}$, because $\nabla \cdot \vec{B} = \nabla \cdot (\nabla \times \vec{U}) = 0$, thus respecting the condition imposed for every vector potential.

Applying this condition to Faraday's Law and Ampère's Law, we obtain:

$$\nabla \times \vec{E} = -j\omega \vec{B} = -j\omega (\nabla \times \vec{U}) \Longrightarrow \nabla \times (\vec{E} + j\omega \vec{U}) = \vec{0}$$

Since $\nabla \times (-\nabla \Omega_0) = \vec{0}$, where Ω_0 is any scalar function that we will call the **scalar potential function**, we can say, by the linearity of the rotational operator $(\nabla \times)$, that $\vec{E} = -j\omega \vec{U} - \nabla \Omega_0$.

In a similar manner, developing Ampère's Law:

$$\nabla \times \vec{B} = \mu_0 \vec{J} + j\omega \mu_0 \epsilon_0 \vec{E} \Longrightarrow \nabla \times (\nabla \times \vec{U}) = \mu_0 \vec{J} + j\omega \mu_0 \epsilon_0 \vec{E}$$

$$\therefore \nabla(\nabla \cdot \vec{U}) - \nabla^2 \vec{U} = \omega^2 \mu_0 \epsilon_0 \vec{U} - j\omega \mu_0 \epsilon_0 \nabla \Omega_0 + \mu_0 \vec{J}$$

$$\iff \nabla^2 \vec{U} = \omega^2 \mu_0 \epsilon_0 \vec{U} - \nabla(j\omega \mu_0 \epsilon_0 \Omega_0 + \nabla \cdot \vec{U}) + \mu_0 \vec{J}$$

By the Lorentz Condition, in which $j\omega\mu_0\epsilon_0\Omega_0 + \nabla \cdot \vec{U} = 0$, we obtain the equation for the vector potential, and its solution 2.7, where $\vec{r'}$ is the distance vector from the current source to the origin of the coordinates, \vec{r} is the position vector of the analysis point, and $k_0 = \omega^2 \mu_0 \epsilon_0$. The following relations display how to extract the electric and magnetic fields from the vector potential.

$$\left| \vec{U} = \frac{\mu_0}{4\pi} \int_v \frac{\vec{J}(\vec{r'})e^{(-jk_0(\vec{r}-\vec{r'}))}}{\vec{r}-\vec{r'}} dv \right|, \tag{2.7}$$

$$\therefore \vec{H} = \frac{\nabla \times \vec{U}}{\mu_0} \Longrightarrow \vec{E} = j\omega \vec{U} + \frac{\nabla(\nabla \cdot \vec{U})}{j\omega\mu_0\epsilon_0}$$
 (2.8)

The previous development allows us to characterize the field distribution generated by a current source at any point in the surrounding space. In Antenna Theory, it is customary to distinguish the space surrounding the antenna into three regions:

- Reactive Zone The region immediately adjacent to the antenna structure $(|\vec{R}| < 0.62 \cdot \sqrt{L^3/\lambda})$. In this region, the electric and magnetic fields are resonant and do not transmit power.
- Fresnel Zone The intermediate region $(0.62 \cdot \sqrt{L^3/\lambda} < |\vec{R}| < 2L^2/\lambda)$ where the fields emit power but the waves cannot be treated as TEM.
- Fraunhofer Zone The far zone region $(|\vec{R}| > 2L^2/\lambda)$, where waves can be treated as TEM, planar, and power-transmitting.

In this work, the antennas used for image acquisition will be hundreds of kilometers from the ground. For the satellite TerraSAR-X, which will be frequently used as a reference during the thesis, the equipment is located precisely 519 kilometers above sea level. The frequency band used is the so-called X-Band, with a frequency of approximately 10 GHz and, therefore, a wavelength of 3 cm. Since the longest dimension of the antenna is 4.8m, the $Fraunhofer\ Zone$ condition is approximately 1.67 km. Therefore, all the analysis conducted in this document will entirely consider distant fields.

For a simple radiator (dipole), with a length Δl , carrying a current I_0 , and thus a surface current density $\vec{J} \cdot d\vec{s}$, the vector potential \vec{U} is obtained by using equation 2.7.

$$\vec{U} = \frac{\mu_0}{4\pi} \int_v \frac{\vec{J}(\vec{r'})e^{-jk_0r}}{r} (dz \cdot ds) \Longrightarrow \boxed{\vec{U} \approx \frac{\mu_0}{4\pi} \frac{I_0 \Delta l e^{-jk_0r}}{r} \hat{z}}$$
(2.9)

The vector potential \vec{U} in 2.9 was obtained for the far field and can be decomposed into a system of spherical coordinates $(\hat{\rho}, \hat{\theta}, \hat{\phi})$. Only the components in ρ and θ are of interest to us, and the decomposition is straightforward, resulting in

$$\begin{cases}
\vec{U}_{\theta} = -\frac{\mu_0}{4\pi} \frac{I_0 \Delta l e^{-jk_0 r}}{r} sin(\theta) \hat{\theta} , \\
\vec{U}_{\rho} = \frac{\mu_0}{4\pi} \frac{I_0 \Delta l e^{-jk_0 r}}{r} cos(\theta) \hat{\rho} .
\end{cases}$$
(2.10)

Applying the relations from 2.8 in 2.10, the electromagnetic field of the dipole is completely defined by

$$\vec{E} \approx j \frac{I_0 \Delta l}{4\pi} sin\theta \frac{sin(\frac{k_0 \Delta l cos\theta}{2})}{\frac{k_0 \Delta l cos\theta}{2}} \frac{\omega \mu_0}{r} e^{-jk_0 r} \hat{\theta}, \qquad (2.11)$$

$$\vec{H} \approx j \frac{I_0 \Delta l}{4\pi} sin\theta \frac{sin(\frac{k_0 \Delta l cos\theta}{2})}{\frac{k_0 \Delta l cos\theta}{2}} \frac{\omega \mu_0}{r \eta_0} e^{-jk_0 r} \hat{\phi} . \tag{2.12}$$

Equations 2.11 and 2.12 were obtained in the **Fraunhofer Zone**, so that **there is no reactive field** derived from the current in the antenna, in this region – that is, part of the field does not accumulate energy, since the *Poynting Vector* $\vec{S} = \vec{E} \times \vec{H}^*$ is purely radial $(\vec{S} = S \cdot \hat{\rho})$, thus radiating – unlike the field in the *Fresnel Zone*, for example, where part of the field is in the $\hat{\theta}$ component, meaning a rotational field around the \hat{z} axis.

The average power radiated by the device is given by the **Average Poynting Vector** $(\langle \vec{S} \rangle)$, whose value is given by:

$$<\vec{S}> = \int_{t=0}^{T} \frac{1}{T} \vec{S}(t) dt \Longrightarrow <\vec{S}> = \frac{1}{2} \operatorname{Re} \left\{ \vec{E} \times \vec{H}^* \right\},$$

$$\therefore <\vec{S}> \propto \frac{\sin^2(\frac{k_0 \Delta l \cos \theta}{2})}{(\frac{k_0 \Delta l \cos \theta}{2})^2}.$$

This proportionality shows us that the intensity of electromagnetic waves depends on the transmission direction.

That is, the power transmission is not necessarily isotropic. From this fact, we derive the concepts of **irradiation intensity**, **directivity**, and **gain**.

The **irradiation intensity** $U(\theta, \phi)$ is the amount of power radiated per solid angle (in S.I., W/Ω). In other words, by the relations in 2.13.

$$U(\theta, \phi) = \frac{P_0}{4\pi} = \langle \vec{S} \rangle r^2$$
 (2.13)

The **directivity** $D(\theta, \phi)$, in turn, is the ratio between the irradiation intensity in a specific direction and the average irradiation intensity – it can be interpreted as the general measure of the main direction in which the antenna radiates power. Mathematically, it is defined by

$$D(\theta,\phi) = \frac{U(\theta,\phi)}{U_0} = \frac{U(\theta,\phi)}{\int_{\Omega-0}^{\pi} \int_{\omega-0}^{2\pi} U(\Omega,\omega) d\omega d\Omega} . \tag{2.14}$$

Finally, the concept that will be most used ahead is that of **Gain**, which is simply treated in this work, by the relation 2.15, as proportional to the directivity, by an efficiency factor k. It is customary to consider that there are no losses, both in free space and in the architecture of the devices, so the distinction between directivity and gain will be irrelevant. That is, **Gain** is an antenna parameter that indicates the direction in which the device radiates the most power, taking into account loss factors.

$$G(\theta, \phi) = k \cdot D(\theta, \phi) . \tag{2.15}$$

The consecutive use of the relations 2.13, 2.14, and 2.15 shows us that the quantity *Gain* is also direction-dependent (as expected), in a spherical coordinate system positioned at the emission source, that is:

$$G(\theta,\phi) \propto \frac{sin^2(\frac{k_0\Delta lcos\theta}{2})}{(\frac{k_0\Delta lcos\theta}{2})^2}$$
.

Where θ is the angle measured from the axis of the elementary linear radiator, and we can define $\gamma = \frac{\pi}{2} - \theta$ as the antenna angle, measured from the axis perpendicular to the length axis of the radiator.

The direction of most power emitted from an irradiator is called **boresight**.

All the discussion so far indicates that, depending on the current distribution of the device, its geometry, and its proximity to the target, the irradiation intensity of the antenna is anisotropic, giving preference (i.e., assigning higher gain) to the direction perpendicular to its length.

Fig. 2.2 shows the gain distribution for an antenna element, for $-\frac{\pi}{2} \leq \gamma \leq \frac{\pi}{2}$. Note that there are preferred directions of power radiation (*lobes*), so the design must include the target in the so-called **main lobe**, which has the highest gain.

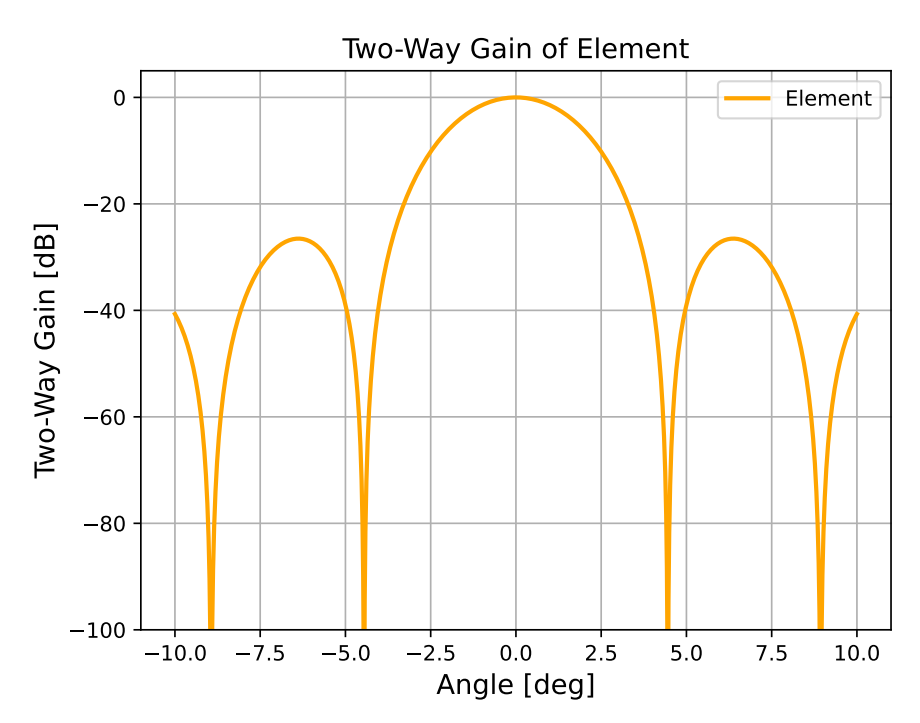


FIGURE 2.2 – Irradiation diagram of an antenna element (Two-Way - the wave travels forth and back to the equipment). The intensity is measured for every angle with respect to the boresight direction - the maximum intensity direction. The intensity pattern follows the trend of lobes - the Main Lobe, the first Side Lobes, the second Side Lobes, and so on.

A commonly used design metric is the *Half Power Beam Width*, i.e., the value of the angular width for a main lobe, between two points that are at half the power of the peak. Its value is approximately given as:

HPBW
$$\approx 0.886 \cdot \frac{\lambda}{L}$$

Where L is the length of the antenna, and λ is the wavelength.

However, note that **we cannot control** which direction this antenna should point, i.e., it is not within our control which target to image.

A possible solution would be to implement a rotation system for the irradiation element, i.e., mechanically rotate the radiator so that its length is perpendicular to the direction of the target to be imaged - thereby ensuring maximum irradiation. A rotation system at the center of the radiator would develop the following torque:

$$|\vec{\tau}| = I|\vec{\alpha}| = \frac{ML^2}{12}\alpha \Longrightarrow \frac{\sigma L^3}{12}\alpha$$

Where $M = \sigma L$ is the mass of the radiator, L its length, σ its linear density, I the moment of inertia of the linear radiator, and α the magnitude of the angular acceleration applied to the device by the rotor. Note that, for a radiator that would need to measure just a few meters, the torque would depend on the cube of its length. Additionally, satellite imaging needs to change images quickly, which would push α to astronomical values, making such an electromechanical system energetically impractical.

Therefore, a purely electrical system must be used to select the direction of irradiation, and hence we resort to the use of **Antenna Arrays**.

2.3 Antenna Array

Until now, we have only considered the use of one, and only one, device for the emission of electromagnetic waves. However, through the use of multiple antennas, we can manipulate the electric currents of each unit to generate a composite electric field, this field meeting the acquisition requirements we desire.

2.3.1 Composite Field of Array

Consider N parallel irradiators, spaced a distance δ apart, along the same axis. Imagine that each irradiator is fed with a current $I_k = \Gamma_k \cdot e^{j\phi_k}$, where Γ_k is the module of the current phasor, ϕ_k its electric phase, and j the imaginary unit. This array of irradiators

is used to illuminate a target P, at a distance from each irradiator given by a vector $\vec{r_k}$. Fig. 2.3 illustrates the imagined scenario.

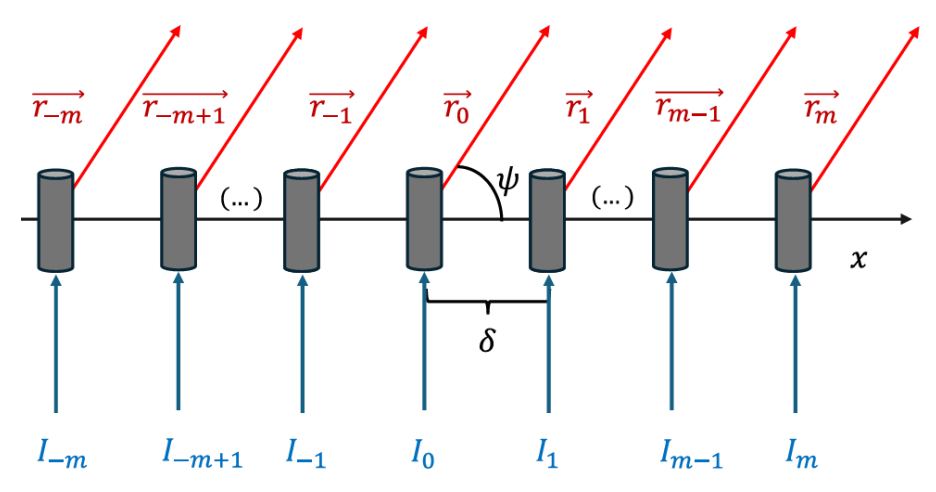


FIGURE 2.3 – Array of irradiators linearly spaced by a physical distance of δ . Each irradiator with index k is fed by a specific current $I_k = \Gamma_k \cdot e^{j(\phi_k)}$. When all are applied to the array antenna simultaneously, a composite electric field is generated by the vector sum of all individual electric fields. This final field is the one used to illuminate a specific direction by the antenna.

As the operators $(\nabla \cdot)$ and $(\nabla \times)$ in the relations 2.1 are linear, a phase shift of current ϕ_k leads to a phase shift of the electric field ϕ_k . Still considering that each irradiator, a priori, has its own electric field vector $\vec{e_k}$, as discussed earlier, the electric field at point P is given by the relation below.

$$\vec{E}_P = \sum_{k=0}^{N-1} \vec{E}_k = \sum_{k=0}^{N-1} \vec{e}_k(\psi) \cdot e^{jk_0 r_k + j\phi_k}$$

Since the antennas used in this work with will always be used in the Fraunhofer condition, that is, targets being imaged will always be far from the equipment, we consider $\vec{r_m} \angle \vec{r_n} = 0, \forall m, n$ — in other words, the vectors are parallel, so they make the same angle ψ with the horizontal axis. Therefore, the path difference between two irradiators m and n is $|\vec{r_m} - \vec{r_n}| = (m - n) \cdot \delta \cdot \cos \psi$.

Therefore, the resulting electric field updates to the following expression.

$$\vec{E}_P = \sum_{k=0}^{N-1} \vec{e_k}(\psi) \cdot e^{jk_0(r_0 + k\delta\cos\psi) + j\phi_k}$$

$$\iff \vec{E}_P = e^{jk_0r_0} \cdot \sum_{k=0}^{N-1} \vec{e_k}(\psi) \cdot e^{jk_0(k\delta\cos\psi)} \cdot e^{j\phi_k}$$

It is important to note that, for a given array configuration (δ and N fixed) and for a chosen direction of the target P, a designer has two sets of variables at their disposal:

the values of the electric fields of the irradiators $(\vec{e_k}(\psi))$, whose intensity and shape are associated with the geometry of the device used (immutable) and with the magnitude and behavior of the fed current; and the phase of the current provided to each irradiator (ϕ_k) . Therefore, we have $2 \cdot N$ free variables at our disposal, but in practice, it is more convenient to define them all through one relationship. In antenna arrays, it is commonly assumed that:

- $\vec{e_m}(\psi) = \vec{e_n}(\psi), \forall m, n$ that is, all the fields of the irradiators are identical because they are fed with currents of the same magnitude and distribution¹;
- $\phi_k = \phi_0 + k \cdot \Delta \phi$ the phases of the fed currents are ramped.

Considering these conditions, the development of the combined field expression follows:

$$\Longrightarrow \vec{E}_P = \underbrace{\vec{e_0}(\psi) \cdot e^{(jk_0r_0 + \phi_0)}}_{\vec{E}_0(\psi)} \cdot \sum_{k=0}^{N-1} e^{j \cdot k \cdot \underbrace{\left(k_0 \delta \cos \psi + \Delta \phi_0\right)}_{\Psi}}$$

Note how this unravels into a geometric progression sum, such that

$$\sum_{k=0}^{N-1} \exp(j \cdot k \cdot \Psi) = \frac{1 - \exp(j \cdot N \cdot \Psi)}{1 - \exp(j \cdot \Psi)} = \frac{\sin(N\Psi/2)}{N \sin(\Psi/2)} \cdot e^{j(N-1)\Psi} .$$

The result is a complex number, with a certain module and a phase. Since the final phase of the electric field is of no interest - as the most important portion is the module of the electric field, we define the **Array Factor** of the antenna array as

$$F(\Psi, N) = |\sum_{k=0}^{N-1} \exp(j \cdot k \cdot \Psi)| = \frac{\sin(N\Psi/2)}{N\sin(\Psi/2)}.$$
 (2.16)

The array factor is dependent primarily on the number of irradiators (N) and the distance of each element from each other (δ) . When applied to all angles in a spectrum, it may be called as **Array Function**.

The **Array Factor** $F(\Psi, N)$ is a multiplier associated with the array, which reduces the magnitude of the composite field for angles $\psi' \neq \psi$, being maximum at the angle of interest (ψ) , the angle of target P). But for this pointing to be valid, Ψ must maximize the Array Factor when the antenna points directly at P at an angle ψ .

The maximization of $F(\Psi, N)$ occurs for $\Psi = 2 \cdot q \cdot \pi, q \in \mathcal{Z}$. For all non-zero values of q, we will have non-global field maxima that will later be called *Grating Lobes* —

 $^{^{1}}$ The isometry of the radiated fields is not a *sine qua non* condition. We can select electric fields for different purposes, such as side-lobe suppression through the use of fields in a binomial distribution.

directions that will be illuminated by the array, but undesirably, contaminating the signal from the imaged target.

For q=0, we maximize the field function for the angle ψ , leading to the relation 2.17.

$$\Delta \phi_0 = -k_0 \delta \cos \psi \tag{2.17}$$

The relation 2.17 provides a means to focus the electric field of the antenna array in the angle ψ , simply by selecting as the angular ratio of the currents used to feed the array what the relation describes.

Thus, the final expression of the composite electric field resulting from the association of radiators in the array is given by equation 2.18.

$$\vec{E}_{network} = \vec{e}_{irr}(\psi) \cdot \frac{\sin(N\Psi/2)}{N\sin(\Psi/2)}$$
(2.18)

Finally, note that there is no need to know the nature of the field of the radiator that composes the array (\vec{e}_{irr}) —the radiator can be a short dipole, a Yagi-Uda antenna, or even another antenna array with M elements, allowing for a more complex field with more control variables (N and M), as long as $\delta_M \ll \delta_N$.

The great advantage of using an antenna array is the ease with which we can focus the field in a desired direction without significant operational, energy, or engineering costs.

And it is this technology—known as Array Antenna—that is behind satellites such as Tandem-X, TerraSAR-X, and ROSE-L (soon to be launched), enabling different methods of acquiring images of the Earth's surface in a highly versatile manner. These include the spotlight method (or Staring Spotlight Mode), which corrects the antenna angle direction during the satellite's passage, or even the Concurrent Mode, in which the antenna's illumination direction alternates between two completely distinct ground regions thousands of times per second—something simply impractical with an electromechanical technique.

As an illustration, Fig. 2.4 evaluates a scenario in which a designer uses an antenna array to receive signals from a target, requiring the antenna to be pointed at an angle of 1.0° from the **boresight** direction (that is, the main direction of the array's component element)

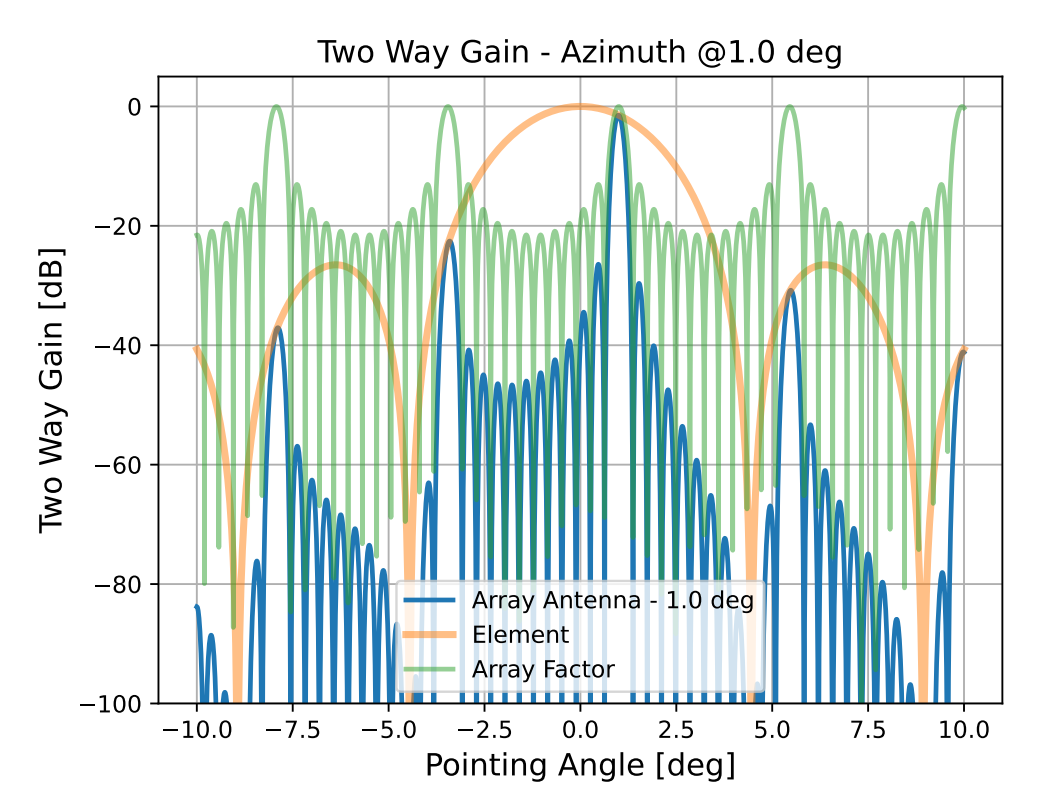


FIGURE 2.4 – Irradiation diagram of an antenna array, which points in a direction of $+1.0^{\circ}$ the element's maximum power direction (called *boresight*, in blue), the original radiation diagram of a single radiating element (in orange), and the multiplicative factor of the *Array Factor* (in green), which is applied throughout the radiator's diagram.

Fig. 2.4 illustrates the usefulness of the antenna array system: the ability to manipulate the distribution of the radiated electric field to maximize power intensity in areas of interest, without being limited by the nature of the radiator.

2.4 Grating Lobes

While using an antenna to focus energy transmission to a particular direction of interest, the use of an array leads to a side effect. The change in angle direction is associated with the displacement of the **Array Function**. For all the maximum values of $F(\Psi, N)$, the value Ψ must be so that $\Psi = 2\pi q$, where $q = 0, \pm 1, \pm 2, \ldots$ The central lobe is the intended direction of the target (q = 0), and all the other directions are not of interest.

As Fig. 2.4 shows, the array factor of each angle multiplies the element irradiation pattern on each point, producing a composite antenna diagram. The main lobe of the distribution (q = 0) has the highest amount of power throughout the plot, and all other peaks, which derive from other array factor maximum values $(q = \pm 1, \pm 2...)$ have smaller two-way gain.

The total power attributed to each array factor peak is given by the value, on that specific angle, of the element power diagram. When the target of interest is located at boresight ($\alpha = 0$), there are no grating lobes, as the maximum values of the array function coincide with the nulls of the element irradiation pattern.

However, as the intended target direction deviates from boresight, so does the whole array function, providing bigger power values to unintended directions, instead of the intended target, as shows Fig. 2.5.

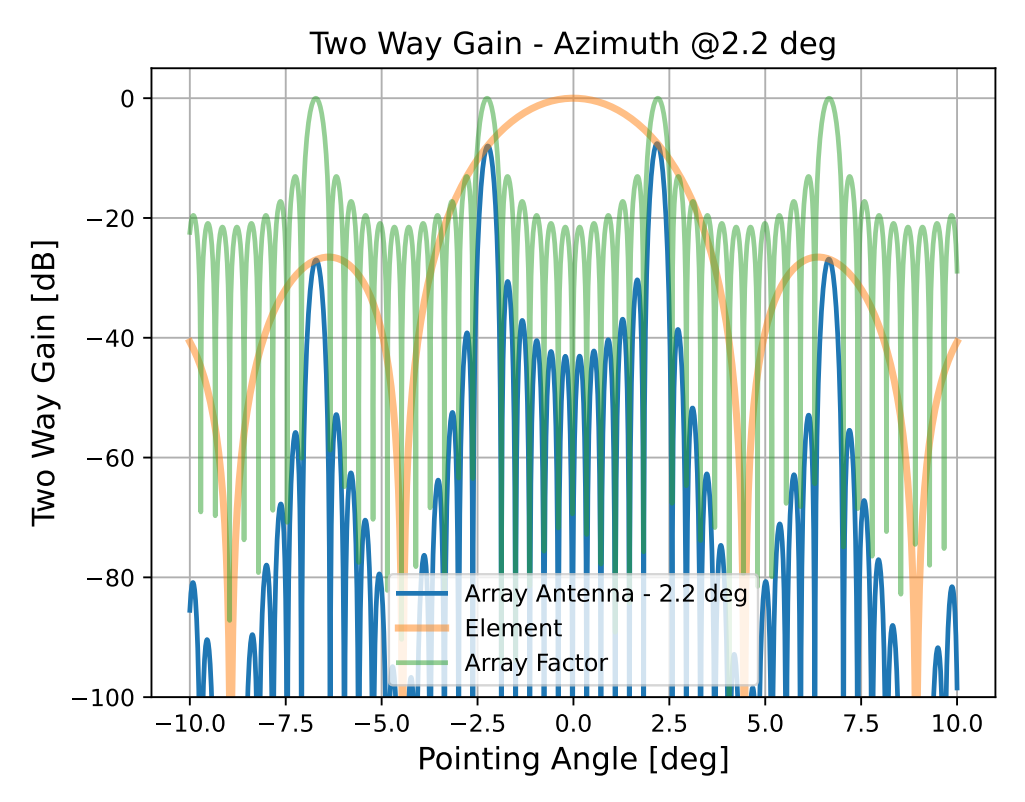


FIGURE 2.5 – Irradiation diagram (in blue) for the same antenna array of Fig. 2.4, but with a pointing angle of $+2.2^{\circ}$. Note how the array gain displays two power peaks: one at $+2.2^{\circ}$ (our intended direction) and -2.2° . This other power peak is unintended, as it's called a **Grating Lobe** - a byproduct of the shift in pointing angle, which shifts the array factor curve (in green) to the right, being modulated in value by the element irradiation diagram (in orange).

These lobes are called **Grating Lobes** and are a sub-product side-effect of antenna array technology. They present a problem because they leak energy to unintended spots on the ground, and if the pointing angle of the antenna is too far-off the *boresight* direction (0°) , their power will become comparable or even greater than the power released to the Main Lobe. In other words, a different, undesired region of the ground will be mapped in tandem to the target scene, and both signals will be acquired at the same time, leading to overlapping and therefore an unusable image.

The existence of grating lobes may also heavily impact the performance of target recognition and especially image acquisition, as the ratio of received power by the antenna be-

tween target and other ambiguous points ($Range\ Ambiguities$ and $Azimuth\ Ambiguities^1$) increases, reducing the amount of reflected power by the target in favor of unintended ambiguous regions.

This limits how far of *boresight* a system designed with an array antenna may point to, being the core reason of the steering angle limits of the *Spotlight* acquisition technique, which will be dissected in Chapter 3.

After this brief introduction to electromagnetism and the operation of the antenna embedded in satellites, we can now delve into the study of radars. For further information on antenna theory and design, we suggest further reading with (Balanis, 1997).

2.5 Introduction to Radars

The general operation of a radar is surprisingly intuitive. Similar to a sonar, a radar is a device capable of emitting electromagnetic waves to detect the position of a target at a given moment and, with more advanced techniques, determine more complex characteristics of that target, such as speed and composition. A deeper study, and a reference book for the concepts here introduced, can be found at (Sullivan, 2004).

2.5.1 Transmission (Tx) and Reception (Rx)

The basic detection mechanism is based on measuring the echo time of transmitted pulses. Given a target located at a point P, at a distance r_p from the radar, a pulse transmitted by the system takes τ to return.

Thus, the distance from the target to the radar is given by equation 2.19.

$$r_p = c_0 \frac{\tau}{2} \tag{2.19}$$

A radar system routinely sends pulses, as the position or size of the target may change (either due to the movement of the target itself or the radar, or even if the target is an extensive body with an irregular shape, such as a mountain or a building). Thus, the system transmits pulses ($\mathbf{T}\mathbf{x}$) using its antenna for a duration τ_p , called the **Pulse Width**, and then interrupts transmission for a period τ_e to receive echo signals ($\mathbf{R}\mathbf{x}$), an interval known as the **Echo Window**. This process repeats, with the time interval of this procedure known as the *Pulse Repetition Interval* (\mathbf{PRI}), and its inverse as the *Pulse Repetition Frequency* (\mathbf{PRF}).

¹Both Range and Azimuth Ambiguities will be explained in Chapter 3.

Fig. 2.6 illustrates the continuous pulse transmission process of a generic radar system.

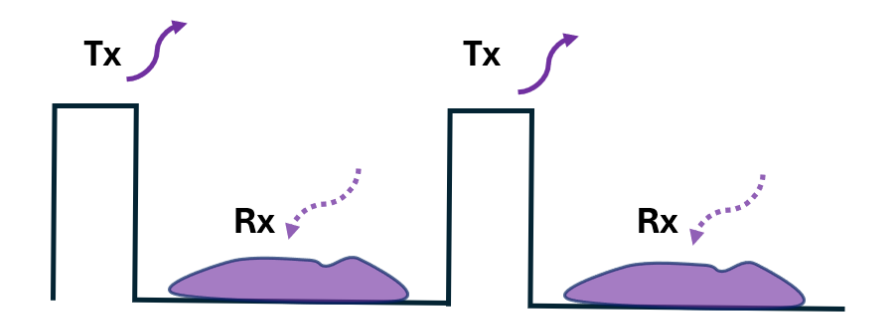


FIGURE 2.6 – Diagram of a conventional radar's *Echo Window*. Pulses are transmitted (\mathbf{Tx}) , with a width of τ_p , periodically in a time interval of PRI. During this interval, no signal is sent to accommodate received signals (\mathbf{Rx}) .

In other words, we can say that:

$$\tau_p + \tau_e = PRI$$

$$PRF = \frac{1}{PRI}$$

The higher the PRF of the transmission system, the more precise the location of a point target in space. However, as we will see later, the pulse transmission rate must be carefully managed, as increasing or decreasing it can cause spurious signals to interfere with the target signal.

Measuring the target's distance is only part of the localization process, as an entire geometric locus (a spherical surface) satisfies this condition.

However, by using techniques derived from gain analysis $(G(\theta, \phi))$, it is possible to precisely locate an imaged target.

2.5.2 SNR

The quantity SNR - Signal to Noise Ratio - measures the ratio between the energy or power of a signal of interest and the energy or power of the added noise.

Noise is an unwanted signal added to the received signal, originating from sources and communication channels. It arises from signal propagation through the atmosphere, the thermal noise of transmission and reception antennas, and other sources.

The energy of the noise signal in a communication channel is given by

$$E_n = kT_s C_b (2.20)$$

Where C_b is the bandwidth factor of the signal, associated with each frequency in the noise spectrum, T_s is the temperature, and k is Boltzmann's constant.

As mentioned in previous sections, it is a fact that the power distribution emitted by a transmitting antenna is not isotropic concerning the polar and nutation angles (θ, ϕ) , this anisotropy being accounted for by the gain function.

In a specific direction between the antenna and the target \mathbf{T} , given by $[\theta_T, \phi_T]$ and with a gain $G := G(\theta_T, \phi_T)$, we calculate the energy transmitted by a pulse. According to the definition of the **Poynting vector**, which represents the amount of power transmitted through an infinitesimal area in the propagation direction, we obtain relation

$$|\vec{S}(\theta_T, \phi_T)| = \frac{P_{\text{Tx}} \cdot G(\theta_T, \phi_T)}{4\pi R^2} . \tag{2.21}$$

The transmitted wave propagates through space, reaching the target of interest.

This target will have, in the direction of incidence of the emitted wave, an absorption and reflection value intrinsic to the nature of the material, a nature composed of its geometry and the material from which it is made. This value is called the *Radar Cross Section* (σ)—abbreviated as RCS—which measures the fraction of power scattered in the direction of incidence. In other words, we establish the RCS of a target through the equation

$$\sigma = \frac{S_{\text{scat}}}{S_{\text{inc}} \cdot 4\pi R^2} \ . \tag{2.22}$$

For our purposes, we can rearange 2.22 as

$$S_{\text{scat}} = \frac{\sigma_T \cdot S_{\text{inc}}}{4\pi R^2} \ . \tag{2.23}$$

Therefore, the total received power flux, assuming no loss along the path, is the product of the magnitudes of the Poynting vectors.

To calculate the total power absorbed by the receiving antenna, considering an antenna with an effective area A_e and a loss factor L throughout the entire path, the received power is given by

$$P_{\rm Rx} = S_{\rm inc} \cdot S_{\rm scat} \cdot \frac{A_e}{L} = \frac{P_{\rm Tx} \cdot G \cdot A_e \cdot \sigma_T}{16\pi^2 R^4 L}$$
.

From Antenna Theory, the effective area is given by $A_e = \frac{G \cdot \lambda^2}{4\pi} = \eta A$, where A is the antenna area and λ is the wavelength.

Thus, the final received power is given by

$$P_{\rm Rx} = \frac{A^2 \eta^2 \sigma_T}{4\pi R^4 \lambda^2 L} P_{\rm Tx} \ .$$

The received energy is the product of the received power and a given amount of time.

What is the time that should be multiplied? This is an interesting question. The concept of dwell time, or observation time, is routine in radars, referring to the period during which a target is observed. Normally, during this period, multiple pulses are sent to the target, but in our case, we are considering only a single pulse. Thus, the time used is the fraction of the PRI in which the pulse remains active—the pulse width τ_p . Considering $\Gamma = \frac{P_{Rx}}{P_{Tx}}$, the received energy is computed as $E_{r,single} = \Gamma P_{peak} \tau_p$ for a single transmitted pulse, and $E_{r,mult} = \Gamma < P > t_{dwell}$ for an observation period in which multiple pulses are transmitted.

Finally, we can calculate the SNR as the ratio between the received energy and the noise energy.

$$SNR = \frac{P_{Rx}}{E_n} = \frac{\langle P \rangle A^2 \eta^2 \sigma_T t_{\text{dwell}}}{4\pi \lambda^2 R^4 k T_s C_b L}$$

Or, in terms of gain:

$$SNR = \frac{\langle P \rangle G^2 \sigma_T t_{\text{dwell}}}{64\pi^3 R^4 k T_s C_b L}$$
 (2.24)

Eq. 2.24 is the Radar Equation, fundamental in the theory of these devices. It dictates the amount of signal returning from the target as a function of its nature, distance, observation duration, and, of course, the alignment between the radar's line of sight and the target, manifested in the equation by the parameters G and σ_T .

The SNR is, therefore, one of the main tools for target localization. While the return time provides us with the radial distance of a target to a radar device, the SNR facilitates its identification on a sphere of radius R, through the analysis of the received power and the *boresight* direction of the antenna.

2.5.3 Point-Target Localization

Thus, while temporal analysis provides us with radial distance, the study of SNR, together with other analyses, gives us the angular location of the target (θ_T, ϕ_T) .

In a more mathematical sense, we could say that extracting the position of a point target in a spherical coordinate system (ρ, θ, ϕ) follows the system of equations of the point target

$$T = (x_T, y_T, z_T) = \begin{cases} x_T = \rho_T \sin(\phi_T) \cos(\theta_T) \\ y_T = \rho_T \sin(\phi_T) \sin(\theta_T) \\ z_T = \rho_T \cos(\phi_T) \\ \rho_T = \frac{c}{2} \Delta t \end{cases}$$
 (2.25)

2.6 Wave Interaction with Materials

One of the discussed ways in which a wave generated by radar instruments accounts for interaction with a target or structure is through the parameter σ . In fact, the RCS (Radar Cross Section) is capable of evaluating how much of the incident power at a given point of the target, in a specific reflection direction, returns to the emitter.

Note, however, that the σ factor, for a given set of fixed parameters, is scalar, meaning it only influences the amplitude of the received wave.

There are other, more complex interactions that a material can establish with the incoming wave, and consequently, different ways that the received wave can encode this interaction.

The two main parameters of a returned electromagnetic wave capable of characterizing the illuminated target are:

- The amplitude of the wave, which internally encodes the distance to the target ($\frac{1}{R^2}$) and the target's RCS;
- The phase shift $\phi(t) = \frac{4\pi t}{\lambda} + \Delta \phi$; and

The phase shifts reveal the nature of the material, while the amplitude encodes both the distance to the target and its reflective characteristics.

In the next subsections, we will consider sending a monochromatic wave of the form $E(t) = \frac{E_0}{4\pi r^2} \cdot \cos(\frac{2\pi r}{\lambda} + \omega t + \phi_0)$, with $\phi_0 = 0$ for $t = t_0 = 0$, λ is the wavelength of the emitted signal, and r the radial distance from the emitter to a given distant point.

2.6.1 Amplitude

For an observer far from the original emission point of an electromagnetic wave, it is evident—according to the **Fraunhofer** criterion—that it will be perceived as a plane wave (TEM wave). Perceiving it as a plane wave may lead one to assume that there is no power dissipation, but this is a misconception.

For a given spherical wave, at a distance from the emitter where R >> L, L being the antenna's length, the variation of the field with respect to a change in distance Δr may be determined by analyzing the difference in electric field at small differences in distance.

$$\begin{split} \Delta \vec{E} &= \vec{E_{r+dr}} - \vec{E_r} \;, \\ \Delta \vec{E} &= \frac{\vec{E_0}}{4\pi (r+dr)^2} \cdot \cos(\frac{2\pi (r+dr)}{\lambda} + \omega t) - \frac{\vec{E_0}}{4\pi (r)^2} \cdot \cos(\frac{2\pi (r)}{\lambda} + \omega t) \;, \\ \Delta \vec{E} &\approx \frac{-dr^2 \vec{E_0}}{4\pi (r)^2} \cdot \cos(\frac{2\pi (r)}{\lambda} + \omega t) \;. \end{split}$$

As, r >> dr, then $\Delta \vec{E} \approx 0$.

The previous development displays the low level of variability of the electromagnetic field, for large distances. Hence, any reflection which takes place at a point of the material's structure may be computed as a multiplying factor σ . The loss factor per distance $(\frac{1}{4\pi r^2})$ usually is defined as a scalar A := A(r).

2.6.2 Phase Shifts

Given an extended body as a target, such as a lake, a forest, or a building, each material distorts the signal's wavelength to a value different from the one emitted. This distortion causes a phase difference in the wave that travels through this medium.

Consider a wave that travels a distance r (round trip) without any interference from detection material. Its phase will follow the expression:

$$\phi = \frac{4\pi r}{\lambda_0} \ .$$

Let L be the length of a structure, in the radial direction, made of material different from air/vacuum, and let λ_m be the wavelength assumed by the wave while passing through the structure of this material. The final phase of the wave upon return is given by:

$$\phi' = \frac{4\pi(r-L)}{\lambda_0} + \frac{4\pi(L)}{\lambda_m} ,$$

$$\Delta\phi = -\frac{4\pi L}{\lambda_0} + \frac{4\pi(L)}{\lambda_m} \; ,$$

$$\therefore \boxed{\Delta \phi = \frac{4\pi L}{\lambda_0} (\frac{\lambda_0}{\lambda_m} - 1)} \ .$$

Note that the phase difference is capable of directly computing the size of the imaged structure in the radial direction. This concept is key in interferometry, a technique widely used in radar systems, especially in synthetic aperture radar (SAR).

It is important to remember that the structure of the material can also contribute an additional phase shift during the interaction. This extra addition—linked both to the radial length of the target and the nature of its structure—allows engineers and technicians to assess the composition of the sample through its **angular deviation rate** per meter, a quantity that can be roughly modeled by a constant k_m .

In other words, the final phase deviation can be expressed as directly dependent on the length of the structure and its intrinsic electrical parameters:

$$\Delta \phi = \frac{4\pi L}{\lambda_0} \left(\frac{\lambda_0}{\lambda_m} - 1 \right) + \psi_0 ,$$

$$\Delta \phi = \frac{4\pi L}{\lambda_0} \left(\frac{\lambda_0}{\lambda_m} - 1 \right) + k_m \cdot L ,$$

$$\Delta \phi = L \cdot \left(\frac{4\pi}{\lambda_m} - \frac{4\pi}{\lambda_0} + k_m\right) ,$$

$$\therefore \boxed{\Delta \phi = L \cdot \zeta(\lambda_m)}.$$

Where we can define $\zeta := \zeta(\lambda_m)$ as a function which synthesizes all physical properties of the material.

These dielectric and length properties of the materials with which the emitted signals interact are used to interpret the underlying panorama of the image being acquired. By leveraging these and other properties (such as polarization plane shifts, not discussed in this thesis), a radar-embedded system with processing capabilities can understand the type of structure that reflected said electromagnetic signal. There are tables of dielectric properties, and by interpolation and estimation, one can deduce if the emitted wave

interacted with canopy, sand, water, ground, cement or other kind of material.

This is the main workframe to acquire large swaths of scenery on the Earth's surface, and build comprehensible images for the human eye to visualize.

The final piece of image composition to comprehend is the resolution and coverage conundrum on radar imaging.

2.7 Resolution and Coverage

When tackling remote sensing, especially when acquiring more than just a point with an angle spectrum but an extended body - such as a landscape - we do need to be able to identify two distinct points within its length, as well as knowing how large can our scanning be, given the radar parameters used in the process. The variables with account for these aspects are, respectively, **resolution** and **coverage**.

2.7.1 Resolution

Resolution is the quantity associated with the ability to resolve — that is, to distinguish — between two points, without loss or confusion of information. It states the minimum distance, in a given axis, that two points must be from each other in order to be recognized as separate entities.

To resolve two distinct targets, T_1 and T_2 , separated by a distance d, consider a pulse originating from a radar at point O, such that O, T_1 , and T_2 are collinear and T_1 is closer to O than T_2 . The emitted pulse has a temporal width τ_p . Fig. 2.7 displays the established scenario.

Note that if the distance d between the targets is sufficiently large, the radar will receive two distinct pulses at different times. In other words, the two points will be easily distinguishable.

On the other hand, if that same distance d is small, the pulse reflected from T_2 will not be sufficiently separated in time from the pulse reflected by T_1 . As a result, these two pulses will be received as a single pulse—with a longer duration and an irregular intensity pattern. This means that we cannot, a priori, resolve the targets.

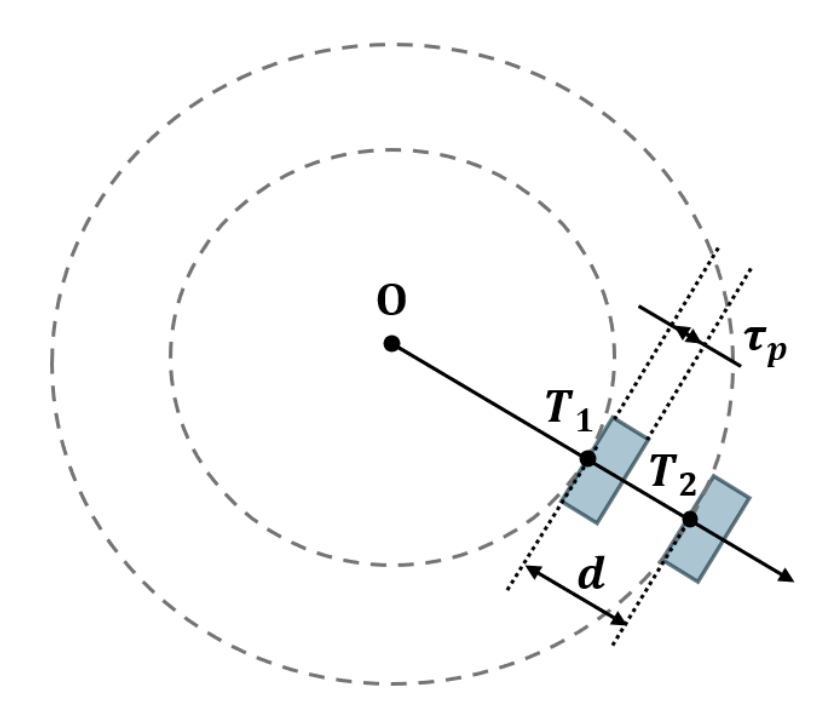


FIGURE 2.7 – Depiction of the emission of pulses from source O. Two wavefronts are highlighted, with points T_1 and T_2 both collinear to O. τ_p is the temporal width of the pulse emitted (in blue), and d the spatial distance between T_1 and T_2 . If d is too small, both points would be mapped by the same pulse, within the same τ_p , being indistinguishable from each other. Hence, there must be a minimal distance between the two points (radially) for them to be resolved as two separate points, and not mistakenly interpreted as the same one.

It is straightforward to observe that there is a threshold of distinction, which is the threshold beyond which two return pulses do not merge into one.

This condition is satisfied when the time difference between the reception of the pulse from T_1 and that from T_2 is greater than the pulse width τ_p .

Thus,

$$t_2 - t_1 = \frac{2 \cdot d}{c} = \Delta t > \tau_p ,$$

$$d > \frac{c \cdot \tau_p}{2} .$$

In this way, if d satisfies the condition above, we say the targets are resolvable.

Therefore, the system resolution, which is the minimum radial distance that two points must maintain between them to be resolvable, is given by

$$\delta = \frac{c \cdot \tau_p}{2} \ . \tag{2.26}$$

Note that the fact that the distance between the targets is radial was emphasized.

This is necessary because if the three points are not collinear, the condition becomes more complex.

The idea behind equation 2.26 creates a boundary for radar systems in two different ways:

- 1. For two points which preserve a distance between them such that the projection of this distance onto the radial axis is not null, this projected distance must be greater than what is given by 2.26 so they can be distinguished in the original direction.
- 2. For any given direction such that the distance preserved from one point to another results in a net-radial distance smaller than what is given by 2.26 or even zero, we say these points are not resolvable in the original direction. This will lead to the constraint of unoptimal *Azimuth Resolution* in conventional radar systems, as we'll soon analyze in Chapter 3.

2.7.2 Coverage

As import as image resolution, the whole size of an acquisition is an important parameter in remote radar sensing, as acquiring the largest possible area of a landscape is extremely desirable.

The most important parameter when defining coverage is the **Swath Width**, or the size of the acquired image in the direction perpendicular to the movement of the radar platform (also called the **Range direction**).

Swath width is directly tied to the interval between two emitted (Tx) pulses. Fig. 2.6 depicts the trains of Tx pulses, and the received signals from the ground. If the PRF of transmission is too high, then narrower images can be acquired, as there will be no space (temporally) to accommodate such scans. If PRF is low enough, larger and larger swaths can be extracted, although it is impractical to lower indefinitely the frequency of emission, as it will increase spurious power coming from Range Ambiguities, as will be shown in Chapter 3.

TerraSAR-X can support at most 30 km of swath width in some acquisition modes, in the lower values of PRF allowed in its system. If a designer were to double the rate of pulses, then the maximum allowed swath width, at that particular rate, would be 15 km and no further.

It is common, however, to image smaller scenes than the maximum allowed width. This is done in such a way that reducing the echo window (thence, increasing PRF) does not alter the swath width of the acquired scene. In acquisition modes such as Staring Spotlight (later to be discussed in Chapter 3), the specified width is so small that even at

maximum PRF, the received signal is still narrow enough to fit tighter and tighter echo windows. This will also be one of the key reasons of success of the Extended Staring Spotlight in doubling the acquired area, as will be shown in Chapter 4.

2.8 Summary

In this introductory chapter, we've established the foundational concepts that must be understood to fully grasp Synthetic Aperture Radar - the niche technology that is the basis of this work.

With this brief overview of the main topics of antenna technology and radar systems, the basis is set for understanding Synthetic Aperture Radar, and the innovation proposed with the EST technique.

3 Synthetic Aperture Radar

With the basic fundamentals of antennas and radars defined, we may dive further into the main topics of this Bachelor Thesis.

Within the field of radar communication and remote sensing, many different technologies and techniques are leveraged to achieve finer image resolution and precision on target detection. The main differences among the radar methods come in various forms, but the core concepts of divergence are often related to the algorithms used to process the received signals and the physical properties exploited.

In this chapter we will first introduce the concept of Side-Looking Airborne Radar as a mean to organically transition towards Synthetic Aperture Radar. We will then discuss the more common methods of utilizing SAR technology to acquire ground image products and their trade-offs, until finally we discuss about one of the most recent breakthroughs in SAR theory and introduce Concurrent Imaging.

3.1 Side-Looking Airborne Radar (SLAR)

Also called Side-Looking Airborne *Real-Aperture* Radar, it is an image acquisition technique which embeds an antenna to an aircraft and points its beam towards the ground, but maintaining an *elevation angle* related to the vertical line that contains the aircraft and its projection on the ground at a particular instant (also called *Nadir Line*). Fig. 3.1 depicts the general geometry of a SLAR acquisition.

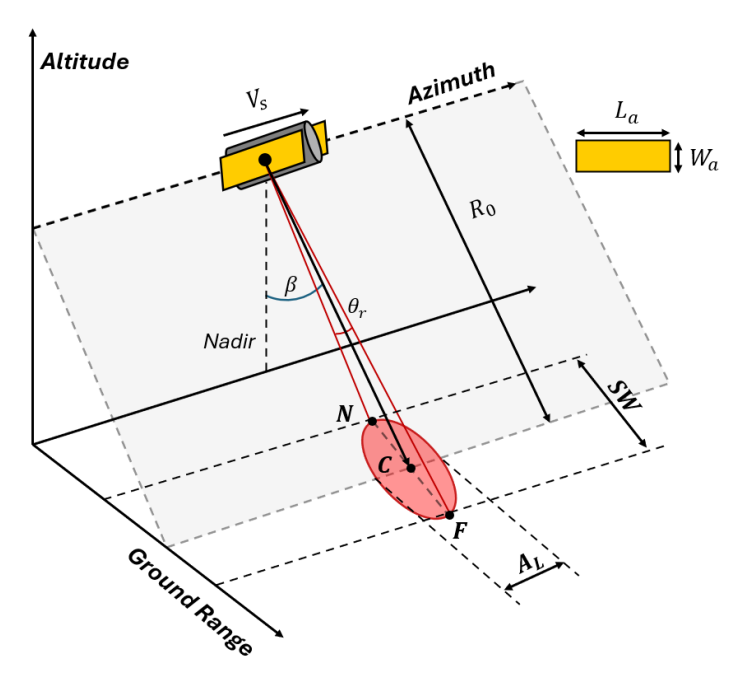


FIGURE 3.1 – Acquisition of a SLAR system. The platform moves with a constant velocity V_s and its direction of movement is the *azimuth* direction. It has embedded within it an antenna, of horizontal and vertical apertures of L_a and W_a respectively. The beam footprint of the antenna pulses (in red) has a near-range (\mathbf{N}) and a far-range (\mathbf{F}) extremes, as well as the scene center (\mathbf{C}). The distance between \mathbf{N} and \mathbf{F} is called the Swath Width (\mathbf{SW}) and A_L is the azimuth length of the footprint. Finally, R_0 is the slant range of the scene and $\theta_r \approx \frac{\lambda}{W_a}$ is the angular beam with in the range direction, with β standing for the elevation angle between the slant range and nadir. The grey plane is defined by the azimuth direction and the range direction.

Consider a platform with a SLAR radar, moving at a constant velocity of V_s . The direction of movement of the system is called azimuth direction, and the direction which contains the platform and the antenna target is the range direction. During the movement of the platform, the antenna constantly emits electromagnetic pulses, each of duration τ_p at a Pulse Repetion Frequency (PRF) of f_p to the Earth's surface. The antenna has its target center at point \mathbf{C} , called scene center, whose direction makes an angle of β (elevation angle) with the vertical which contains the platform and its projection on the ground, called Nadir. A wide region around \mathbf{C} is also illuminated, with points \mathbf{N} (nearrange) and \mathbf{F} (far-range) being the extremes of the beam footprint in the ground range direction.

It must be stressed: the antenna has a fixed pointing visage, not focusing on any particular landmark on the ground. Points N, C and F are defined as the near edge, center, and far edge of the beam footprint, regardless of where the footprint lands on the ground. This method of image acquisition was briefly introduced in Chapter 1 as the Stripmap mode, and will be studied later in this chapter.

The illuminated region has a Swath Width (SW) and an Azimuth Length (A_L) , both dimensions being related to the main lobe angular apertures of the antenna.

For a one-dimension antenna of length L emitting electromagnetic pulses with wavelength λ , the **HPBW** (Half-Power Beam Width) is approximately

$$\theta_{\frac{1}{2}power} \approx \frac{\lambda}{L}$$
.

Hence, the azimuth and range beam widths are defined as

$$\theta_a \approx \frac{\lambda}{L_a} \ , \tag{3.1}$$

$$\theta_r \approx \frac{\lambda}{W_a}$$
 (3.2)

We can calculate the dimensions of the illuminated footprint. For a given wavefront of the beam, its spread in a given dimension x (azimuth or range) is obtained by

$$S = \theta_x \cdot R_0 \approx \frac{\lambda R_0}{L_r} \ .$$

In the case of the azimuth length (A_L) we may say the azimuth spread of the beam is approximately equal to the azimuth length of the beam footprint.

$$A_L \approx R_0 \cdot \theta_a = \frac{\lambda R_0}{L_a} \ . \tag{3.3}$$

For calculating swath width, however, we need to considerate the deformation of the wavefront when reaching the ground. The geometry of the wavefront arrival on the ground is displayed in Fig. 3.2.

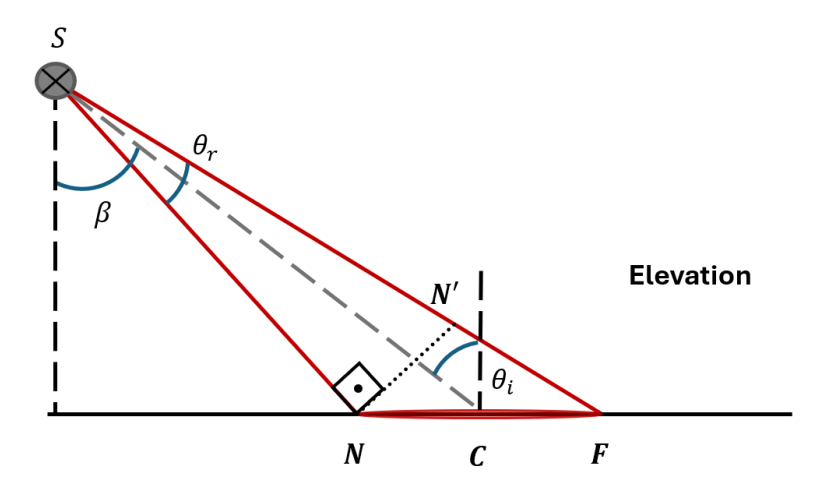


FIGURE 3.2 – Elevation geometry of pulse spread.

Fig. 3.2 depicts the same scenario of Fig. 3.1, but in the elevation plane. A pulse

emitted by the platform at S travels as a coherent wavefront (which can be approximated to a plane wavefront when close to the ground). When it reaches Earth, it does not do so with all points reaching it at the same time: the first point to reach it will do so at near-range \mathbf{N} , being reflected and then returning to the radar, while other points of the wavefront $\overline{NN'}$ still need to reach the ground. The last point of the wavefront will reflect on Earth's surface at far-range \mathbf{F} .

It is notable how the wavefront $\overline{NN'}$ is mapped to the beam width in ground range \overline{NF} . Using the geometry displayed, we can say

$$\overline{NN'} = \overline{NF} \cdot \cos \theta_i ,$$

$$\therefore SW = \overline{NF} = \overline{NN'}/\cos\theta_i$$
.

Since $\overline{NN'}$ is the spread of the signal just as it touches the near-range (**N**) onto the ground, the value of the ground range beam footprint is

$$\left| SW \approx \frac{R_0 \cdot \theta_r}{\cos \theta_i} = \frac{\lambda R_0}{W_a \cos \theta_i} \right|. \tag{3.4}$$

Note: We use θ_i and not the elevation angle β for generalization purposes. In the case of an aircraft platform, since the altitude of the flight is low when compared to Earth's radius ($\frac{R}{H} \approx 1000$), the geometry of the ground may be considered flat, hence $\theta_i \approx \beta$. However, when working with spaceborne SAR systems, this premise is non applicable, as the curvature of the planet is no longer negligible and the relation between θ_i and β is given by

$$\theta_i = \sin^{-1}((1 + \frac{H}{R}) \cdot \sin \beta)$$
 (3.5)

The range resolution of a radar system (whether a simple radar, SLAR, SAR or any other similar device), as previously explained in Chapter 2, is given by relation 2.26, where $\delta_r = \frac{c \cdot \tau_p}{2}$. However, this is in the *slant range* (radial) direction. When projecting this distance of resolvability onto ground range, we have:

$$\delta_{gr} = \frac{c \cdot \tau_p}{2 \cdot \sin \theta_i} \ .$$

However, this is far from solved. This equation, for normal values of τ_p , would lead to range resolutions in the spectrum of dozens of kilometers, which is not acceptable. One would need to produce pulses in the realm of microseconds just to have ground range

resolutions below one kilometer, which would limit the amount of energy being sent to the ground, requesting power peaks in the range of megawatts.

What is commonly done in radar technology is to compress the received pulse via usage of matched filters¹. This eliminates the necessity of sharply reducing the pulse duration and leverages the bandwidth of the received signal. Thence, **ground range resolution** is

$$\delta_{gr} = \frac{c}{2 \cdot B_w \cdot \sin \theta_i} \,. \tag{3.6}$$

Where B_w is the bandwidth of the base pulse utilized. Using TerraSAR-X with its 150 MHz of bandwidth as reference, for an incidence angle of 30°, $\delta_{gr} \approx 1$ m.

When it comes to azimuth resolution, since all points belong to the same wavefront (in the azimuth direction), there is no resolvability for any two points in the same line, if both lie within the beam footprint. In other words, the azimuth resolution is the spread of the beam footprint on the ground, as expressed by the relation below.

$$\delta_a \approx \theta_a R_0 = \frac{\lambda}{L_a} R_0 \ . \tag{3.7}$$

This limitation is acceptable for Side-Looking Airborne Radar, since R_0 usually is limited to at most 50 km. For a SLAR system operating at X-Band ($\lambda \approx 3$ cm) with a slant range of 20 km and an antenna with length $L_a=2$ m, the azimuth resolution would be $\delta_a \approx 300$ m, which is acceptable for many different applications. For a research airplane, at one kilometer altitude, resolution could go as high as $\delta_a=15$ m, an excellent quality parameter.

The image acquired by the radar will be processed in such a way that the resolutions given by 3.6 and 3.7 can serve as a grid. Any two landmarks acquired in a specific shot, in order for both to be distinguishable from each other (using resolvability as criteria), must preserve a distance of at the very least $\delta_{g,r}$ in range and δ_a in azimuth. Fig. 3.3 shows a snapshot of the beam footprint up close, with a grid of $\delta_{g,r} \times \delta_a$ on it.

¹Pulse compression is used for received signals, as the commonly utilized waveform in antennas, the *Chirp*, has a *sinclike* shape. When compressed with a matched filter, the main lobe becomes sharpingly stricter, therefore more well defined.

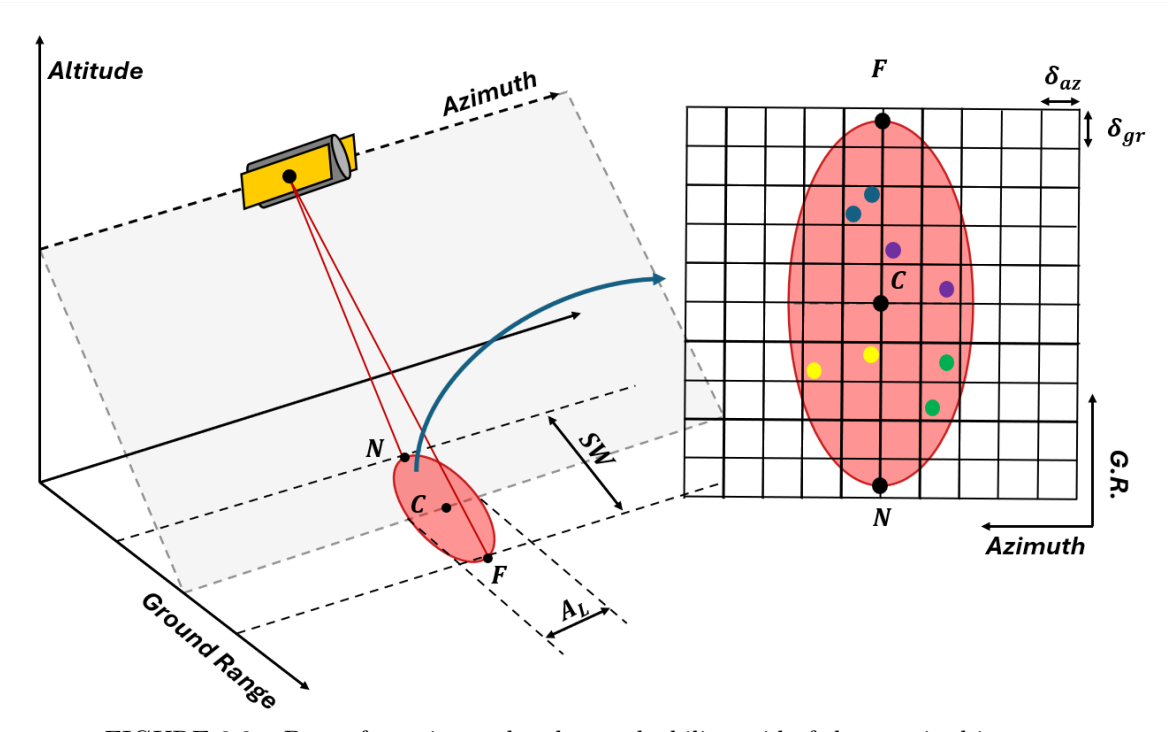


FIGURE 3.3 – Beam footprint under the resolvability grid of the acquired image.

There are four sets of landmarks onto the footprint: blue, green, yellow and lily.

- The blue landmarks are both in the same resolution pixel meaning they cannot be distinguished neither in azimuth nor in range, because they do not differ δ_a in azimuth nor $\delta_{q,r}$ in range.
- The yellow landmarks can be resolved in azimuth, as they have an azimuth distance between themselves of at least δ_a . However, they do not differ by $\delta_{q,r}$ in range.
- The green landmarks can be resolved in range, but not in azimuth, as they do differ by at least $\delta_{g,r}$ in range, yet the same cannot be said in azimuth, as they don't preserve a minimum of δ_a in this direction.
- Finally, the lily landmarks are completely resolvable, as they differ both in range and azimuth more then their respective resolution minimum thresholds².

Fig. 3.4 shows an approximate scenario of the received snapshot on the SLAR radar - only the lily landmarks are completely distinguishable from each other, as the rest are only partially resolvable at best, if at all.

²One final comment about resolvability in SAR-embedded systems: two points may be in different cells and still be unresolvable, as the grid is more of an approximate depiction of the necessary thresholds.

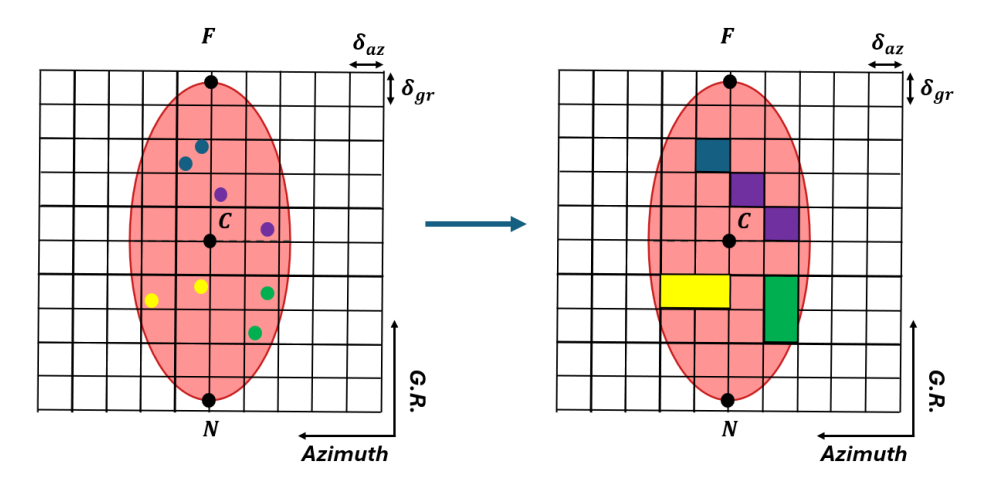


FIGURE 3.4 – Resolvability under the resolution grid - two objects not sufficiently apart from one another in one direction will not be resolved.

One limitation of a lower altitude SLAR acquisition: since the altitude of the moving platform is small (no higher than 10 km), the covered area illuminated by the beam is limited as well. It is interesting to ponder whether embedding a SLAR system into a spaceship could provide a far wider coverage, as the altitude would be dozens of times higher than a simple aircraft.

Unfortunately, as the coverage would increase, so would the minimum distance of resolvability - using the same equipment as previously, but at the altitude of a satellite such as TerraSAR-X, the azimuth resolution of such an acquired image would be such as $\delta_a \approx 8$ km, which is not tolerable.

The solution to the problem of the azimuth resolution for higher altitudes is provided by the usage of Synthetic Aperture Radar.

3.2 Synthetic Aperture Radar (SAR)

Synthetic Aperture Radar (SAR) is a subtype of SLAR radars, proposed in 1951 by Carl Wiley, which utilizes an airborne or spaceborne antenna for imaging with a frequency processing algorithm that enables the device to synthesize an artificial antenna length, using the platform's movement to enhance resolution.

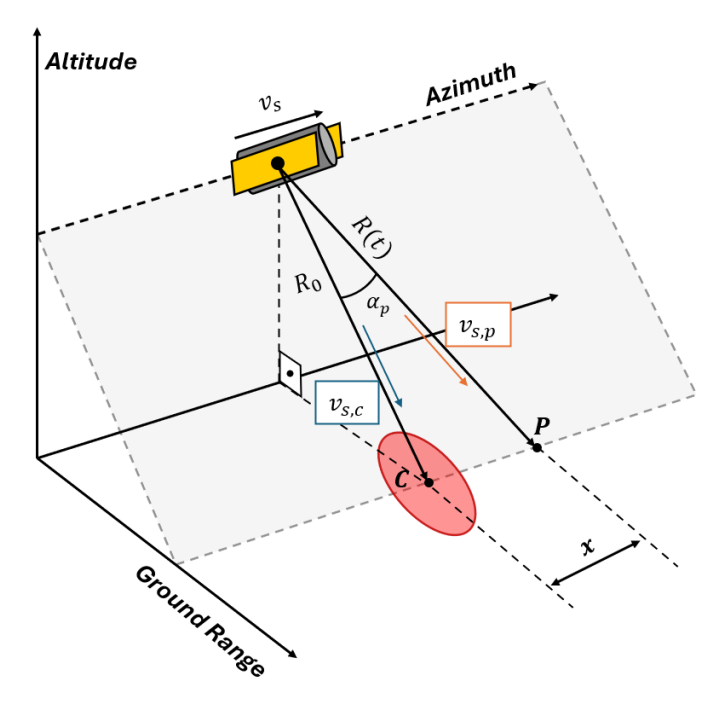


FIGURE 3.5 – Schematic of a SAR/SLAR acquisition, with \mathbf{C} as scene center and \mathbf{P} as particular point of interest, at the same range but x apart from it in the azimuth direction, forming an angle of α_p in along-track. $v_{s,c}$ and $v_{s,p}$ are the components of velocity v_s seen from \mathbf{C} and \mathbf{P} respectively, with R_0 being the slant range at maximum proximity of the platform with \mathbf{C} and R(t) the slant range of \mathbf{P} .

To understand how this improves azimuth resolution of a given acquisition, it is necessary to take into account the effect of the moving platform on the perceived frequency of received signals. The embedded antenna will be the exact same as the one in the previous SLAR example, for future comparison.

The movement of the platform inputs a *Doppler frequency shift* on all points of the received wavefront echoed from the ground, in the along-track direction. However, as all points on the ground are slightly off from each other by a small azimuth angle in respect to the platform, they will all have their unique frequency shifts.

Fig. 3.5 depicts the same scenario of a moving platform as Fig. 3.1, but we now focus on specific points in the along-track (azimuth) direction. For a given point \mathbf{P} , apart from the scene center \mathbf{C} of x in azimuth, its perceived velocity of the platform will change as it approaches its position - but much more importantly, every single point on the ground will see the platform velocity differently, along-trackwise. In the schematic, $v_{s,c} = 0$ and $v_{s,p}$ is a non-null velocity component, expressed by:

$$v_{s,p} = v_s \cdot \sin \alpha_p \ . \tag{3.8}$$

This is important, as it signals that, according to the Doppler Effect, **two different** points will have two different Doppler Frequency shifts from the nominal frequency f_0 of the emitted frequency pulse by the antenna.

If we recall the equation for the *Doppler Effect*, we can estimate the Doppler frequency shift.

$$\Delta f_P = f_0 \frac{v_{s,p}}{c} = \frac{v_s \sin \alpha_P}{\lambda_0} \ .$$

Nonetheless, since the signal is sent to point P (hence P senses a Doppler shift of Δf_P) and then P echoes the distorted signal back to the platform, which itself sees P move towards it with velocity $v_{s,p}$, the total frequency shift is doubled $(f_D = 2 \cdot \Delta f_P)$.

Hence, we have the total amount for the Doppler Shift given by:

$$f_D = 2 \frac{v_s \sin \alpha}{\lambda_0} \ . \tag{3.9}$$

Point **P** has a slant-range of R(t) when the satellite is the closest to \mathbf{C} ($\overline{SC} = R_0$). One key concept to solidify is that the variable t does not stand for the current instant, but for the time necessary to be at maximum proximity with \mathbf{P} ($\overline{SP} = R_0$). This implies that the distance \overline{CP} is obtainable as

$$\overline{CP} = x = v_s t . (3.10)$$

From the geometry of Fig. 3.5 and inputing 3.10, we have:

$$R(t)^2 = R_0^2 + v_s^2 t^2 ,$$

$$\therefore R(t) = \sqrt{R_0^2 + v_s^2 t^2} \ . \tag{3.11}$$

In most scenarios, whether the radar is carried by an aircraft or a satellite, $R_0 >> v_s t$. Hence, we may approximate R(t).

$$R(t) = R_0 \sqrt{1 + \frac{v_s^2 t^2}{R_0^2}} \approx R_0 + \frac{v_s^2 t^2}{2R_0}$$
.

The rate of change for the slant range of \mathbf{P} , which itself must be the velocity component of the satellite seen by \mathbf{P} , can be obtained via extracting the time derivative of R(t).

$$\frac{\partial}{\partial t}R(t) = \frac{\partial}{\partial t}(R_0 + \frac{v_s^2 t^2}{2R_0}) ,$$

$$\dot{R}(t) = \frac{v_s^2 t}{R_0} \ .$$

But, again, $\dot{R}(t) = v_{s,p}$. By 3.8, we obtain:

$$v_{s,p} = v_s \sin \alpha_p = \frac{v_s^2 t}{R_0} ,$$

$$\therefore \sin \alpha = \frac{v_s t}{R_0} = \frac{x}{R_0} \ .$$

Which could also be directly obtained via the trigonometry of the scheme, assuming $\sin \alpha \approx \tan \alpha$, which is valid since $v_s t \ll R_0$, as previously established.

Accounting for 3.9, we have the final result.

$$f_D = \frac{2v_s^2 t}{\lambda_0 R_0} = x \frac{2v_s}{\lambda_0 R_0} \quad . \tag{3.12}$$

The main takeaways from 3.12 are:

- 1. In the context of small areas of acquisition, where the condition $v_s t \ll R_0$ stays valid³, points with the same azimuth coordinate will have the same Doppler frequency shift, regardless of range distances.
- 2. Points on the ground can now be finely distinguished in azimuth even if both lie within the same beam footprint, which is an improvement from SLAR the satellite can analyze the frequency deviation from the nominal pulse frequency to distinguish two different points in azimuth, associating one frequency with one x position.

The limits of resolvability in azimuth (δx) are tied to how finely can a system distinguish two different frequencies (δf) .

Extracting the differential and rearranging equation 3.9:

$$\delta x = \frac{\lambda_0 R_0}{2v_s} \delta f \ .$$

How granular is the frequency discretization is dependent on the amount of time a received waveform is analyzed.

³This condition is necessary for the validity of 3.12, as the *locus* of all points on the ground with the same Doppler shift lie on a hyperbole, not a straight line. The azimuth coordinate will need to behave, alongside the range coordinate, to match this hyperbole *locus* to ensure it is an *iso-Doppler* shift curve.

$$\delta f = \frac{1}{T_{ill}} \ .$$

Where T_{ill} is the illumination time of a particular point on the ground, or the amount of time spent on analyzing a particular waveform. In a more practical sense, it can be viewed as the duration of time where a point on the ground is illuminated by the antenna beam footprint.

Since the number of pulses is discrete, one can view the illumination time as the number of frames or pulses taken by the radar system $(T_{ill} \propto N_{pulses})$ of the scene.

Henceforth, we arrive at

$$\delta x = \frac{\lambda_0 R_0}{2v_s} \cdot \frac{1}{T_{ill}} \,. \tag{3.13}$$

The main improvement of SAR systems, when compared to regular systems such as SLAR, is the possibility of leveraging the frequency shift to better resolve two different points in the azimuth direction, not being limited by the azimuth length of the antenna beam footprint on the ground. If we compare relations 3.13 and 3.7, we see the gain in performance.

$$\frac{\delta x_{SAR}}{\delta x_{SLAR}} = \frac{\frac{\lambda_0 R_0}{2v_s} \cdot \frac{1}{T_{ill}}}{\frac{\lambda_0}{L_a} R_0} = \frac{1}{2} \cdot \boxed{\frac{L_a}{v_s T_{ill}}}.$$

Since $L_a \ll v_s T_{ill}$, the resolvability of SAR is much finer than SLAR's. This comparison mathematically exposes the secret technique of Synthetic Aperture Radar and why it receives such name: from the perspective of a point on the ground, it is being illuminated by an antenna whose aperture (size) is the length traveled by the platform for all the time the point receives electromagnetic pulses, and not its real aperture of L_a . But since this antenna is not real, it is considered a synthetic aperture antenna, hence the radar system leveraging it is called a **Synthetic Aperture Radar**, yielding far wider apertures than any normal real aperture radars ever could.

Relation 3.13 is the main expression to extract the azimuth resolution of a SAR technique when the platform behaves similarly to a SLAR, and will be used to calculate the azimuth resolution of many acquisition modes.

3.3 Ambiguities

After dissecting SAR technology and its advantages, we must take a step back to better understand some of the major hurdles of working with this technique.

One of the most important side-affects of radar technology is the concept of ambiguous signals. When scanning a specific object or area, the returning signal from the intended direction will not be the only one to be received by the antenna.

While radars leverage antenna technology, whose main purpose is not only to translate electric pulses into electromagnetic waves, but also focus the injected power mainly to a particular direction, it is still necessary to recall that the electromagnetic pulses emitted in transmission do travel through the medium as a spherical wavefront (assuming an isotropic environment for propagation). The wavefront emitted from the satellite towards the ground will illuminate a large portion of the Earth's surface, not only the target scene.

All points illuminated on the ground will reflect the incident energy in all directions, and one of these directions is towards back to the satellite. For the majority of these points, the reflected energy is of no concern, so long as they do not interfere with the received energy directed towards the main scene of interest.

But for some specific spots on the ground, this is not the case. Certain specific positions on the ground will reflect power in such a way that **their reflected signals will overlap with the signal from the main scene**, and this will infect the target image by overlapping it with the attenuated images of these undesired regions. These spots are called **Ambiguities**.

In SAR technology, a common metric to study the level of ambiguity of an image is the **Ambiguity-to-Signal Ratio (ASR)**. It is defined as the ratio between the total power of ambiguities and the power reflected from the main scene.

$$ASR = \frac{\sum_{k=1}^{N} P_{amb,k}}{P_{target}} \tag{3.14}$$

Fig. 3.6 depicts the process of image infection. The ambiguities on the ground (in blue) reflect energy which will overlap with the main scene (in red), degrading the target scene by overlapping it with the signals from the undesired spots.

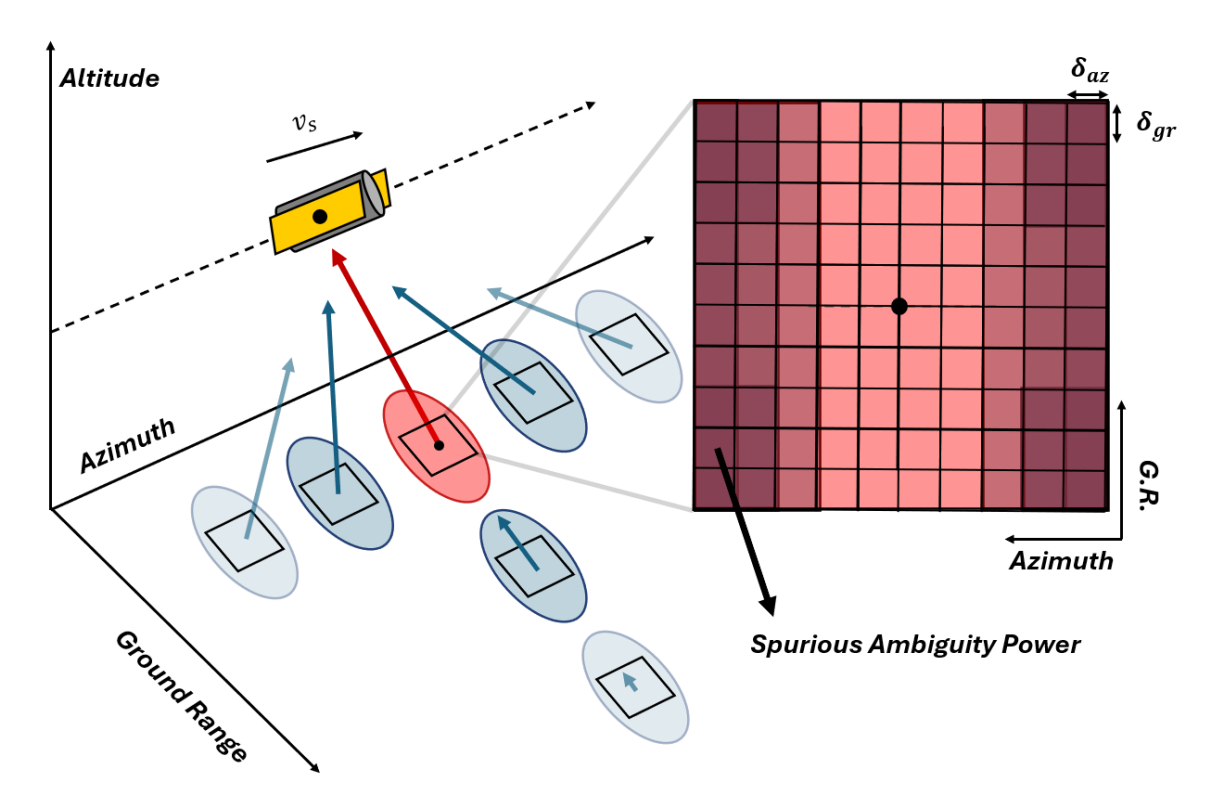


FIGURE 3.6 – Effect of reflected power from ambiguities (in blue) on the image of the focused scene (in red). These specific spots on the ground are positioned as such that their signals will overlap with the main scene's signal, leading to a degraded image. If the Ambiguity-to-Signal Ratio (ASR) is too high, the extract data is deemed not suitable and it is discarded. The darker pixels in the grid represent the ambiguities effect on the image extracted of the target scene - all should be red, but other blue scenes on the ground leak into the main scene, mixing with it and making it purple.

There are two categories of ambiguities pertinent to SAR imaging, each with its unique mechanism for signal interference: **Range Ambiguities** and **Azimuth Ambiguities**.

3.3.1 Range Ambiguities

When a satellite is utilized to scan a specific strip of Earth's surface, it will transmit thousands of pulses per second, not just a single unitary pulse. This is done so to increase illumination time and, therefore, resolution, but also to minimize noise and other outlining deviations from the expected standard image.

However, this mechanism brings a restriction.

Refer to Fig. 3.7, where a satellite at point S emits a train of pulses towards the surface of Earth. Since pulses travel in all directions, they will hit the ground in many different points, of which we highlight three: P, T and Q, where T is the target point, illuminated by the main lobe of the antenna, represented by the red cone. The red arrows are the first emitted pulse, the blue ones are the second pulse, and finally the green arrows represent the third and final transmitted pulse.

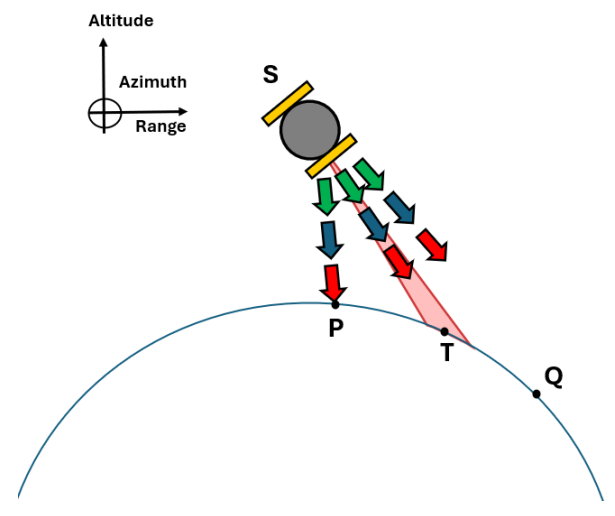


FIGURE 3.7 – Depiction of a satellite transmitting a train of pulses to points P, Q and T, in elevation. Point T is the acquisition target, since it is illuminated by the main lobe (in red). The train of pulses is colored such that the first transmitted pulse is red, the second is blue and the third is green. The satellite travels in azimuth, entering the paper plane.

After a few milliseconds, the pulses will hit P, T, and Q in their respective time-frames, with part of the incident power reflecting back towards the satellite. However, since the segments \overline{SP} , \overline{ST} , and \overline{SQ} have different lengths, the travel time of the train of pulses is different in each respective direction, as shown in Fig. 3.8.

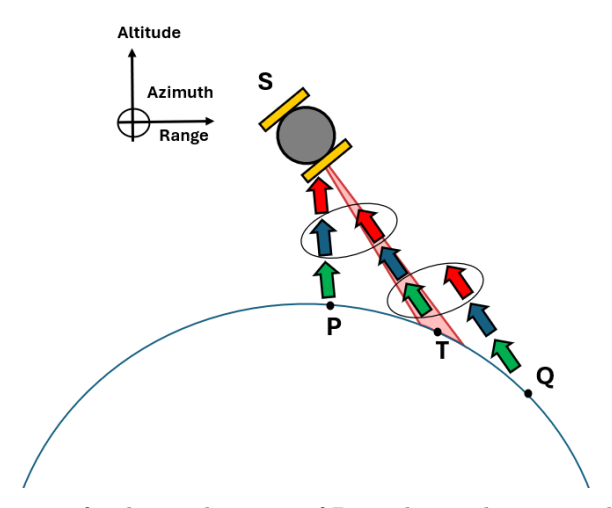


FIGURE 3.8 – Reflected trains of pulses. The train of P is advanced in one pulse related to T, while T is advanced in two pulses from Q. The circles show how these signals will now arrive in S at the same time, so it will have the reflected signals of P, T and Q mixed.

For the illustrated scenario, P is exactly one pulse ahead of T, and Q is two pulses behind T. The received signals will arrive precisely at the same moment in the echo window of the transmission diagram - in other words, they will overlap.

This happens because \overline{SP} and \overline{SQ} differ from \overline{ST} precisely enough to advance (or delay) the reflected train of pulses in P and Q with respective to the train of pulses in T by one

period and two periods (or Pulse Repetition Intervals), respectively.

P and Q are called Range Ambiguities of T - spots on the surface whose train of pulses will be shifted in reference to the intended target by a whole number of pulse intervals. These spots will, therefore, have the same timing as the target when received by the satellite and will be received in tandem, mixing the target with images of undesired points on the ground.

In other words, a point on the ground is a range ambiguity of T if its return time t_k is such that

$$t_k = t_0 + k \cdot PRI, \ k \in \mathbb{Z}^*$$

Where t_0 is the return time of the target's reflected signal and PRI is the pulse repetition interval.

We may convert this property to its version in distances, where for a given point target T, distant of S by R_0 (slant range of T), are considered Range Ambiguities all points on the surface whose distances from the satellite are given by

$$R_k = R_0 + k \cdot \frac{c_0 \cdot \text{PRI}}{2}$$
(3.15)

These are called "range" ambiguities because they emerge from the difference in path at the range/ground range axis. Differences in the azimuth position barely change the overall value of the *slant ranges* of ambiguities since the half-power beam width of the antenna's main lobe in azimuth is too narrow. Any other spots on the ground with the same timing as other range ambiguities, but in the azimuth direction, are too faint to detect⁴.

It must be noted that range ambiguities are not unique to SAR technology, being present in conventional RAR and SLAR systems.

3.3.2 Range Ambiguity-to-Signal Ratio (RASR)

When comparing the amount of ambiguity power to target power, it is useful to measure the ratio between them. For this, we often extract the Range Ambiguity-to-Signal Ratio (RASR) of the image, where the power sourced from all the range ambiguities is summed, and then compared with the received power from the desired scene. RASR calculation may vary its formulation depending on definition, and we decide to utilize the

⁴When addressing Staring Spotlight (ST), Extended Staring Spotlight (EST) and Concurrent Imaging, this is no longer truth.

equation

$$RASR = \frac{\sum_{k=1}^{N} P_{\text{amb, k}}}{P_{\text{target}}} = \frac{\frac{\sum_{k=1}^{N} G_{\text{two-way, k}} \cdot \sigma_k}{|\sin \theta_{i,k}| \cdot R_k^3}}{\frac{G_{\text{two-way, T}} \cdot \sigma_T}{|\sin \theta_{i,T}| \cdot R_T^3}}$$
(3.16)

- where N is the total number of range ambiguities on the ground, G is the two-way gain of the signal emitted by the satellite and reflected by the ambiguity point, θ_i the incidence angle, R_k the slant range (distance to the satellite) from point the k-th ambiguity.

In summary, range ambiguities are considered to be an unavoidable constraint of radar imaging, resulting from a time ambiguity of reflected pulses.

One of the main methods of reducing the effect of range ambiguities on the image's signal is to utilize higher values of PRI (or smaller values of PRF). However, this increase cannot be done indefinitely, as it increases also the number of Azimuth Ambiguities, which will be discussed next.

3.3.3 Azimuth Ambiguities

While range ambiguities are considered to emerge from a return time coincidence of pulses, and are a necessary hurdle to address for all radar systems, there is another kind of ambiguities that needs attention, and these are specific to SAR systems - **ambiguities** in frequency.

Consider Fig.3.9, where a satellite embedded with a SAR instrument begins the acquisition of a target scene, with attention to its center C. When emitting pulses to the ground, these will hit the surface of Earth in the same fashion as said previously - they will illuminate a much larger area than solely the acquired scene. When the satellite reaches its minimum distance to said center C (its slant range R_0), the firing frequency will be f_0 - the natural frequency of the generated pulse. However, to all other points in the azimuth direction, the relative velocity of the satellite to these points will not be null. This leads to a Doppler Shift taking effect on the signal sent to a particular point $P \neq C$, so the perceived frequency by $P(f_P \approx (1 \pm 2 \cdot \frac{v_s}{c}) \cdot f_0)$ is different than f_0 .

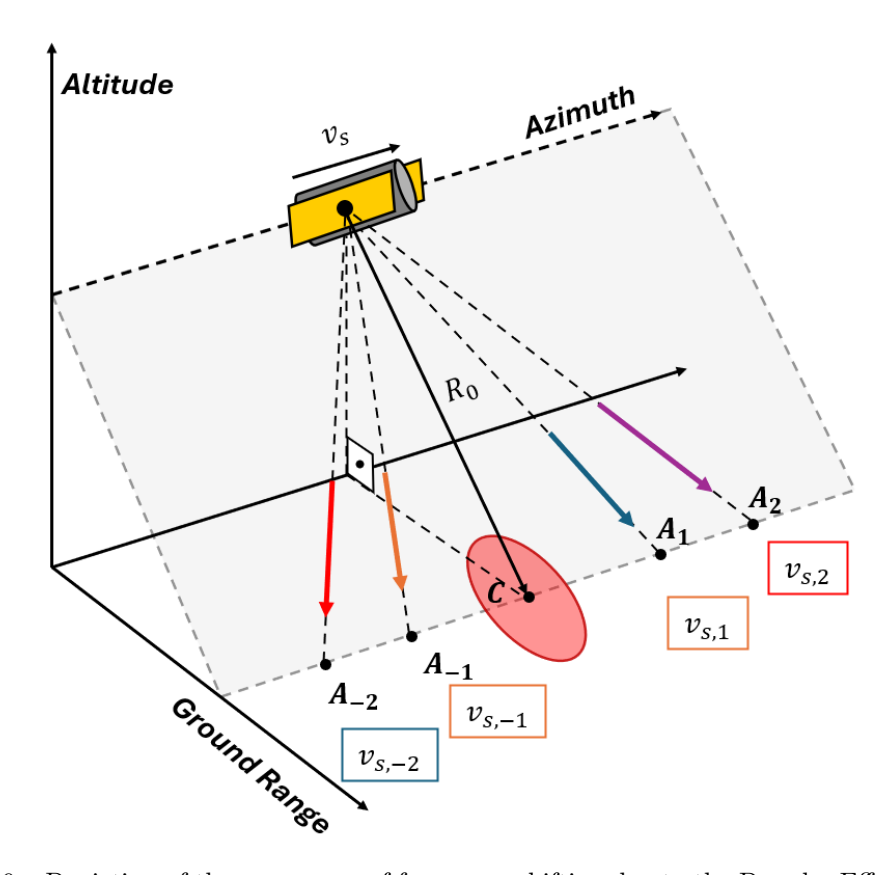


FIGURE 3.9 – Depiction of the emergence of frequency shifting due to the Doppler Effect. All points on the ground which are not coincident to C will experience a different signal frequency due to the movement of the platform. In particular, some specific points $(A := \{A_k\}, k \in \mathbb{Z}^* \text{ will experience a shifted frequency which, when processed back to the satellite, will be processed as the same frequency as the target's (center C). These points are call$ **Azimuth Ambiguities**.

However, there will be certain spots on the ground whose reflected Doppler frequency towards the satellite will follow the equation

$$f_k = f_0 + k \cdot PRF, \ k \in \mathbb{Z}$$
 (3.17)

Where PRF is the Pulse Repetition Frequency (PRF = $\frac{1}{PRI}$) of the signal.

At first glance, this property is of no concern to any acquisition project. Nonetheless, satellite systems which embed SAR instruments have to process the received data with some sort of processing frequency. Satellite systems process incoming signals in frequencies similar to the values of the PRF used to emit signals.

The most important parameter for signal processing in SAR is the *Oversampling Factor* B_z , defined by:

$$B_z = \frac{f_{\text{sampling}}}{\text{PRF}} \tag{3.18}$$

An increase in oversampling leads to a higher sampling frequency capability. It is common to sample signals in SAR systems with oversampling factors of 1, 1.2, 1.5, and at most 2. The higher the factor, then more data points will need to be stored in the embedded hardware - which is expensive, since SAR image acquisitions tend to necessitate hundreds or even thousands of megabytes of storage.

Still, having a limit to sampling frequency means that any frequency $f > B_z \cdot PRF$ will not be accurately mapped. Any frequency which follows the format below:

$$f = k \cdot B_z \cdot PRF + \Delta f, \ k \in \mathbb{Z}, \ 0 \le \Delta f < B_z$$

Will be perceived by the sampling hardware and, therefore, the image as its remainder. This frequency will be **ambiguous** to the frequency Δf .

$$f \longleftrightarrow \Delta f$$

If we take $B_z = 1$ for simplicity and $\Delta f = f_0$, we see that it falls under the case of 3.17.

Referring back to Fig. 3.9, it is much clearer how these specific spots may pose a problem to an acquisition: all points on the ground whose position is such that its Doppler frequency respects 3.17 will have its frequency recognized by the embedded hardware as the frequency f_0 of the center. In other words, signals of different frequencies will mesh with the scene's signal due to ambiguity in processing, leading to an infected image due to limitations in the frequency domain.

These are the **Azimuth Ambiguities** - **points whose frequency will be interpreted as the scene's due to an ambiguity in sampling and processing.** The signals carrying these ambiguous frequencies will therefore overlap with the scene's signal and therefore infect it.

Azimuth ambiguities can be minimized by an increase in sampling hardware, but as range ambiguities, they can never be fully eliminated, becoming a real constraint for SAR systems which must be analyzed beforehand.

Another way to reduce the number of Azimuth Ambiguities is to increase the pulse repetition frequency used by the embedded hardware, as higher PRF leads to less points on the ground that will match the frequency f_0 in a defined spectrum.

The main setback of increasing the PRF indefinitely is that its increase leads to also increasing the number of Range Ambiguities. Since $PRI = \frac{1}{PRF}$, higher PRF values lead to smaller PRI values, and therefore higher quantities of range ambiguities, as 3.15 shows.

3.3.4 Azimuth Ambiguity-to-Signal Ratio (AASR)

In the same fashion of RASR, we can propose a ratio between the received ambiguous power that comes from ambiguous frequency processing and the power reflected by the scanned scene. This is the so called Azimuth Ambiguity-to-Signal Ratio.

There is no fixed formulation of AASR, as the ambiguity in frequency depends of several factors - most importantly on the acquisition methods that will be detailed in the next section. But the main principle applies - a ratio between the power coming from ambiguities and the power of the target.

Both Range and Azimuth Ambiguities become the whole of ambiguity power in a SAR acquisition. Summing the total power captured in both methods results in the total ambiguity power that can interfere with the image.

Their effects on the acquired image depend on the mode of acquisition - that is, how the antenna focuses on the ground to capture the necessary signals.

Some different types of acquisitions will discussed next.

3.4 Acquisition Modes

The hardware of SAR itself does not differ much from a common SLAR set (aside especially from the frequency processing algorithm). Nonetheless, even with a fixed hardware there are numerous manners to exploit optimal performance of a specific parameter of choice, so long as the platform and the hardware itself is flexible enough to handle such strategies. These methods are the so called **acquisition modes**, where depending on the behavior programmed into the antenna, as well as the type of movement the platform executes, one can extract different image specifications and quality parameters.

The two most important and widely used types of acquisition modes are **Stripmap** and **Spotlight**.

3.4.1 Stripmap (SM)

The Stripmap acquisition mode (SM) is executed when the platform moves at a straight line, with constant speed, while the antenna is maintained at a fixed angle both in elevation (β_c) and azimuth $(\alpha_c$, called *squint* and usually $\alpha_c = 0$). No particular landmarks are constantly looked for, such that it illuminates a long strip as the platform moves.

Fig. 3.10 displays the acquisition mode of Stripmap.

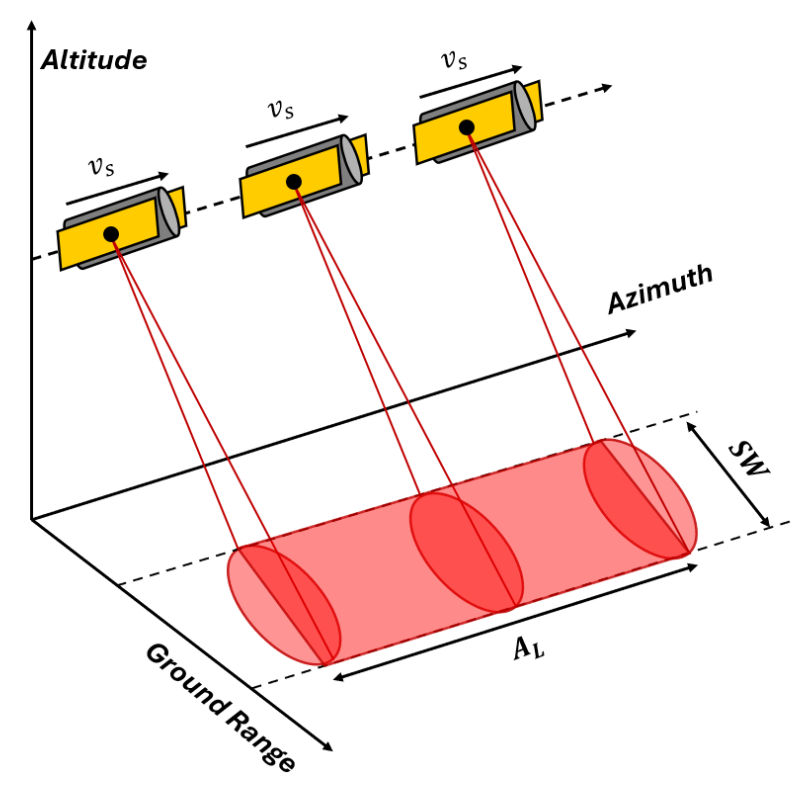


FIGURE 3.10 – Stripmap acquisition depiction - the antenna keeps steered at a particular solid angle, never changing its squint.

The azimuth length of the strip A_L is indefinite, while the swath width SW is limited by the time size of the signal in the echo window. In TerraSAR-X, the swath width of an SM acquisition is around 30 km.

A particular point P on the ground is illuminated by the beam for a duration of $T_{ill,SM}$. This time amounts from the interval between the initial instant where P enters the beam footprint and the final instant where it leaves the beam. Since the beam travels at the same velocity as the platform v_s , the illumination time of the Stripmap mode can be obtained as

$$T_{ill,SM} = \frac{x}{v_s} \approx \frac{R_0 \theta_a}{v_s} = \frac{R_0 \lambda}{v_s L_a} ,$$

$$\therefore \boxed{T_{ill,SM} = \frac{R_0 \lambda}{v_s L_a}} . \tag{3.19}$$

If we refer back to 3.13, applying 3.19 to it results in the final expression for the azimuth resolution of a SAR system in Stripmap mode as

$$\delta_{SM} = \frac{\lambda R_0}{2v_s} \cdot \frac{1}{\frac{R_0 \lambda}{v_s L_a}} ,$$

$$\therefore \delta_{SM} = \frac{L_a}{2} \ . \tag{3.20}$$

Eq. 3.20 is the most important result in all of SAR Theory. It states the core of all that is attractive under this technology for designers to exploit and engineers to implement, which could be summarized into three main points:

- 1. The azimuth resolution of a SAR system is completely independent of the distance between the radar and the target scene. So long as the transmitted pulse has enough power not to be confused with noise on its return, two points far off by at least this amount will be resolved, whether the platform is 10 km above the ground or 10.000 km.
- 2. The azimuth resolution is now tied directly to the antenna's length in azimuth and reducing its length improves resolution. It is an unintuitive statement, as one would expect the antenna to increase for this to occur. Designers avoid reducing too much the length of the antenna in the along-track line, however, as a short antenna leads to a broad main lobe on the power irradiation pattern, leading to much spurious power returning in the form of Range and Azimuth Ambiguities.

In the case of TerraSAR-X, with an azimuth antenna length of 4.8 meters, the azimuth resolution of a SM acquisition is around 2.5 meters.

The advantage of the Stripmap mode is the size of the acquired scene. With a wide swath of 30 km in TerraSAR-X, as well as an indefinite length in along-track, a sizeable coverage can be obtained with reasonable image quality - low amount of ambiguity power due to little to no antenna squint and decent resolution overall.

The disadvantage is not being able to harness ultra-high resolution that other modes are capable of, such as Circular SAR or Staring Spotlight, which will be the next topic.

3.4.2 Spotlight

While Stripmap maintains its antenna pointing to a fixed angle position, the Spotlight technique does the opposite. As one would expect, an imaging radar must image a specific region, therefore it is intuitive to argue the antenna should always point towards this particular landscape.

This is precisely what the Spotlight mode does - it steers the antenna so it always points to the same region, regardless of the movement of the platform. Fig. 3.11 illustrates the mode in action.

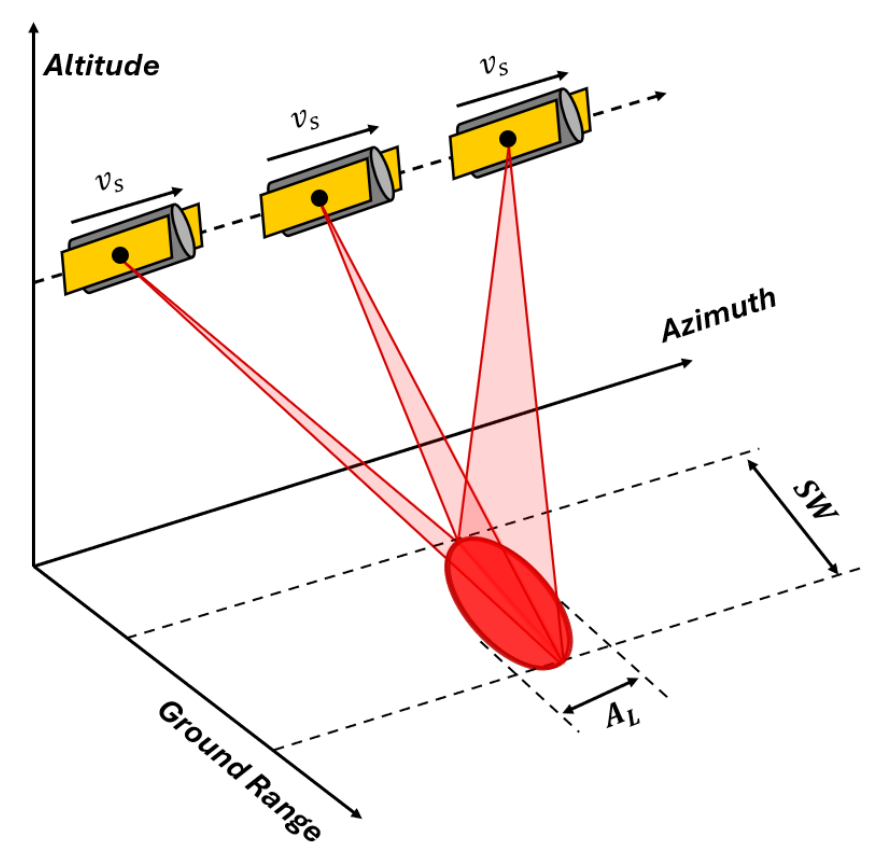


FIGURE 3.11 – Depiction of a Staring Spotlight acquisition, where the antenna keeps steering towards a particular landscape in spite of the movement of the platform.

This is a clever strategy, since maintaining the beam footprint always at the same location increases the illumination time of all points in the landscape of interest. Additionally, the illumination time of the points on the ground is virtually arbitrary, as it depends on how much time the antenna is steered towards the scene. Theoretically, if an antenna could handle such steering, the resolution in the azimuth direction could go as high as possible. It will be shown, still, why this is currently not possible.

One key note to be raised is that the Spotlight Mode can be subdivided into two different main groups: **Staring Spotlight (ST)** and **Sliding Spotlight (SL)**. The former has the antenna pointing towards a scene center located precisely on the ground, while the latter points towards a virtual rotation center *beneath* the surface.

From this point onward, this thesis will solely focus on Staring Spotlight when Spotlight mode is concerned.

When it comes to ST, the illumination time of the scene is given by the interval of time between the initial instant where the antenna starts pointing towards the scene, and the final one where it stops such steering. Fig. 3.12 displays the geometry of such scenario.

The azimuth antenna angle at which the radar starts emitting pulses towards the

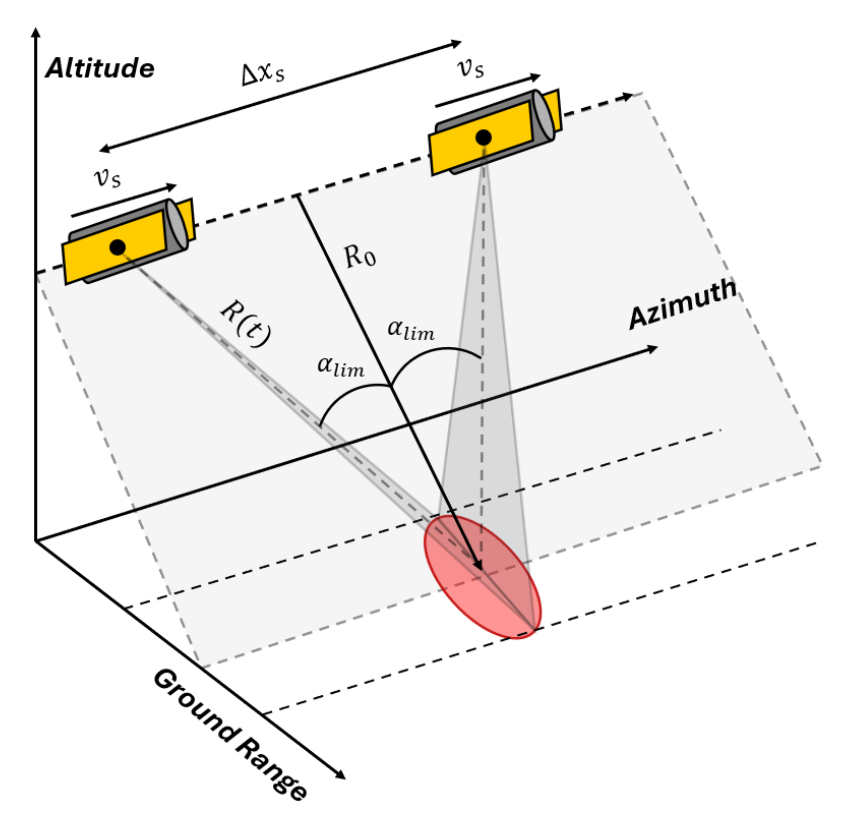


FIGURE 3.12 – Geometry of a Staring Spotlight acquisition, in function of the steering limit angles.

ground is α_{lim} , and it is determined by restrictions that are intrinsic of the design. For TerraSAR-X, which implements Array Antenna technology with 12 irradiators spread over 4.8 meters, the conventional limit for the azimuth antenna angle to start steering is 2.2°. Any further from this threshold leads to an irradiation pattern where *Grating Lobes* emanate more power than Main Lobes, directing power to non-intentional spots on the ground and leading to high ambiguity power interfering with the scanned scene signal⁵.

This is precisely the reason why it is not possible to illuminate indefinitely a region and therefore acquire it with outstanding resolution - a Grating Lobe would form, leading to spurious power mapping other regions of the surface that would overlap with our intended scene. Even if this were addressed, there would be other limitations, such as SNR levels plummeting when the platform is too far away, or the curvature of Earth itself would restrict the maximum azimuth angle limit.

Setting the limit of α_{lim} , Fig. 3.12 shows that the scene is illuminated until the platform finishes its traversal of Δx_s .

According to the geometry of the schematic, we can say:

$$\Delta x_s = 2R_0 \tan \alpha_{lim} = v_s T_{ill,ST}$$

⁵The limits of Spotlight were defined for TerraSAR-X in (J. Mittermayer S. Wollstadt; Scheiber, 2014).

This leads to the illumination time of the Staring Spotlight mode.

$$T_{ill,ST} = \frac{2R_0 \tan \alpha_{lim}}{v_s} \tag{3.21}$$

In expression 3.13, we obtain the resolution of the Spotlight mode.

$$\delta_{ST} = \frac{\lambda_0 R_0}{2v_s} \cdot \frac{1}{\frac{2R_0 \tan \alpha_{lim}}{v_s}} ,$$

$$\therefore \delta_{ST} = \frac{\lambda}{4 \cdot \tan \alpha_{lim}} \,. \tag{3.22}$$

It is notable, once again, how the resolution in azimuth is independent from the distance between the platform and the ground - so long as the satellite traverses more to complete the arc of $2 \cdot \alpha_{lim}^{6}$.

With TerraSAR-X (TSX) specifications, operating in X-Band with a wavelength of 0.03 m and $\alpha_{lim}=2.2$, the azimuth resolution with the use of Spotlight acquisition is $\delta_{ST,TSX}\approx 19.5$ cm.

When comparing it with the SM resolution:

$$\delta_{SM}/\delta_{ST} \approx \frac{2.5}{0.2} = 12.5 ,$$

$$\therefore \delta_{ST} = \frac{\delta_{SM}}{12.5} \ .$$

Spotlight is capable of extracting 12.5 times better resolution than Stripmap, which is a considerable improvement in quality.

While impressive, the best theoretical resolution for TerraSAR-X is still far lower - around $\delta_{CSAR} \approx 0.75$ cm

The main disadvantage of Staring Spotlight is the size of the image. The azimuth length of the acquisition is always limited to the beam footprint in the along-track direction, which is roughly determined by:

$$A_L \approx R_0 \theta_a \approx R_0 \frac{\lambda}{L_a} \ .$$

For TerraSAR-X, this amounts to $A_L = 3.6$ km at most. However, the full performance

⁶The formulation of 3.22 is an approximation to the simplified geometric scenario elaborated in this thesis, and does not constitute the closed formula. It is only valid for small scenes and small α_{lim} angles.

image usually does not utilize the whole extension of the beam footprint, commonly being restricted to 2.5 - 3.0 km.

A final downside of the Staring Spotlight is the fact that it is rarely useful to acquire an ST image that is not a square. Since the swath width is far longer than the azimuth length, this creates a square image that is limited to the shorter edge.

For comparison, a Stripmap acquisition done using TerraSAR-X can encompass areas of 400 to 900 km^2 . Staring Spotlight, on the other hand, works with areas of 6.25 - 9.0 km^2 at most.

This area extension is extremely limited for ultra-high resolution imagery in wide coverage. If TerraSAR-X wanted to map a landscape previously scanned using SM mode, but now utilizing ST mode, it could take as long as 216 hours (or 9 days) to do what Stripmap could achieve in some minutes, due to the orbit round trips.

If we are able to enlarge the azimuth length - suppose we double it - not only would the area increase proportionally by maintaining a fixed length on swath width, but we could even increase it to match the extended azimuth length. We could increase the area of the acquisition 2-4 times just by finding a reliable method to double the azimuth length, increasing a typical ST coverage to 12.5 - 25 km², not just 6.25 km².

This extremely limited coverage of conventional Spotlight modes in general could be tackled, using new emergent techniques to solve this conundrum of area \times resolution and extend the size of the Staring Spotlight acquisition.

In the next chapter, the Extended Staring Spotlight will be proposed.

For a deeper dive in Synthetic Aperture Radar, we suggest the reading of (Curlander; McDonough, 1991).

4 Extended Staring Spotlight

The goal of this Bachelor Thesis is to provide a method of acquiring a larger area of acquisition while not sacrificing resolution in the process. As previously explained, increasing the illumination of a region amounts to maintaining it in the beam footprint for longer intervals.

For a SAR embedded system whose trajectory is linear (or in orbit) the best resolution achievable is obtained in the Staring Spotlight mode (ST), introduced in 3.4.2.

The first approach to extending the ST azimuth length (and therefore doubling the covered area) would be to execute two consecutive Staring Spotlight acquisitions, one right after the other, in such a way that the second acquisition has a ground image that is juxtaposed, in azimuth, to the first one. This way, both frames, when combined, would generate an extended image. However, as we'll show in the next section, this is not possible.

The following sections will detail the current problems with traditional imaging, how can we overcome them, and the final product of the Extended Staring Spotlight.

4.1 Discontinuity in Traditional ST

Let's analyze the possibility of acquiring two consecutive Staring Spotlight images, with the effort of producing an ST image twice the size of a normal one.

As explained in 3.4.2, the resolution in along-track is dependent on α_{lim} , the steering limit for the antenna to turn. This limit varies from system to system, but in the case of TerraSAR-X, it is $\alpha_{lim} = 2.2^{\circ}$. Any further from this would degrade the image far too much, as spurious power from ambiguous sources would interfere with the received main signal - as explained in 2.5, this is due to the existence of Grating Lobes, which at this angle will harness as much power as the Main Lobe.

So in order to maintain the resolution of Staring Spotlight, the radar must traverse the whole course, from $\alpha_{lim} = 2.2^{\circ}$ to $-\alpha_{lim} = -2.2^{\circ}$. Any less from this will degrade resolution, as it will reduce illumination time of the points acquired, and any more will

infect the image with spurious power.

Fig. 4.1 depicts the necessary procedure to acquire two consecutive ST images.

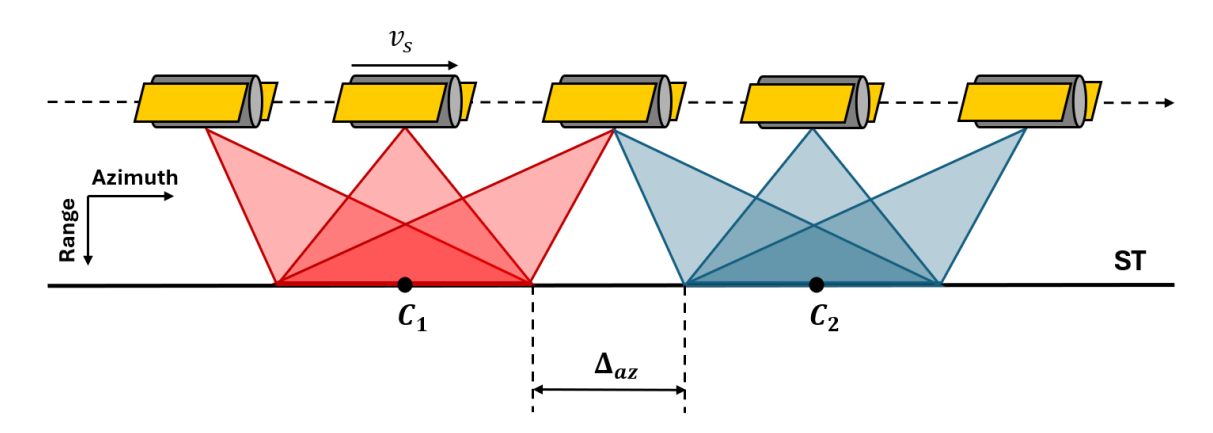


FIGURE 4.1 – When acquiring two consecutive ST images, the satellite needs to steer completely within its steering angle range, and only when it is finished doing so, it can point frontward to the next scene, with the same starting angle as the first scene. This inevitably leaves a gap Δ_{az} between both scenes.

As shown, the consecutive ST acquisitions will leave a gap Δ_{az} between them.

This gap is obtainable by the geometry of the azimuth-range plane:

$$\Delta_{az} \approx 2R_0(\alpha_{lim} - \frac{\theta_a}{2}) \ .$$

The sine qua non condition to nullify the gap is given by 4.1.

$$\alpha_{lim} = \frac{\theta_a}{2} \ . \tag{4.1}$$

This creates a scenario where, in order to generate a continuous strip where two (or more) images can be consecutively received, the total steering angle range would go, in the scenario of TerraSAR-X, from 4.4° to 0.3°. This scenario is shown if Fig 4.2.

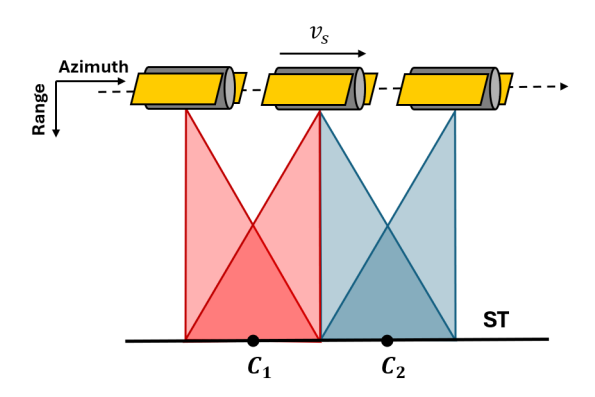


FIGURE 4.2 – Possible consecutive acquisition of two ST images. The satellites now travel a narrow path during the illumination of a specific scene before imaging the next one, which heavily impacts resolution.

This significantly reduces azimuth resolution - in fact, since the points on the scene would be illuminated in a duration of a half power beam width angle, it would resolve the same as a conventional Stripmap mode.

This concept on itself is not without merit, and it is explored to produce a different type of concurrent acquisition mode - the **Continuous Staring Spotlight (CST)**¹.

The current developments show that traditional imaging techniques cannot solve the area-resolution conundrum in this case, meaning it is necessary to bring more powerful tools to the table.

4.2 Concurrent Imaging

In 2014, it was initially proposed a new imaging method called **Discrete Stepped Strip** (**DI2S**) in (Calabrese, 2014). This technique breaks the conventional imaging method of acquiring images by altering the direction of emitted pulses mid-execution, alternating between one direction and another. This method would eventually be called **Concurrent Imaging**.

4.2.1 Core Concepts

Concurrent Imaging changes the proper functioning of the typical trains of transmission pulses sent to the ground. Consider Fig. 4.3. The imaging done of the scene is constructed by sending multiple pulses to the ground, in such a way that these pulses must all match their intended design schedule. In the case of SM, all pulses must be sent as the antenna keeps a fixed angular position. In ST, all pulses are sent so that the antenna keeps itself pointed towards a particular spot on the ground (scene center). Until the intended acquisition is completely finished, the pulse emission routine does not change.

¹L. F. S. R. Soares, J. P. T. Ribeiro, T. Kraus and M. Bachmann, "An Extended Staring Spotlight Mode Enabled by Concurrent Imaging," 2025 IEEE Radar Conference (RadarConf25), Krakow, Poland, 2025, pp. 508-513

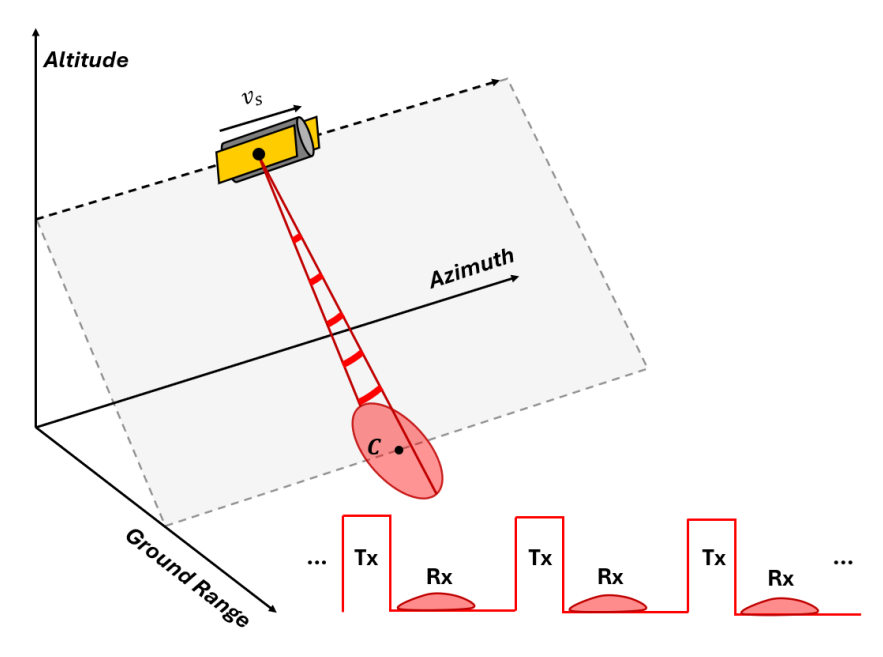


FIGURE 4.3 – Usual acquisition of a desired scene. All pulses emitted are following the schedule of one, and one one, acquisition mode. In the case of Stripmap, all pulses are emitted at a fixed antenna angle, while for Spotlight all pulses are emitted focusing on one, and only one, scene center.

However, the use of Concurrent Imaging challenges this idea. Let's imagine the situation now displayed in Fig. 4.4. The moving satellite desires to map two different spots, both of them being available in the current trajectory. If it utilizes a fixed set of train pulses, as did the satellite in Fig. 4.3, it will only be able to acquire one scene, and then it will have to come back to map the remaining one. But if it alternates the emission of pulses - sending one pulse towards Scene 1, then the next towards Scene 2, and so on - it will be able to map both scenes during the same flight window.

Essentially, what we'd have would be:

- If the pulse emitted is of **Odd** order $(1, 3, ..., 2n 1; n \in \mathbb{Z}^*)$, it is executing an **SM** acquisition on Scene 1.
- If the pulse emitted is of **Even** order $(2, 4, ..., 2n; n \in \mathbb{Z}^*)$, it is executing an **SM** acquisition on Scene 2.

So long as the signals arrive at convenient instants (which can be calculated previously), the concurrent acquisition is possible.

The rapid alternation between two or more beam directions is made possible due to the usage of electronic antenna systems such as the **Planar Antenna Array**, discussed in 2.3. The ability of switching directions thousands of time per second is possible by altering the phase step $(\Delta \phi_0)$ of the input current on each irradiator of the array. This leads to a shift in the phase (ϕ_k) , altering the value of the antenna composite angle psi, leading to a different gain diagram, whose main lobe will focus on a different direction $(G(\alpha, \beta))$. In other words:

$$\Delta \phi_0^{[1]} \longrightarrow \phi_k^{[1]} \longrightarrow \Psi_1 \longrightarrow G_1(\alpha, \beta) ,$$

$$\Delta \phi_0^{[2]} \longrightarrow \phi_k^{[2]} \longrightarrow \Psi_2 \longrightarrow G_2(\alpha, \beta)$$
.

A fast switch would not be possible if the embedded SAR antenna was an electromechanical system, as the quick rotations could either break the pivots, heat the friction zones and damage the equipment, or simply not be sufficiently fast enough.

This is a game changer in SAR technology, as it allows a SAR system to acquire different areas of interest on Earth's surface without the need of a second or third trip.

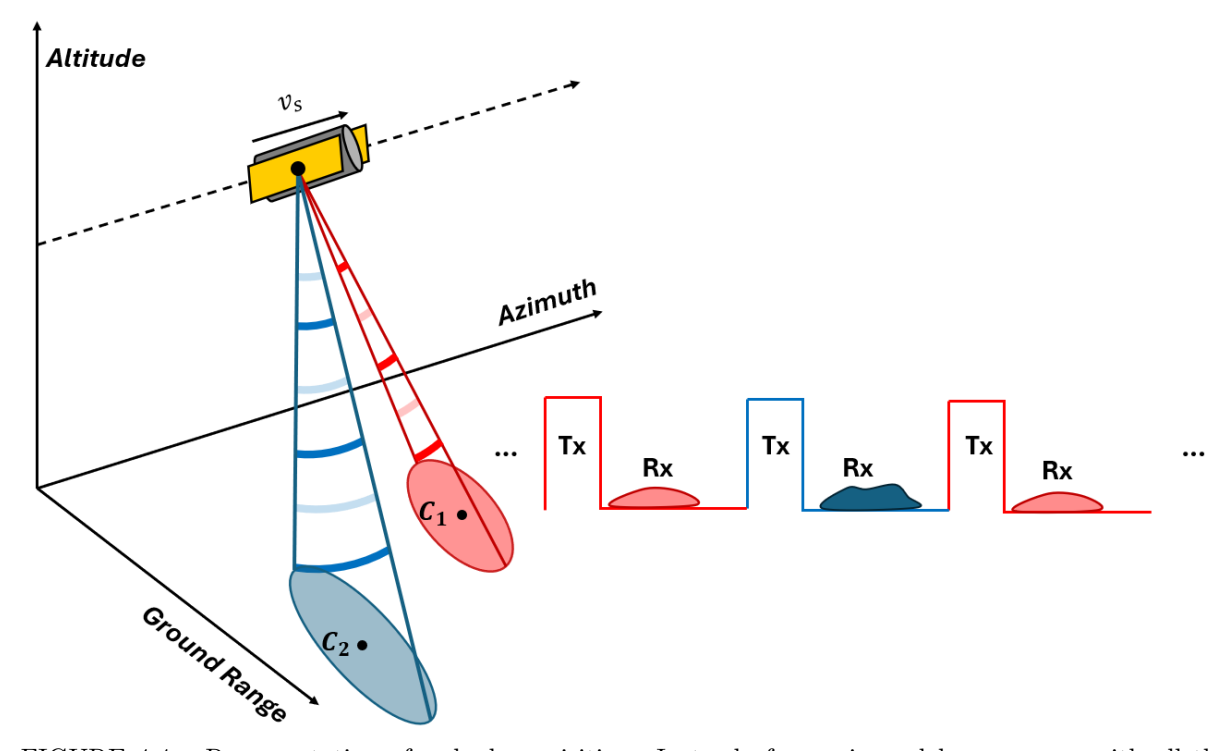


FIGURE 4.4 – Representation of a dual acquisition. Instead of mapping solely one scene with all the available pulses, the hardware sends interleaved pulses - one towards C_1 and one towards C_2 - being then doable to acquire two scenes at the same time.

Another important point to stress about Concurrent Imaging is how it isolates the modes among themselves. While there will be side effects one must take into account when designing a concurrent acquisition², each $\mathbf{R}\mathbf{x}$ pulse acquired from a specific mode is concerned solely with the acquisition parameters of itself - the acquisition strategy used,

²The main problem to be addressed is the emergence of **Odd Ambiguities** - spurious power which is an ambiguity of another scene, not the focused one at the scanning instant. This emerges from the existence of two different Tx pulses within the same PRI, each imaging a different region on the ground. There will be ambiguous regions on Earth's surface whose timing of Mode 2 will interfere the the scene acquired by Mode 1, and vice-versa.

the interval between two $\mathbf{T}\mathbf{x}$ pulses solely of the scene in this mode, its echo window interval etc.

It is also possible, in theory, to leverage multiple modes in tandem, not just two. The general rule for acquiring N scenes within the same path is given by the following implication.

$$k_{th} \text{ pulse} \iff ((k-1) \mod N + 1)_{th} \text{ scene, } k \in \mathbb{N}^*$$
 (4.2)

However, in literature there has only been usage and extensive research on Concurrent Imaging done with two modes in tandem, as managing three or more concurrent acquisition modes becomes far more complex than just two.

4.2.2 Limitations on Concurrent Imaging

While a powerful tool, Concurrent Imaging has some trade-offs to it that must be analyzed before jumping to it as a solution to parallelize acquisitions.

1. If a designer wishes to acquire N different scenes concurrently, all with the same **Pulse Repetition Frequency (PRF)**, **it will be necessary to increase the number of pulses emitted** N **times** (hence, increase the total PRF N times as well) - if not done so, each mode will be scanned with $\frac{1}{N}$ times the repetition frequency expected. For example, if a designer wishes to scan two regions on the ground, both at PRF = 5000 Hz, the embedded radar system will need to generate a composite PRF (total number of pulses per second, regardless of the scene the pulse is imaging) of PRF = 10000 Hz.

This comes with its list of hurdles that may need to be overcome.

- This may be struggling to deliver for some systems. TerraSAR-X, for example, has its frequency oscillator limited at *circa* 7 kHz for acquisition purposes. Hence, if a designer wishes to image two landscapes concurrently, each can be framed with an individual PRF of at most 3.5 kHz.
- Another important issue relates to the **Echo Window** in the transmission time frame. As PRF increases, so does the number of transmission pulses that populate a given interval. **This leads to the reduction of the echo window of a given mode, which by itself reduces the maximum swath width** of the acquired scene. Concurrently acquiring two landscapes doubles the PRF, which itself halves the available echo window for each scene and, therefore, its maximum swath width achievable.

- 2. While theoretically possible, it is not practical to leverage more than two modes (scenes) in Concurrent Imaging, unless in extremely niche and simple use cases.
- 3. Concurrent Imaging is not capable of imaging any two scenes both their Rx signals need to arrive at the proper instants, following mainly three conditions:
 - (a) The received signals mustn't interfere with transmission pulses (**Tx Interference**).
 - (b) The received signals mustn't interfere with any Nadir signals³ (**Nadir Interference**).
 - (c) The received signals should not interfere with each other. This is a general condition, as in the case of only two concurrent modes there are some techniques which do allow signal interference, such as sending *up-down* Chirp pulses and de-correlate them when received however, we will not consider this in our work (M. Villano; Moreira, 2018).
- 4. As will be later shown, scanning two scenes at the same time will heavily the quality of the acquired images due to ambiguity power, which increases considerably.

All of these conditions must be taken into account when designing a concurrent acquisition, and the design must be carefully done beforehand to see whether it is feasible or not.

Each specific case must be analyzed with care, as different scenarios lead to multiple variants.

With Concurrent Imaging explained, we will talk about utilizing it to extend the conventional Staring Spotlight mode.

4.3 Extending the Staring Spotlight

It was seen in 4.1 how it is physically impossible to use continuously the same antenna beam to scan two azimuth-juxtaposed scenes in Staring Spotlight. In 4.2, it was discussed how we are able to leverage Concurrent Imaging and its ability to change the direction of the pulse mid-flight. We are now in conditions of solving the discontinuity problem of Staring Spotlight with the use of Concurrent Imaging as a support technique.

³Nadir signals are spurious and time-narrow pulses which come from the reflection of transmission pulses on the ground right at the Nadir line. Even if the antenna gain in the Nadir direction is low, the incidence angle is small enough that almost all power reflects towards the satellite, becoming too strong to be negligible.

4.3.1 The Extension Method

If we wish to enlarge the total covered area in the azimuth direction, instead of consecutively acquiring a first then a juxtaposed second scene, we acquire concurrently two scenes that are juxtaposed in azimuth and have the same elevation angle, as Fig. 4.5 depicts.

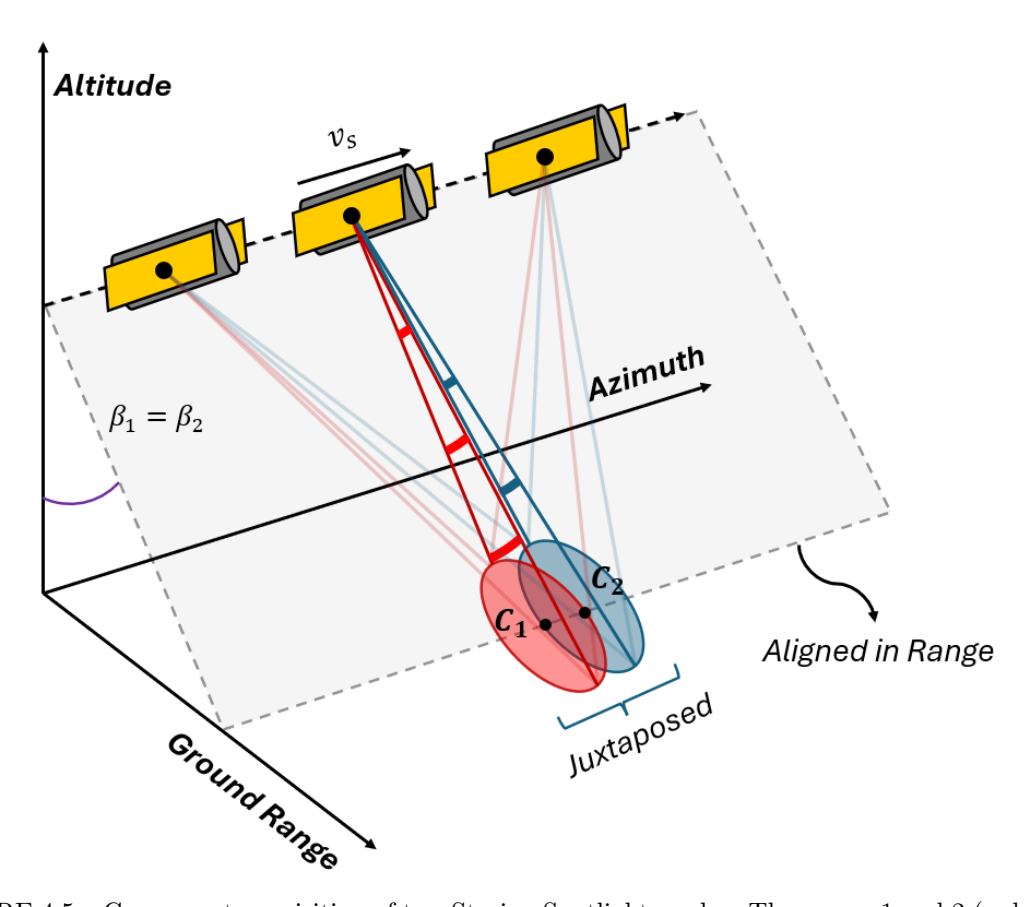


FIGURE 4.5 – Concurrent acquisition of two Staring Spotlight modes. The scenes 1 and 2 (red and blue) are juxtaposed azimuth-wise, but maintaining the same elevation angle. Note how scene 1 and scene 2 receive pulses in an interleaved manner. The beams from earlier and later positions of the platform were drawn less vibrantly to avoid pollution.

However, blindly imaging two jointed scenes is careless. As a satellite moves by to initiate its concurrent imaging process, it will only start to acquire any of the images if it has an angle within ST imaging range. In other words, if $\alpha(t) = \alpha_{lim}$, then the focused scene will start receiving pulses. There are two scenes that need to be acquired in ST. If the satellite, at the very moment it forms an azimuth angle of $\alpha_1(t) = \alpha_{lim}$ with the first scene center, starts imaging both scenes concurrently, this will present a problem -acquiring both simultaneously at this instant will force the azimuth angle with the second scene center - $\alpha_2(t)$ - to be greater than $\alpha_1(t)$. This leads to $\alpha_2(t) > \alpha_{lim}$ during an interval of the flight at entrance. Conversely, at the exit of the acquisition, the value of $\alpha_1(t)$ will be bigger than the limit for another interval, until $\alpha_2(t) = \alpha_{lim}$.

This is a serious issue - for some considerable portion of the concurrent ST imaging, both images will be infected with considerable ambiguity power, as the antenna will be out of their intended steering angle ranges. Grating Lobes with higher power gain than Main Lobes will redirect emitted power to unintended regions of the surface, such that these regions will overlap with the intended signals.

One remedy of this would be doing the opposite - only starting the concurrent ST acquisition if the inner-most scene has its center at an azimuth angle of α_{lim} . In other words, starting the movement at entrance when $\alpha_2(t) = \alpha_{lim}$ and finishing the scan when $\alpha_1(t) = \alpha_{lim}$.

While partially the answer, this on itself would also not be optimal. At entrance, Mode 1 would need to start at a lower azimuth angle than the steering limit of conventional ST, and so would Mode 2 at exit. As stated in 3.21, the illumination time of all points on the scene is strictly dependent on the azimuth angle of start and finish, and 3.22 shows how resolution worsens as illumination time decreases.

The correct approach on how to extend ST acquisitions in a concurrent manner is:

- 1. At entrance, Mode 1 activates at $\alpha_1(t) = \alpha_{lim}$, but Mode 2 remains turned off. In this phase, only scene 1 is being ST imaged.
- 2. When $\alpha_2(t) = \alpha_{lim}$, turn on Mode 2. Both scenes are being ST acquired via Concurrent Imaging.
- 3. At exit, at some point $\alpha_1(t) = -\alpha_{lim}$, even though $\alpha_2(t)$ is still within azimuth angle steering range. At this instant, turn off Mode 1, but keep Mode 2 running. At this phase, only Mode 2 is kept up, only scene 2 is ST acquired.
- 4. At last, when $\alpha_2(t) = -\alpha_{lim}$, turn off Mode 2.

In a more concise reasoning, at the beginning and at the ending of the ST imaging, the radar should perform a conventional Staring Spotlight for scene 1 and scene 2, respectively. Otherwise, both are being concurrently acquired. Fig. 1.3 displays the steps previously written.

With these guidelines, we can say we extended the ST without leaving any gaps. Henceforth, it is an Extended Staring Spotlight (EST).

4.3.2 Technical Analysis

The next steps after defining a reliable procedure to enable the EST mode revolve around studying the consequences and trade-offs of it.

There are three main consequences of utilizing **EST** for an enhanced imaging of the ground landscape.

- 1. With the increase in acquiring modes, as previously established in 4.2, the available interval in each echo window to accommodate received signals is reduced by half. This could be a problem for other acquisitions, but in the particular case of Staring Spotlight acquisitions, this does not pose a problem. With TerraSAR-X as reference, the available echo window of a traditional acquisition can accommodate scenes with swath widths up to 30 km. Halving it by doubling the PRF would still leave 15 km of maximum swath width available for any acquisition. For the same satellite, ST imaging may use swath widths as up to 7.6 km (although, as said earlier, it usually enforces 2.5-3.0 km so acquire a square-shaped image). Overall, the size of the extended image in the range direction would not be reduced. Hence, doubling the amount of scenes and the azimuth length of the total acquisition does double the total acquired area.
- 2. The amount of Range Ambiguities increases dramatically. This is the main quality trade-off when switching from conventional ST to EST while the azimuth resolution is maintained and the size is doubled, the ambiguity power on the scene can increase to the point of the image being completely unusable.
- 3. The availability of EST acquisitions with a bare minimum quality is not guaranteed for all antenna directions. It depends on the size of the desired image, at which incidence angle θ_i is the landscape located, and the quality threshold desired by the designer that is, how much ambiguous power overlapping with the intended image is considered acceptable.
 - Much more importantly, the timing analysis checking whether the received signals fit within their respective echo windows is much tighter than conventional imaging methods, forcing us to adopt a thorough investigation to find parameters for achievable acquisitions.
- 4. The division of one composite pulse into two pulses presents a design cross-roads: should the designer utilize two transmission pulses, each with the same duty cycle (τ_p) as if each were acquired with a single pulse? Or should one pulse be time-divided into two, giving more space to echo windows at the cost of total energy emitted, thus reducing the total SNR of both pictures?

All the items in the technical analysis lead us to propose a general methodology on how to generate a valid EST acquisition.

The step-by-step methodology is proposed in the next section.

4.4 Methodology

There are five main steps which need to be performed in order to obtain an EST product:

- 1. **Timing Analysis** at which PRFs and pulse formats the intended scene can be acquired from a timing perspective;
- 2. Range Ambiguity assessment the amount of ambiguity power coming from regions on the ground whose reflected signals have their return coincident with the returning signals of the focused scene.
- 3. **Azimuth Ambiguity assessment** the amount of ambiguity power coming from spots on the ground whose frequency is equal, in module, to the frequency of the main scene.
- 4. **Ambiguity Signal Ratio threshold** given a threshold of acceptable levels of ambiguity power onto the scene, filter all the PRFs which do not achieve an spurious ambiguity power below this threshold.
- 5. Take the PRF whose ambiguous power is the smallest of all collected, extracting therefore the parameters which provide the best EST image of all under its geometrical restrictions.

The goal of these steps is to verify the feasibility of the Extended Staring Spotlight, and under which conditions it is doable. For all possible incidence angles which fit the range of a given satellite (in the case of TerraSAR-X, the full-performance angle range would be $20^{\circ} \leq \theta_i \leq 45^{\circ}$), we verify whether there is a valid PRF which provides an acquired image with no interferences and acceptable ambiguous power levels. If it is, then we consider to be possible an EST acquisition for that particular incidence angle.

We'll discuss the implementation of each step of the general methodology, first introducing the techniques for conventional acquisitions and then adapting them to the scenario of Concurrent Imaging, and especially to the EST mode.

4.5 Timing Analysis

A typical timing analysis in conventional SAR imaging involves studying the return signal and its time width in the echo window, asserting the Rx signal respects two main goals:

- 1. No **Tx Interference** the received signal must not overlap with a transmission pulse; and
- 2. No Nadir Interference the Nadir signal and the received signals must not overlap.

4.5.1 Conventional Timing Analysis

Nadir signals are the result of the reflection of the emitted pulses onto the ground at the foot of the Nadir line. Fig. 4.6 illustrates their origin. They need to be accounted for - in spite of the low gain attributed to a signal sent in a direction so far-off the main lobe, it is still relevant. The reason behind this comes from the fact that, since the emitted wavefront will be reflected at very low incidence angles ($\theta_i \approx 0^{\circ} - 3^{\circ}$), almost all of the emitted power reflects back to the radar, even if the gain attributed to it is low. Nadir interference occurs whenever a Rx signal has its power overlapping with the received power of a Nadir beam. In order for an echo window to accommodate a Rx signal without Nadir interference, it must not overlap with Nadir.

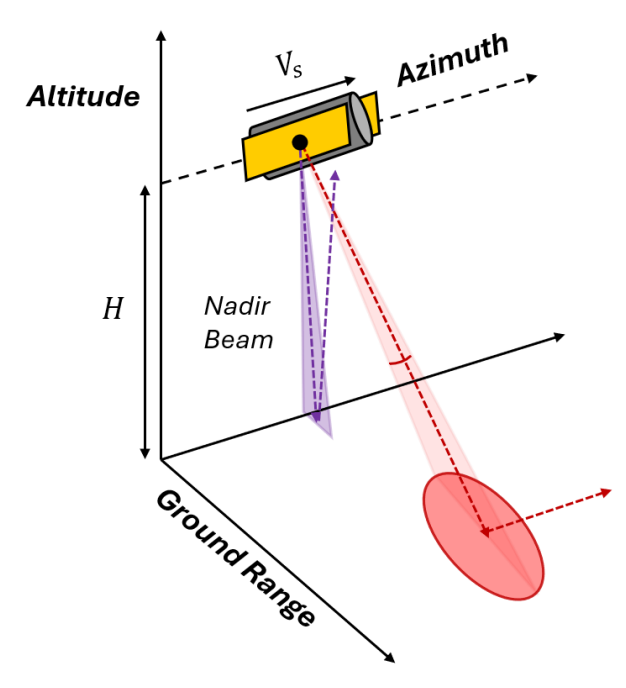


FIGURE 4.6 – Image depicting the emergence of Nadir beams. Since pulses propagate in spherical wavefronts, they will hit the ground in all available positions, regardless of gain. In the case of Nadir beams, they are the first to return to the system, but since their incidence angle is so low, most of the energy emitted is transmitted back with the Rx pulse, in spite of the low gain associated with it.

In summary, an achievable acquisition is that which satisfies both of these conditions: no Tx or Nadir overlapping with the Rx pulse. An example of a valid timing schematic can be seen in Fig. 4.7, where the received pulse has no intersection with either the

transmission pulse (hence, free of any kind of transmission interference) or the Nadir signal (hence, no Nadir interference).

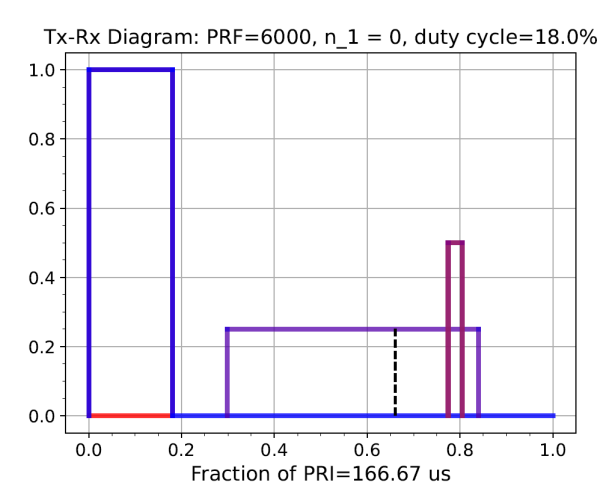


FIGURE 4.7 – Diagram of a transmission pulse schedule and its echo window. The blue rectangle corresponds to the transmitted pulse, with a duty cycle of 18% and PRF=6000 Hz, the large indigo rectangle accounts for the received signal from a scene on the ground, and the narrow purple rectangle is the Nadir received pulse. The Rx pulse doesn't overlap with the transmission pulse, and Nadir does not overlap with the Rx pulse as well, aside from the tail-end τ_p (dashed line), which is dismissed in pulse compression.

Of course, in order to prepare an acquisition, a designer needs to be aware beforehand which parameters are capable of obtaining the desired landscape. In a conventional acquisition setting, a Timing Diagram is constructed.

The Timing Diagram is a map which meshes two different plots: the first is the *locus* of all PRF values which cannot acquire a particular scene due to transmission interference, and the second *locus* is the set of PRF values which are unfit for acquiring a scene due to Nadir interference, and these *loci* are evaluated for all incidence angles.

Fig. 4.8 displays a simulated Timing Diagram for a system such as TerraSAR-X, at 519 km from the surface of the Earth, imaging a region close to a mountainous region such as Mount Everest.

If a designer wishes to acquire, for example, a scene at $\theta_i = 40^{\circ}$ and PRF = 5000 Hz, the diagram must be checked at those coordinates. In this case, neither the red line (Nadir Interference) nor the green line (Tx Interference) intercept the point, so no case of interference happens - it is a valid (θ_i , PRF) pair for acquisition.

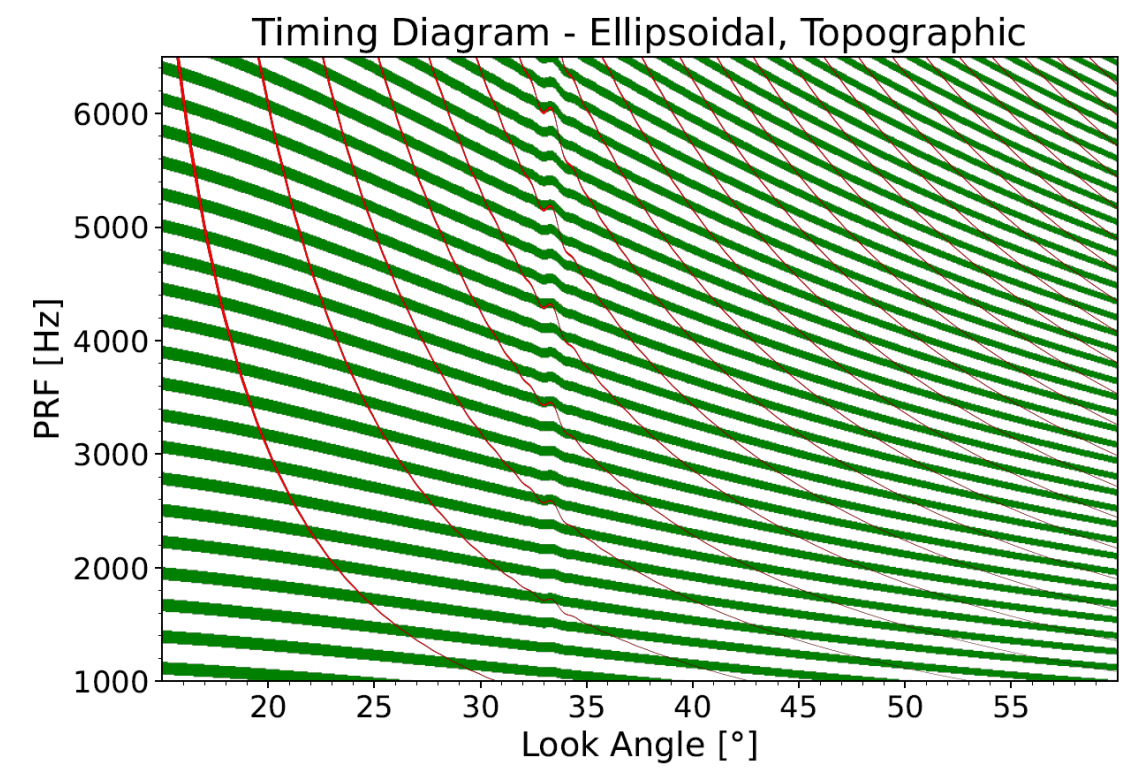


FIGURE 4.8 – Timing Diagram of availability of scene acquisition for a given pair of (θ_i , PRF), stretching from 15° to 60° of incidence angle and 1000 Hz to 6500 Hz of PRF. The red lines represent the pairs where there will be Nadir interference, while the green lines do the same but for the Tx Interference. Any blank space is a valid zone to start a conventional imaging technique, from a timing perspective alone. Notice the distortion around 34° - this is the region of higher terrain on the ground, such as Mount Everest. This simulation is a proof of concept only, as conventional mountains would not distort the diagram this much. We use a proof-of-concept topographic model of Earth, where terrain variations such as mountains are present, with an ellipsoidal approximation of the WGS84 computational model of the planet.

Timing Diagrams, for conventional imaging, are useful tools to verify the feasibility of an acquisition for the whole span of incidence angles. They embed within them both interference sources and give to the designer a clear view of the routes to be taken to obtain a scan of the Earth's surface.

In the case of Concurrent Imaging, and more specifically our Extended Staring Spotlight, we need to be more careful, as now there are twice as much transmitted pulses and Nadir callbacks we need to address.

4.5.2 Concurrent Timing Analysis

When addressing availability in Concurrent Imaging, one must understand it is not solely a matter of doubling the amount of transmission interference and Nadir interference *loci* in a conventional Timing Diagram. There are mainly two new challenges to overcome when acquiring scenery concurrently - Scene Overlap and Cross-Nadir interference.

Scene overlapping is the phenomenon where the received signals from different modes

- \mathbf{Rx} 1 and \mathbf{Rx} 2, in our case - mix themselves in the echo window. If the same rules of conventional imaging were to be applied, we could have two \mathbf{Rx} signals interfering with one another whilst not being subject to \mathbf{Tx} or Nadir interferences, hence this acquisition would be considered acceptable, which is not the case.

Similarly, **Cross-Nadir interference** is the process of having a Nadir signal from one mode interfering with the **Rx** signal of another mode.

Both scene overlapping and cross-Nadir interference can be solved if leveraging **Chirp Decoupling**⁴, although it will only solve scene overlapping and cross-nadir interferences in Concurrent Imaging acquisitions of at most **two** operating modes. We ignore this possibility in this thesis.

Henceforth, we need to make sure the two **Rx** pulses do not overlap neither themselves or repeat the previous interferences. Fig. 4.9 shows an example of an acceptable EST acquisition, where there are two ST images azimuth-wise juxtaposed, each acquired by its respective mode.

In Fig. 4.9, notice how each transmission pulse of each respective mode yields only 9% of duty cycle for their transmission pulses (**Tx 1** and **Tx 2**), instead of the expected standard of 18% duty cycle for a conventional acquisition. This was done to provide more space within echo windows and therefore allow more regions to be mapped on Earth's surface.

Recalling 2.24, halving the transmission pulse duty cycle comes at the cost of halving the SNR of the target image, since only half of the usual energy is being emitted to a particular mode than usual. We chose to do so since SNR levels are far easier to address if too low, not being considered necessary to analyze in the methodology of this thesis.

⁴Chirp Decoupling is a powerful technique which decorrelates received signals by mixing them with an Up or Down Chirp. If the received signal comes from a transmission pulse whose signal uses an up chirp, it can be passed through an Up-Chirp filter and be reconstructed, while neglecting an overlapping signal emitted with a Down Chirp pulse, and vice-versa. Due to time constraints, we did not leverage Chirp Decoupling in the thesis.

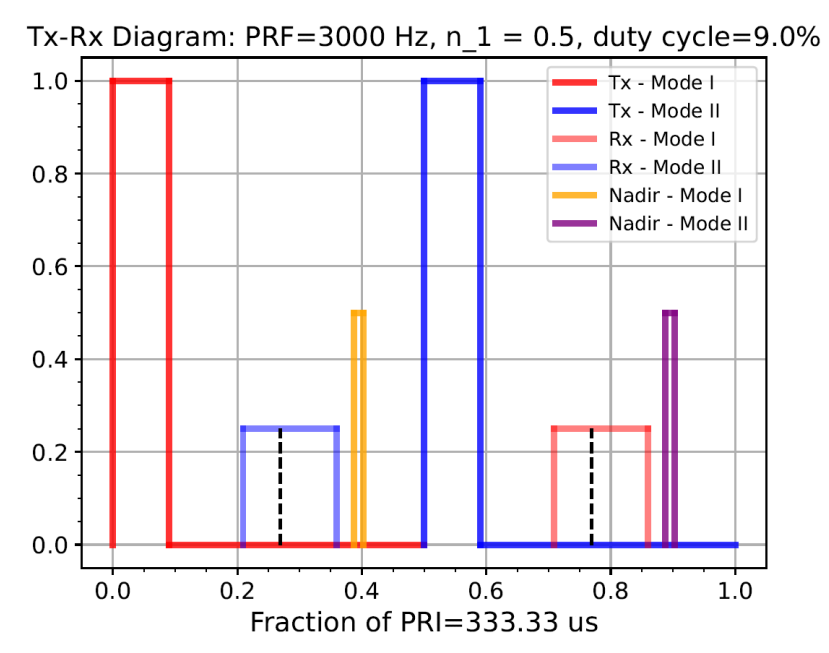


FIGURE 4.9 – Transmission diagram of a EST acquisition. Both scenes have a 5 km swath width, acquired at an incidence angle of $\theta_i = 37^{\circ}$, with PRF=3000 Hz and 9% duty cycle for each Tx pulse. There are no Tx nor Nadir pulses overlapping with any receiving signals, and each pulse is locked within a echo window. Each mode has an echo window that occupies 50% of the PRI (aside from the Tx Pulses).

4.5.3 Asymmetrical Concurrent Imaging

The scenario of Fig. 4.9 shows a symmetrical concurrent imaging, where both modes share an equal amount of the whole period (50 % for each echo window). But in Concurrent Imaging, however, there is one last possibility to be accounted for - the scenario where Modes 1 and 2 have **disproportionate echo windows**. In a Pulse Repetition Interval (PRI) of, say, 1000 μs , Mode 1 may use 300 μs and Mode 2 may use the remaining 700 μs .

This is the scenario of **asymmetrical concurrent imaging**, where Mode 1 and Mode 2 have each a fraction of the total PRI of the combined period. Let η_1 be the fraction of the PRI reserved for Mode 1. In this case, for asymmetrical imaging:

$$\frac{\eta_1}{\eta_2} = \frac{\eta_1}{1 - \eta_1} \neq 1 \Longleftrightarrow \eta_1 \neq 0.5 .$$

This asymmetry also impacts availability, since too narrow of a window for one mode may not be able to fit the whole scene of its respective mode, while leaving too much space for the other mode.

Asymmetrical concurrent imaging is an important feature when designing a concurrent acquisition - especially of two different scenes. Preserving a larger portion of the echo window to one mode may allow a larger image to be scanned in one mode than what a

symmetrical pulse share would allow, while also being possible to image a second smaller scene.

And as will be shown, setting non-symmetrical values to a pulse share of one mode can also redistribute ambiguity power between two scenes, especially in scenarios such as EST. While using a pulse setup where $\eta_1 = \eta_2 = 0.5$ will bring an acceptable and equal ambiguity power for both scenes, setting $\eta_1 = 0.48$ and $\eta_2 = 0.52$ may lead to lesser spurious power levels for mode 1, while increasing it for mode 2.

There are situations where this level of control may be useful, such as when imaging coastlines with EST. Regions with wide water bodies are far more susceptible to be visually dubious, as spurious power from the continent will overlap with regions such as oceans and lakes, leading to both landscapes meshing up. Fig. 4.10 displays a Stripmap acquisition done by TerraSAR-X of Piúma, in Brazil⁵.

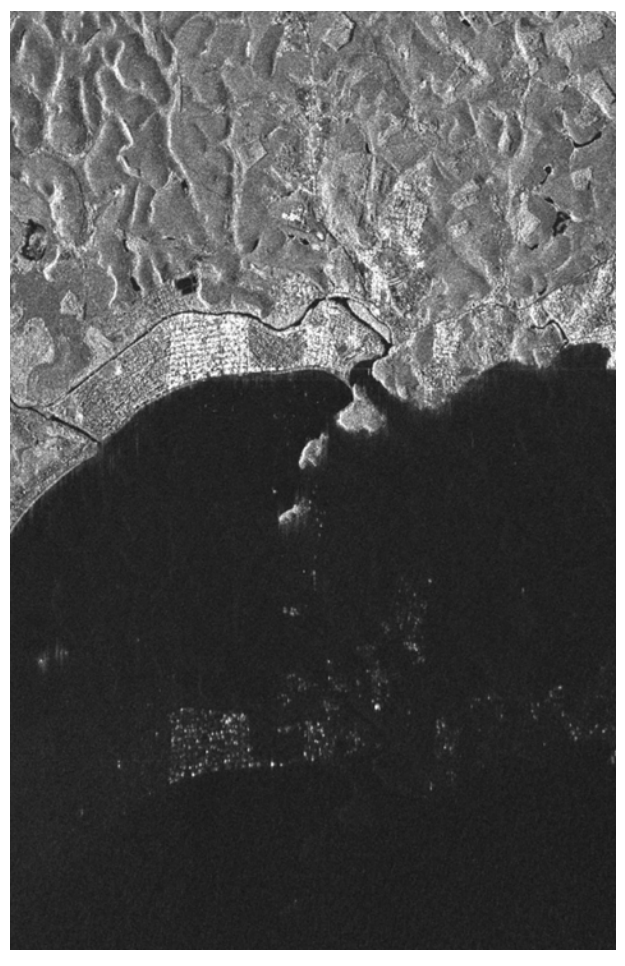


FIGURE 4.10 – Picture of a Stripmap acquisition of the city of Piúma, in Brazil, obtained by TerraSAR-X. Many bright spots can be seen outside of landmass, due to the ambiguous signals coming from the city, which overlap with the received signal of the ocean. This is an example of the necessity of minimizing ambiguity power as much as possible in SAR acquisitions. This image was extracted from (Ribeiro, 2021)

⁵J. P. T. Ribeiro, Concurrent Imaging Mode Design and Performance Prediction for Experimental SAR Acquisitions using TerraSAR-X, p.72.

If such regions were to be acquired leveraging EST, one could reduce the amount of ambiguous power on water bodies by shifting η_1 from 0.5 to 0.48, for example. This would increase ambiguity on the landmass portion of the extended scene, but reduce it on the water, which is visually more sensible - leading to a visually richer acquisition.

Due to the importance of analyzing assymetrical imaging, thence, instead of building a Tx Diagram, where the input parameters are PRF and θ_i , we build **PRF Maps**.

4.5.4 PRF Maps

PRF maps are diagrams which indicate the pairs of (η_1, PRF) that can acquire the scenes in tandem. They represent the *locus* of such pairs which are able to acquire two concurrent scenes, in their respective incidence angles $\theta_{i,1}$ and $\theta_{i,2}$, with no sort of interference whatsoever.

In Fig. 4.11, we build a PRF map for an EST acquisition (where both scenes have the same elevation, just juxtaposed in azimuth) where the extended scene has a 5 km swath width at an incidence angle of $\theta_i = 27^{\circ}$.

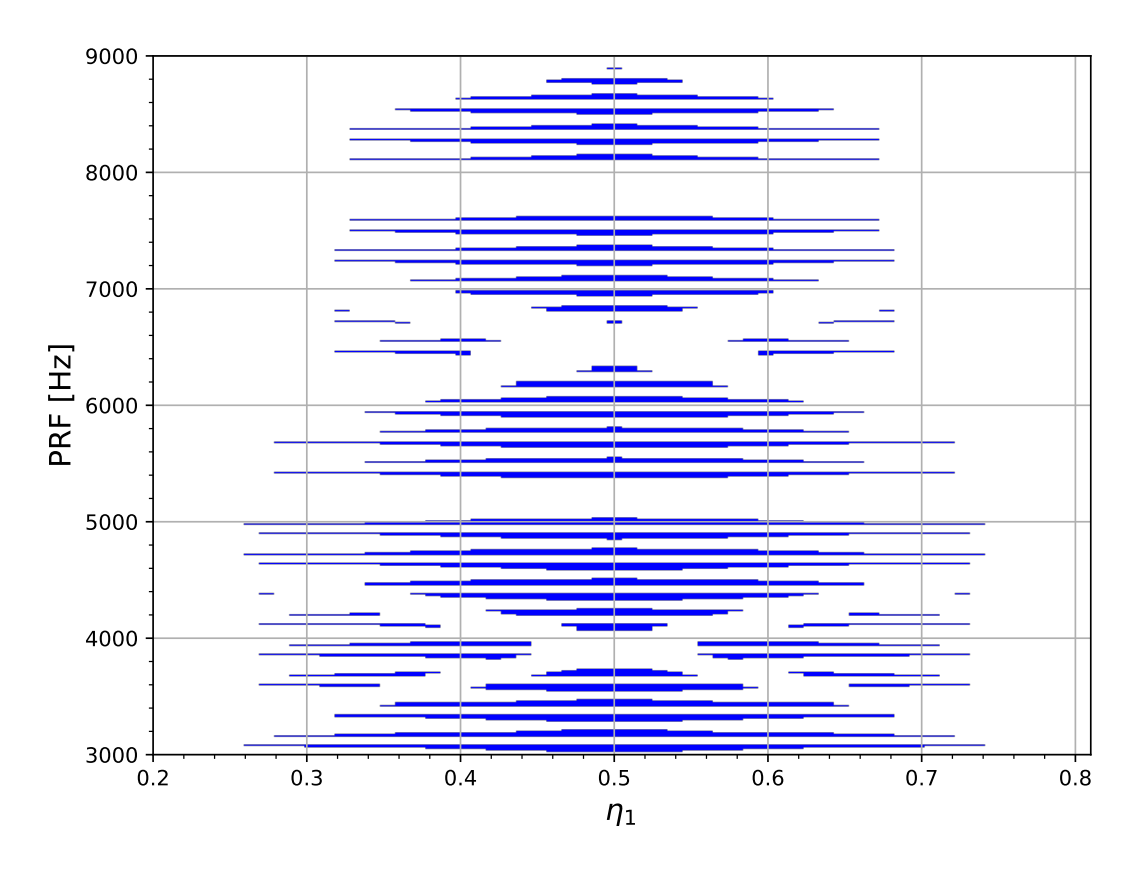


FIGURE 4.11 – Map of all the points which are capable of imaging an EST image at $\theta_i = 27^{\circ}$, with a swath width of 5 km (blue). Note how the majority of pairs which are able to concurrently acquired two ST images lie in the $\eta_1 = 0.5$ axis.

PRF maps are more convenient to build than Timing Diagrams when operating concurrent modes, as a designer may prefer to check, for a given θ_i , which configurations of a composite pulse will be able to acquire two scenes at once, given their placement on the ground. Additionally, as will be shown, one may iterate through all the (η_1, PRF) pairs where the acquisition is feasible to check whether the quality of the image at a particular pair is acceptable. In many cases, one may find other configurations of pulses which extract better images than the most trivial ones.

For every EST (or any Concurrent Imaging product), we need to build the diagram of Fig. 4.11, if either the swath width or the incidence angle changes.

Knowing which (η_1, PRF) pairs enable the extraction of an EST product, now it becomes necessary to analyze how does the acquisition fare in terms of image quality which to this thesis mainline revolves around calculating the spurious ambiguity power that each scene is infected with. By checking the amount of spurious power that overlaps with the image, we can deduct if it is able to use it.

When analyzing the total ambiguity power that is added to the target image power, the first step is extracting the range ambiguity throughout the scene.

4.6 Ambiguity Power

Although we mapped all the available points for a concurrent acquisition from a timing perspective in 4.5.4, this only provides information on whether the received signal could be feasibly accommodated within an echo window - if the received signal interferes with Tx or Nadir pulses. It does not verse on the quality of the image acquired, which is a critical point of concern when scanning a particular region of the ground and extracting an image out of it.

When ordering an acquisition, the designer must be aware of the obtainable levels of quality. In other words, the amount of spurious power interfering with the target image power must be known before ordering a satellite to point its antenna towards the region and start an EST (or any other kind of concurrent imaging technique).

The chosen method to assess and compute the amount of ambiguity power is the calculation of **Ambiguity Signal Ratio (ASR)**.

ASR encompasses the total amount of ambiguity power, whether it comes from RASR or AASR. For each valid pair (η_1, PRF) of a PRF map, we compute the total amount of spurious power throughout every pixel of the extracted image and check if it exceeds a determined threshold. If it does, in any pixel of the image whatsoever, the acquired image is deemed not sufficiently acceptable, hence this specific (η_1, PRF) pair is discarded.

If all pixels of the acquired image fit the minimum threshold, then the (η_1, PRF) pair is deemed acceptable, and the worst ASR value of the entire image is associated with its respective pair.

The worst ASR value is used as a metric to better inform a potential client. If one wishes to utilize a satellite to acquire an EST product under certain parameters, it is necessary to know which is the worst pixel of the acquired image, and if it fits a minimum threshold of quality. This is helpful to know, as it is a way of being certain that all of the image has a quality of at the very least the worst value presented.

When analyzing the total ambiguity power that is added to the target image power, the first step is extracting the range ambiguity throughout the scene.

4.6.1 Range Ambiguities Assessment

For every pair of Fig. 4.11, we create a frame (grid) of pixels to represent the image to be acquired. For each pixel, we calculate the total RASR using 3.15 and 3.16. By using 3.15, we are able to calculate which are the points on Earth's surface that emit interfering pulses, and their associated antenna gain. Via 3.16, the total RASR generated by all range ambiguities on the ground.

The generated image grid is built as represented in Fig. 3.6. For each resolution pixel, an RASR value is calculated and associated to it. Fig. 4.12 shows a simulation of the RASR values for a specific image of the ground, in a grid of 400 by 400 pixels.

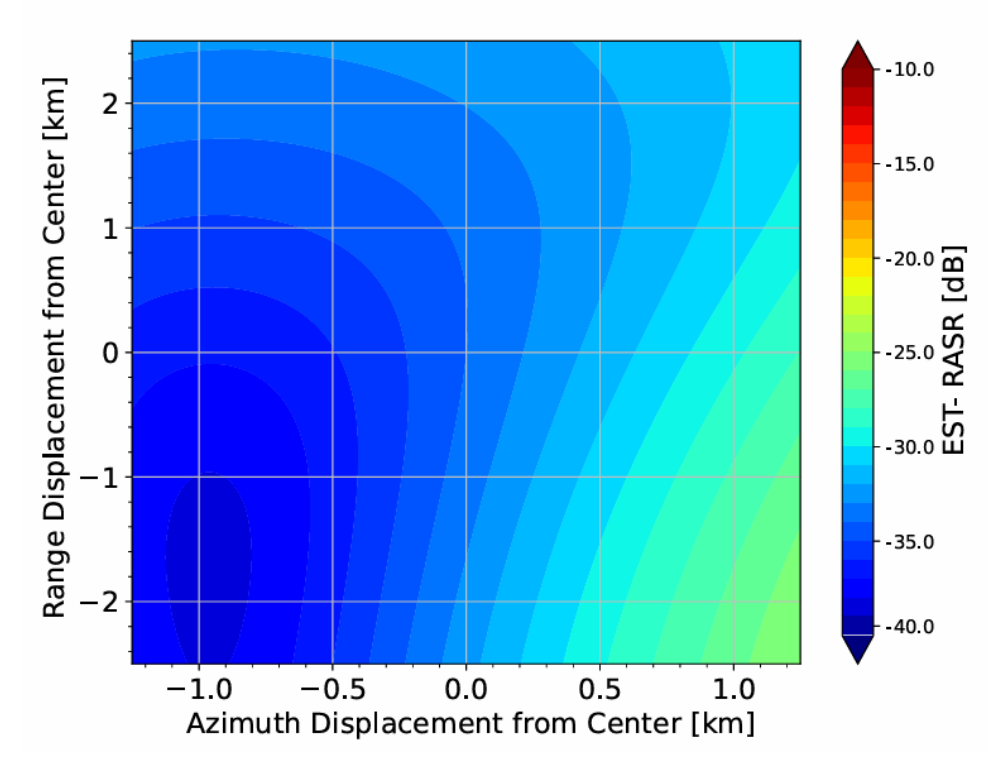


FIGURE 4.12 – Simulation for the RASR of an Extended Staring Spotlight image, which is 2.5 km in azimuth and 5.0 km in elevation (only half of the scene is present). This was collected for an incidence angle of $\theta_i = 27^{\circ}$, $\eta_1 = 0.5$, and PRF = 5000 Hz. In the particular case of this simulation, a grid of 400x400 pixels was built, and each one is associated with a specific value of RASR. All values of ambiguous power are in dB.

For the simulation of Fig. 4.12, the worst RASR value is -25.4 dB. So we take note and associate the pair $(\eta_1, PRF) = (0.5, 5000 \text{ Hz})$ to -25.4 dB in the PRF map of Fig. 4.11.

This procedure is repeated for every single pair which provides timing availability in Fig. 4.11, and the result is displayed in Fig. 4.13.

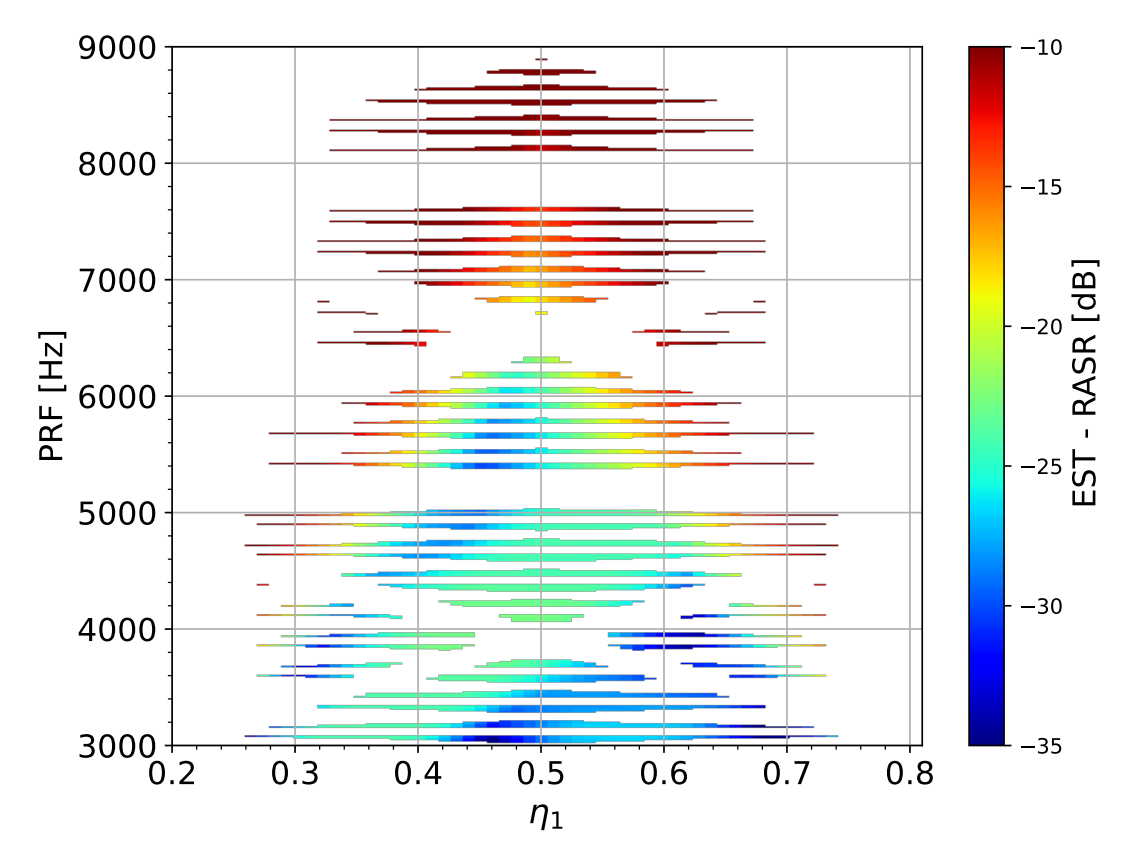


FIGURE 4.13 – PRF map of Fig. 4.11, with each pair of parameters associated with the worst extractable RASR value of the EST image (first half of the extended scene). The EST acquisition is done at 27 degrees of incidence angle and has a swath width of 5 km.

This iteration generates a complete PRF map with all RASR values extracted for that particular direction of acquisition ($\theta_i = 27^{\circ}$) and acquisition swath width (5 km). Note that the map was extracted for the first half of the extended scene (first 2.5 km azimuthwise), as the diagram for the remaining 2.5 km is the same as Fig. 4.13, but mirrored around the $\eta_1 = 0.5$ vertical line. This behavior concerns all subsequent maps built in this thesis - RASR, AASR or ASR.

4.6.2 Azimuth Ambiguities Assessment

In similar fashion to what is done to range ambiguities, we must analyze the behavior of Azimuth Ambiguities and their power spread throughout the scene. After this is done, we grab the worst value displayed on the grid, and associate it to the respective (η_1 , PRF) pair.

Fig. 4.14 depicts the result of a simulation which executes an Extended Staring Spotlight, with 5 km swath width and 5 km of extended azimuth length (only the first 2.5 km are shown), at $\theta_i = 27^{\circ}$. We utilize $\eta_1 = 0.5$ and PRF = 6500 Hz for this example.

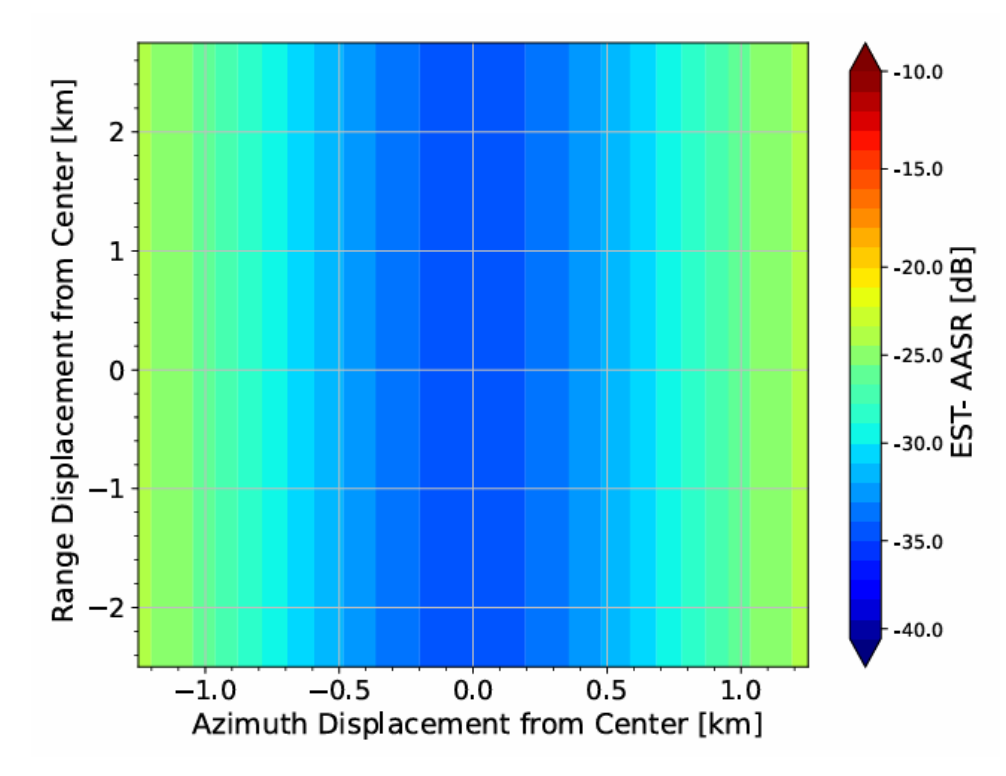


FIGURE 4.14 – Distribution of ambiguous power (AASR) coming from azimuth ambiguities throughout the first half of the extended scene. The AASR is shown in dB, and it is approximately symmetrical at x = 0, since range differences in distance do not alter the influence of azimuth ambiguities. The worst values of azimuth ambiguities will always be symmetrically at the boarders. For this particular simulation, the worst AASR value of the whole grid is -24 dB.

For this particular scenario, the worst AASR value throughout the whole scene is around -24 dB. We associate this value with the respective $(\eta_1, PRF) = (0.5, 6500 \text{ Hz})$.

As done in the previous section, we do this procedure for every single pair of (η_1 , PRF) in the correspondent PRF map that can accommodate the EST acquisition at the detailed specifications of swath width, extended azimuth length and incidence angle.

The result is the image in Fig. 4.15, where all pairs in the PRF map are associated with the worst extracted AASR value encountered throughout their respective pixel grids.

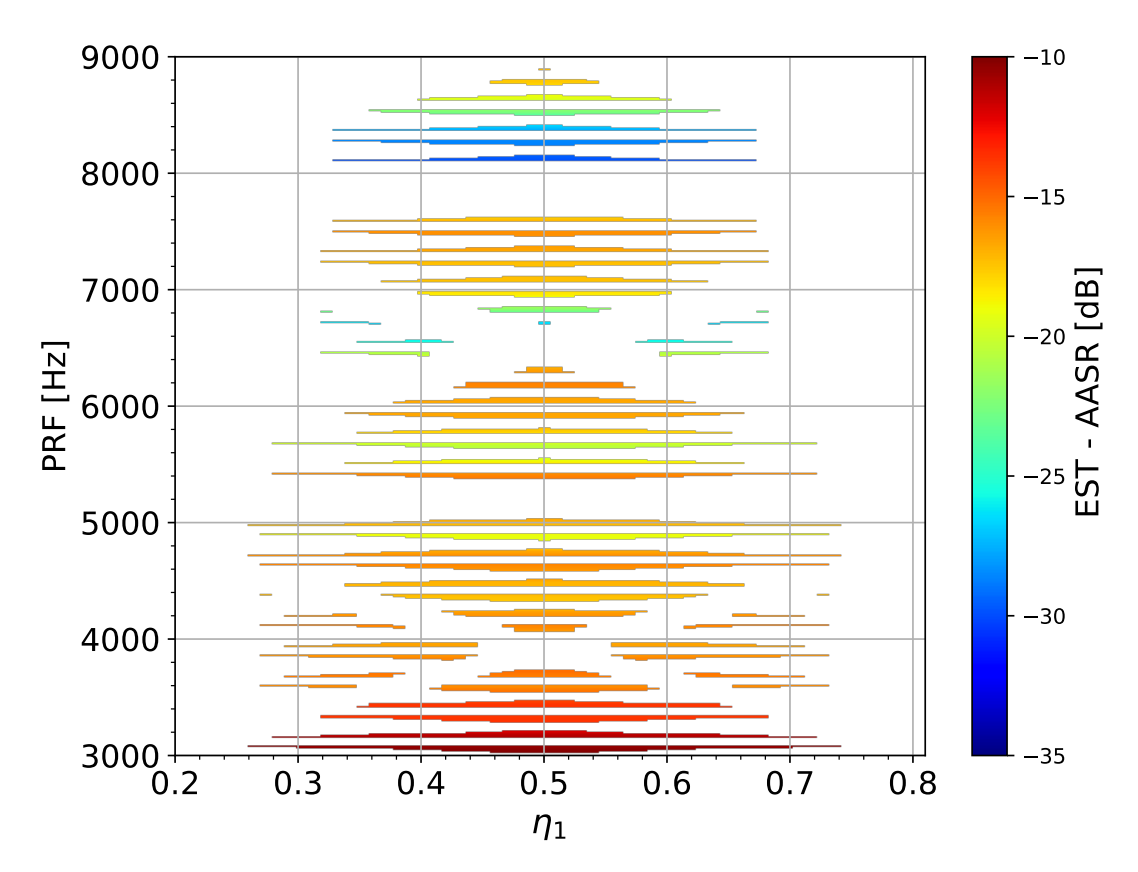


FIGURE 4.15 – AASR map built from associating every pair of Fig. 4.11 with the worst AASR value extracted from the respective image grid. For any kind of Staring Spotlight acquisition, as PRF increases the AASR quality of the image tends to increase. Note how the AASR value does not change with a variation of η_1 .

In the case of AASR, since azimuth ambiguities come from a coincidence in frequency, changing η_1 only alters the shape of the pulse in time, but the frequency experienced from each mode is the same, regardless of it. Hence, Fig. 4.15 shows no variation of AASR due to a modification of η_1 .

4.6.3 Ambiguity Signal Ratio

Having both RASR and AASR calculated, we now sum both of them to obtain the general **Ambiguity-to-Signal Ratio** (**ASR**)⁶.

The reader may have realized how RASR maps and AASR maps, although similar, do change in behavior reasonably. The former is not symmetrical to η_1 , while the latter is. In the same manner, the former degrades as PRF increases, whilst the latter does the

⁶We incur in a small error when summing directly the values of RASR and AASR for a specific (η_1 , PRF). This imprecision arises from the fact that the position on the scene where the worst value of RASR is located does not necessarily match the position of worst value of AASR on the same grid. The total ASR calculated will be, thence, a bit bloated, but it is sufficient for the proof of concept of this thesis.

opposite. This leads to a situation where the total ambiguity power will be minimal at the core of an EST ambiguity map. In other words, the designer will need to evaluate a sweet spot for the acquisition to be fruitful.

ASR measures the total ambiguity power regardless of its origin. This is important, since when concerning image quality, any kind of ambiguity will mesh the intended image to be acquired with overlapping, non-desirable scans of different spots on the ground.

Fig. 4.16 depicts the ASR map - the combination of RASR map (Fig. 4.13) and AASR map (Fig. 4.15) - where the total amount of ambiguous power is computed.

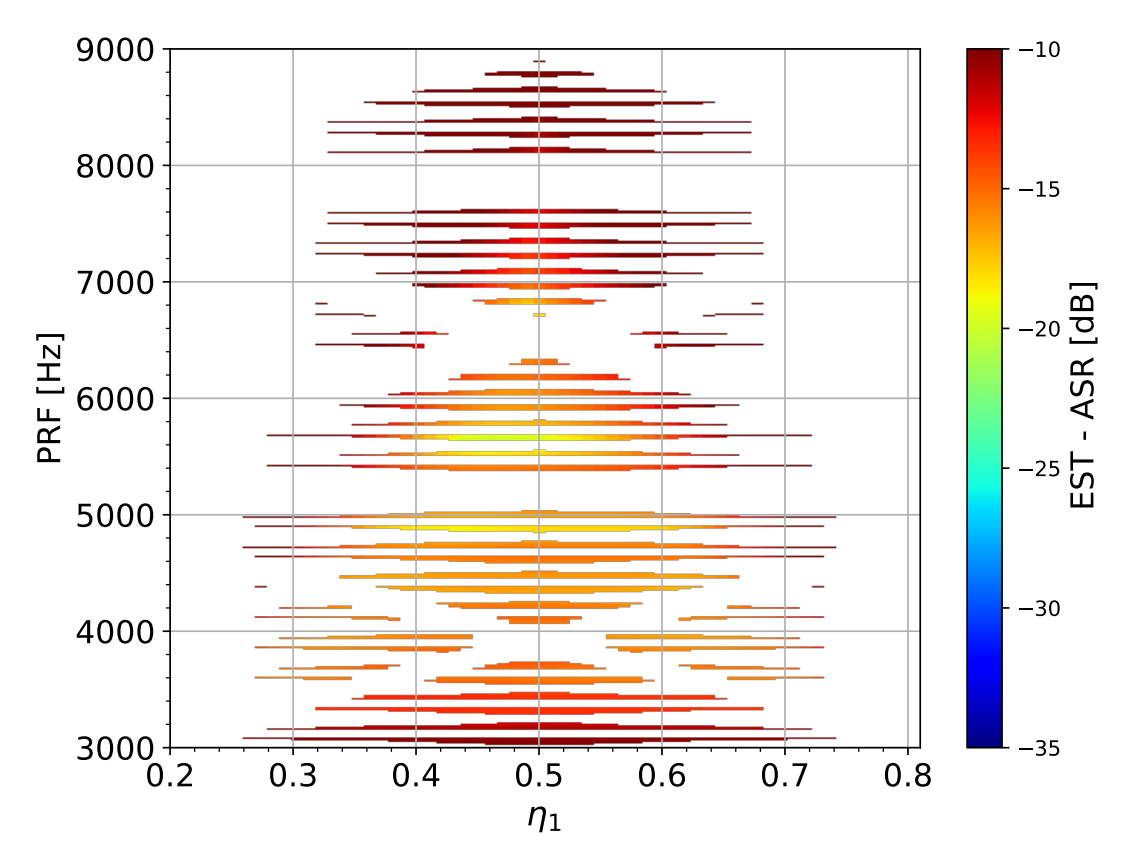


FIGURE 4.16 – ASR map, obtained by summing all ambiguities which overlap with the intended scene (RASR and AASR maps are combined). Notice how almost all points on the map yield far too high of an ambiguity power to be considered suitable to an acquisition, since the majority of them are in the red-orange color scheme. Still, there is a wide collection of points with reasonable quality (yellow-green range) which can be utilized to acquire an EST product as specified.

It is noticeable in Fig. 4.16 how almost all pairs are not suitable for an EST acquisition. This is natural, since in this methodology we are summing both kinds of ambiguity power. In particular, ASR becomes far too high for high PRF values - due to an increase in the number of range ambiguities - but also for low PRF values - due to an increase in azimuth ambiguities and narrower processing window. In other words, there will be more chance of encountering a suitable (η_1 , PRF) pair on the map if we analyze it around its core, in

the yellow zones.

The final step is filtering the whole ASR map, using a specific threshold of maximum spurious power tolerable as metric.

If at the very least one pair remains after filtering, then the Extended Staring Spotlight acquisition is considered doable at that θ_i with the required specifications of swath width and extended azimuth length.

4.6.4 Threshold filtering

ASR on itself is unavoidable, but it can be minimized. SAR-equipped systems tend to establish a maximum amount of accepted ambiguity power for an image to be deemed suitable for commercial purposes. TerraSAR-X, for example, establishes a limit of -17 dB for AASR power and -20 dB for RASR power.

In this thesis, in order to simplify the analysis and attest the proof of concept of the Extended Staring Spotlight, we'll sum both ambiguity criteria as a common threshold.

$$ASR_{thr} = RASR_{thr} + AASR_{thr}$$
,
 $ASR_{thr} = -17 \text{ dB} + -20 \text{ dB}$,
 $\therefore ASR_{thr} = -15.2 \text{ dB}$.

We'll approximate the ASR threshold to -15.5 dB, with this being the maximum amount of ambiguous power for an image to be considered acceptable. However, we'll run the analysis with -17 dB as the threshold which ensures an image to be of decent quality, not just acceptable.

Therefore, for every (η_1, PRF) pair on the ASR map of Fig. 4.16, we'll check whether the total ambiguity power detected is lower or higher than -17 dB. If it is higher, this pair will be excluded from the collection, not being considered suitable for an EST acquisition.

The result of this analysis is shown in Fig. 4.17.

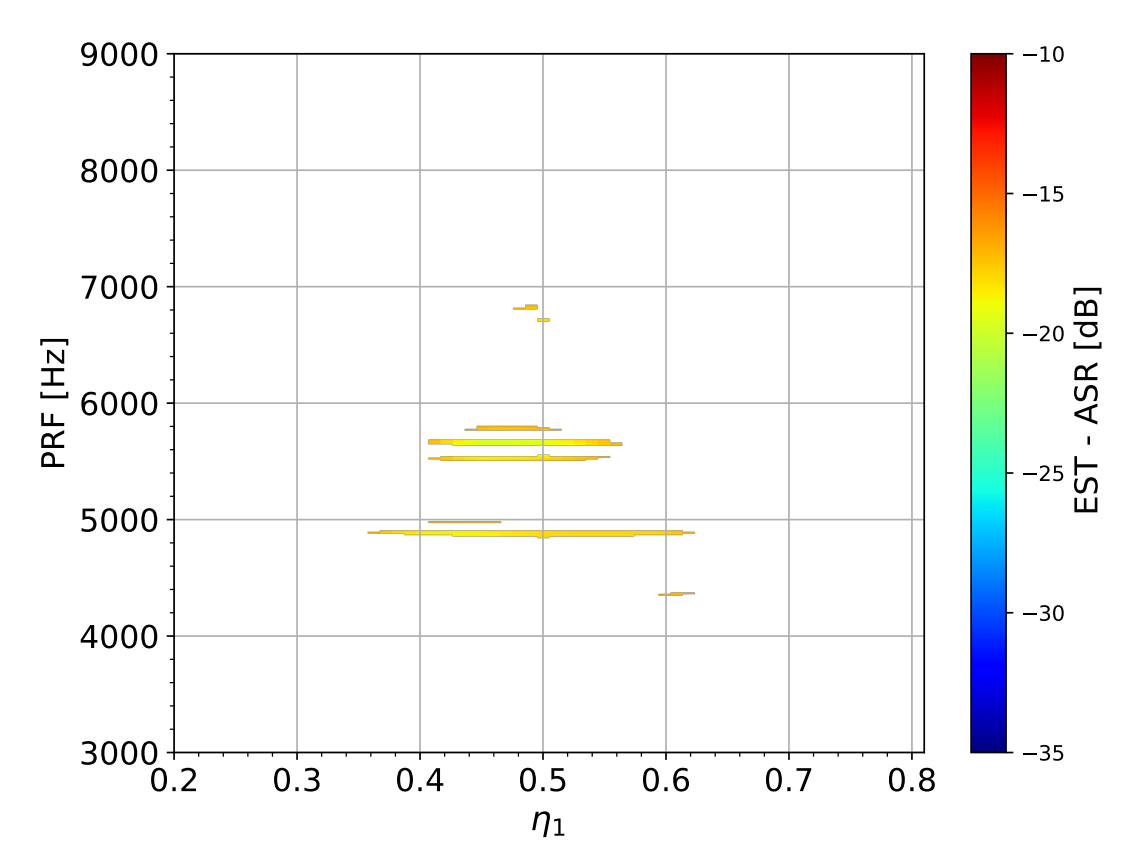


FIGURE 4.17 – Collection of pairs whose ambiguity power is lower than -17 dB, therefore being considered suitable for an EST acquisition of 5 km swath width, 5 km extended azimuth length, at $\theta_i = 27^{\circ}$.

Fig. 4.17 displays all pairs whose undesired power is less than -17 dB when compared to the target scene's received power. In other words, it is the *locus* of the EST acquisition for that particular set of geometric parameters: 5 km swath width, 5 km extended azimuth length, and $\theta_i = 27^{\circ}$.

However, as it is clear, not all these pairs have the same ambiguity power. Some are more suitable, while others are more spurious. Which point will be selected depends on many constraints, such as:

- The maximum composite PRF the satellite system is capable of producing;
- Whether the designer wishes to reduce ambiguities on one half of the extended scene, but doesn't care much about the ambiguity levels on the second half of the extended scene;

In general, it is in the best interest of the client to extract the best quality in general (both halves of the extended scene), so the pair to be extracted would be whichever PRF that minimizes ASR at $\eta_1 = 0.5$. In the particular scenario of Fig. 4.17, at $\theta_i = 27^{\circ}$, 5

km swath width and 5 km of extended azimuth length in an EST acquisition, it would be $(\eta_1, PRF) = (0.50, 5680 \text{ Hz})$, yielding -19.6 dB in ASR throughout the whole extended scene.

If, however, it is in the interest of the designer to minimize ASR in the first half of the extended scene, thence one must pick the pair on the filtered ASR map that yields the lowest ASR value, as such map refers to the ASR calculated to the first mode of the EST acquisition. In Fig. 4.17, this would be the pair $(\eta_1, PRF) = (0.46, 5680 \text{ Hz})$, yielding -19.9 dB in ASR in the first half of the extended scene (mode 1), but leading to a -18 dB ASR level on the second half of the extended scene (mode 2).

4.7 Implementation

The core implementation of the methodology exposed is established for all possible incidence angles of an acquisition spectrum.

For TerraSAR-X, its full-performance of acquisition is done at the range of incidence angles from 20° to 45°, according to its product specifications⁷. To study the feasibility of the Extended Staring Spotlight, we'll use this range as a benchmark, checking for all possible incidence angles within this range whether an EST acquisition attempt yields fruitful images.

The general results are presented in the next chapter.

⁷TerraSAR-X Basic Product Specification, DLR, 2013.

5 General Results

The main purpose of this work is to prove the feasibility of the Extended Staring Spotlight as an acquisition technique, aiming to double the azimuth length of the acquired image and the total area of the acquisition when compared to a conventional Staring Spotlight mode.

In order to do so, we've established a workflow as a methodology to analyze whether a given scene - which measures 5 km in swath width and 5 km in extended azimuth length in our test-bench scenario, but could measure differently - could be acquired at a particular incidence angle θ_i , with ideally less than -17 dB of ambiguous power overlapping with the target image signal.

With a given workflow ready for a particular θ_i , all there is left is to analyze at which angles the Extended Staring Spotlight technique yields decent acquisitions, providing to an interested client or designer the possibility of executing this new mode for imaging larger areas than conventional ST, but with its high resolution and with decent levels of ambiguity power. Additionally, we keep track of the parameters of such acquisitions (η_1 , PRF, ASR) to inform the client of which input parameters must be used to achieve the desired quality level of ASR.

Using the full-performance range of incidence angles of TerraSAR-X (SM mode angle range), we simulate all the parameters and quality data as detailed in the methodology workflow for all incidence angles between 20° and 45°, at a step of 0.5°.

After simulation, the core results are subdivided into four main tables. Table 5.1 displays the ASR and necessary PRF values for each incidence angle when utilizing $\eta_1 = 0.5$ (symmetrical concurrent imaging), from 20.0° to 35.0°, while Table 5.2 shows the results from 35.5° to 45.0°. Table 5.3 compiles the data for a designer who wishes to minimize ASR in the first half of the extended scene - that is, using any η_1 values which extract the best possible quality, regardless of distribution throughout the extended image - from 20.0° to 35.0°, while Table 5.4 continues the data from 35.5° to 45.0°.

θ_i [°]	PRF [Hz]	ASR [dB]
20.0	8000	-24.4
20.5	7960	-23.9
21.0	8060	-21.0
21.5	8060	-20.1
22.0	6640	-23.0
22.5	6640	-18.0
23.0	6640	-23.7
23.5	6620	-23.5
24.0	4040	-15.5
24.5	6620	-18.2
25.0	6680	-17.9
25.5	6620	-21.8
26.0	6600	-20.8
26.5	6600	-16.0
27.0	5680	-19.6
27.5	5140	-15.4
28.0	5660	-19.5
28.5	5180	-16.0
29.0	4940	-18.3
29.5	4500	-16.2
30.0	4900	-18.7
30.5	4860	-18.7
31.0	4980	-17.4
31.5	4820	-18.1
32.0	4940	-18.0
32.5	4860	-17.7
33.0	4020	-15.9
33.5	4320	-17.6
34.0	4340	-17.5
34.5	4340	-17.5
35.0	4320	-17.0

TABLE 5.1 – Table results of simulations for an EST acquisition, with 5 km of swath width and 5 km in total azimuth length. Until 35°, the ambiguity quality is below the minimum quality threshold of -17 dB. Precision: $(\Delta \eta_1, \Delta PRF, \Delta ASR = \pm 0.01, \pm 10~Hz, \pm 0.2~dB)$.

θ_i [°]	PRF [Hz]	ASR [dB]
35.5	4320	-17.0
36.0	3880	-16.4
36.5	3880	-16.3
37.0	3600	-16.0
37.5	3600	-16.0
38.0	3540	-15.7
38.5	3620	-15.5
39.0	3600	-15.4
39.5	3580	-15.1
40.0	3560	-14.9
40.5	3300	-14.5
41.0	4340	-17.5
41.5	3300	-14.1
42.0	4320	-17.0
42.5	3260	-13.6
43.0	3240	-13.2
43.5	3180	-12.6
44.0	3260	-12.4
44.5	3020	-11.9
45.0	3320	-7.5

TABLE 5.2 – Table results of simulations for an EST acquisition, with 5 km swath width and 5 km total azimuth length. After 35°, the ambiguity power struggles to hit the quality threshold of -17 dB, and after 40° not even the minimum tolerable limit of -15.5 dB. Precision: $(\Delta \eta_1, \Delta PRF, \Delta ASR = \pm 0.01, \pm 10 \text{ Hz}, \pm 0.2 \text{ dB})$.

θ_i [°]	η_1	PRF [Hz]	ASR [dB]
20.0	0.45	8100	-26.2
20.5	0.46	7960	-25.8
21.0	0.48	8060	-23.1
21.5	0.48	8060	-22.1
22.0	0.45	6660	-24.8
22.5	0.48	8100	-19.3
23.0	0.46	6640	-25.3
23.5	0.46	6620	-25.2
24.0	0.6	4560	-16.2
24.5	0.48	6620	-18.6
25.0	0.48	6680	-18.8
25.5	0.48	6620	-23.1
26.0	0.47	6600	-22.2
26.5	0.44	5160	-16.0
27.0	0.48	5680	-19.9
27.5	0.46	5140	-15.8
28.0	0.48	5660	-20.0
28.5	0.46	5180	-16.1
29.0	0.46	4940	-18.7
29.5	0.44	4500	-16.3
30.0	0.48	4900	-18.9
30.5	0.5	4860	-18.7
31.0	0.46	4340	-17.8
31.5	0.46	4820	-18.4
32.0	0.48	4940	-18.2
32.5	0.48	4860	-18.4
33.0	0.48	4020	-16.1
33.5	0.48	4320	-17.8
34.0	0.48	4340	-17.8
34.5	0.48	4340	-17.8
35.0	0.48	4320	-17.5

TABLE 5.3 – Table results of simulations for an EST acquisition, with 5 km of swath width and 5 km in total azimuth length. This table displays the necessary η_1 to achieve maximum image quality at the first half of the extended scene, but not for the entire picture. Until 35°, the ambiguity quality is below the minimum quality threshold of -17 dB. Precision: $(\Delta \eta_1, \Delta PRF, \Delta ASR = \pm 0.01, \pm 10 \text{ Hz}, \pm 0.2 \text{ dB})$.

θ_i [°]	η_1	PRF [Hz]	ASR [dB]
35.5	0.48	4320	-17.5
36.0	0.48	3860	-16.6
36.5	0.48	3860	-16.5
37.0	0.48	3600	-16.1
37.5	0.48	3600	-16.1
38.0	0.48	3880	-15.9
38.5	0.48	3620	-15.8
39.0	0.48	3600	-15.7
39.5	0.48	3580	-15.5
40.0	0.48	3560	-15.2
40.5	0.48	3300	-14.8
41.0	0.48	4340	-17.8
41.5	0.48	3280	-14.4
42.0	0.48	4320	-17.5
42.5	0.5	3260	-13.6
43.0	0.48	3240	-13.2
43.5	0.5	3180	-12.6
44.0	0.5	3260	-12.4
44.5	0.5	3020	-11.9
45.0	0.52	3320	-7.6

TABLE 5.4 – Table results of simulations for an EST acquisition, with 5 km of swath width and 5 km in total azimuth length. This table displays the necessary η_1 to achieve maximum image quality at the first half of the extended scene, but not for the entire picture. After 35°, the majority of sampled incidence angles does not fit the quality threshold of -17 dB. After 40°, the minimum threshold of -15.5 dB is not met as well, aside from some specific directions. Precision: $(\Delta \eta_1, \Delta PRF, \Delta ASR = \pm 0.01, \pm 10 \text{ Hz}, \pm 0.2 \text{ dB})$.

The subdivision of the full-performance range of TerraSAR-X into two different sections (20°-35°, 35°-45°) is done not just to fit the tables within page template (officially), but also show more clearly the distinction between two different trends in the EST ambiguity power yield.

Until 35°, aside from some exceptions, all incidence angles respect the quality threshold of -17 dB, with particular attention to the [20°, 23.5°] and [24.5°, 26°] ranges, which provide the best quality of ASR by far, below the -20 dB of ambiguity power - or less than 1% of spurious power overlap.

However, after the 35° incidence angle mark, the levels of ASR struggle to meet the minimum -17 dB quality threshold, excluding some niche exceptions. After 40°, even the minimum tolerable limit of -15.5 dB is not sufficiently met, leading to unacceptable levels of spurious power.

Fig. 5.1 summarizes in a plot the general trend of the Extended Staring Spotlight in terms of minimum extractable ASR for all the incidence angles within TerraSAR-X's full-performance angle range.

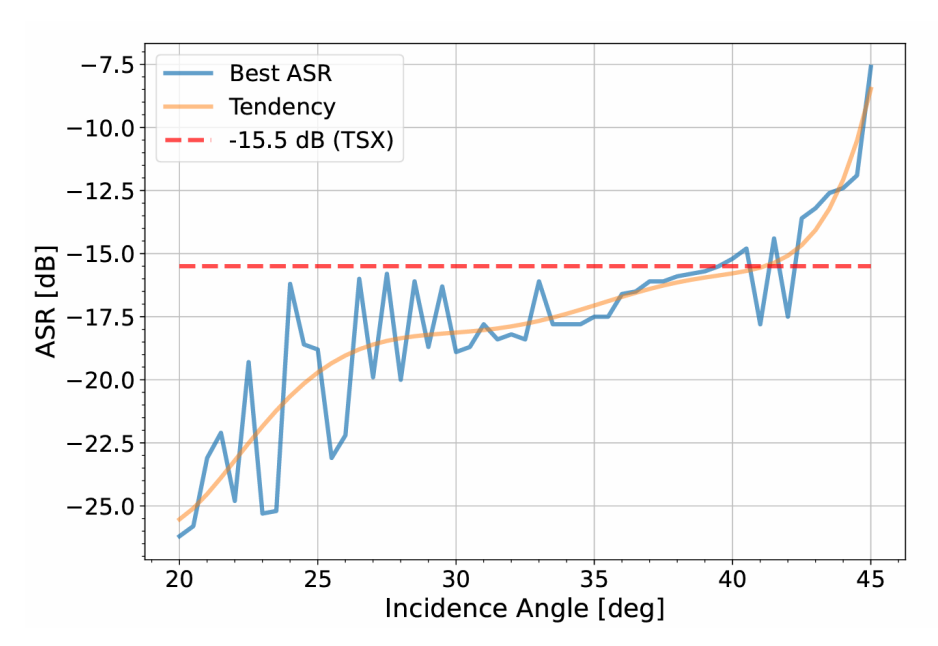


FIGURE 5.1 – Best extractable ASR (in blue) utilizing the Extended Staring Spotlight method to acquire an extended scene of 5 km swath width by 5 km composite azimuth length, for all incidence angles within TerraSAR-X's full-performance span. The data is presented along with a tendency curve (in orange), which depicts the upward trend of the ambiguity power. The minimum threshold of -15.5 dB (in red) is satisfied by all incidence angles below 40°, proving the feasibility of the EST method for a variety of scenarios.

Fig. 5.1 shows how all incidence angles up to 35° (with a few exceptions) yield EST images with less than -17 dB of overlapping ambiguity power, and almost all until 40° respect the minimum threshold of -15.5 dB.

We can say, therefore, that the Extended Staring Spotlight mode is feasible, allowing a client to request twice the same amount of area than what a conventional Staring Spotlight technique would yield, while maintaining high resolution and containing ambiguity power to a tolerable amount, which was the goal of this thesis.

Additionally, the necessary parameters to achieve such levels of quality are documented in Tables 5.1, 5.2, 5.3, and 5.4, providing the ways of acquiring EST products that resemble the quality levels simulated.

6 Conclusion

In this thesis, **the Extended Staring Spotlight was presented**. The extension of the azimuth length and acquired area to twice the size of the conventional Staring Spotlight mode can be done while preserving its high resolution.

For many incidence angles within the range of $20^{\circ} \leq \theta_i \leq 45^{\circ}$, a test workflow was implemented for each incidence angle analyzed, for an extended scene of 5 km swath width and 2×2.5 km of extended azimuth length.

Due to the limitations of TerraSAR-X, an acquisition of the Extended Staring Spotlight would not be feasible, so all data were simulated.

The simulated data showed that, for an acquisition height of 519 km, all angles up to 40° present less than -15.5 dB of ambiguity power (roughly 3% of spurious power), and most until 35° yield less than -17 dB (or 2% of spurious power). Finally, with some care to oscillation, the 20°-24° incidence angle range yields less than -20 dB (1%).

The results demonstrate the practical feasibility of the Extended Staring Spotlight as an acquisition method, being able to acquire twice the coverage of the traditional ST method but still yielding acceptable to excellent levels of image quality.

All the necessary pulse configurations for these quality parameters being extractable were compiled in Chapter 5 for the particular case of TerraSAR-X, located at 519 km of Earth's surface, for the 5 x 5 km scene proposed. This compilation allows a designer to reproduce these experiments under these restrictions, although for different constraints the methodology of Chapter 4 needs to be applied from the beginning for all incidence angles of interest.

Further possibilities for this work could include Cross-Nadir interference filtering techniques, to acquire more (η_1 , PRF) pairs and achieve better performance. Another possibility is to analyze the variations, such as an Extended Sliding Spotlight (ESL) or a deeper study into the Continuous Staring Spotlight (CST), both commented in the conference paper¹.

¹L. F. S. R. Soares, J. P. T. Ribeiro, T. Kraus and M. Bachmann, "An Extended Staring Spotlight Mode Enabled by Concurrent Imaging," 2025 IEEE Radar Conference (RadarConf25), Krakow, Poland, 2025, pp. 508-513

References

- BALANIS, C. A. **Antenna Theory Analysis and Design**. 2nd. New York: John Wiley Sons, Inc., 1997. Cit. on p. 40.
- CALABRESE, D. DIscrete Stepped Strip (DI2S). *In:* EUROPEAN CONFERENCE ON SYNTHETIC APERTURE RADAR, 10., 2014, Berlin, p. 1–4. Cit. on p. 78.
- CURLANDER, J. C.; MCDONOUGH, R. N. **SYNTHETIC APERTURE RADAR Systems and Signal Processing**. 1st. New York: John Wiley Sons, Inc., 1991. Cit. on p. 75.
- J. MITTERMAYER S. WOLLSTADT, P. P.-I.; SCHEIBER, R. The TerraSAR-X Staring Spotlight Mode Concept. **IEEE Transactions on Geoscience and Remote Sensing**, v. 52, n. 6, p. 3695–3706, June 2014. Cit. on p. 73.
- L. F. S. R. SOARES J. P. T. RIBEIRO, T. K.; BACHMANN, M. An Extended Staring Spotlight Mode Enabled by Concurrent Imaging. *In:* IEEE RADAR CONFERENCE (RADARCONF25), 10., 2025, Krakow, p. 508–513. Cit. on p. 24.
- M. VILLANO, G. K.; MOREIRA, A. Nadir Echo Removal in Synthetic Aperture Radar via Waveform Diversity and Dual-Focus Postprocessing. **IEEE Geoscience and Remote Sensing Letters**, v. 15, n. 5, p. 719–723, May 2018. Cit. on p. 82.
- RIBEIRO, J. P. T. Concurrent Imaging Mode Design and Performance Prediction for Experimental SAR Acquisitions using TerraSAR-X. 2021. Bachelor Thesis Aeronautics Institute of Technology, São José dos Campos, Brazil. Cit. on p. 92.
- SULLIVAN, R. J. Radar Foundations for Imaging and Advanced Concepts. 2nd. New York: SciTech Publishing, 2004. Cit. on p. 40.

	FOLHA DE REGISTI	RO DO DOCUMENTO		
1. CLASSIFICAÇÃO/TIPO TC	2. DATA 11 de novembro de 2025	3. DOCUMENTO Nº DCTA/ITA/TC-046/2025	^{4.} № DE PÁGINAS 111	
5. TÍTULO E SUBTÍTULO: Extended Staring Spotlight	- A new SAR method of acq	uisition via Concurrent Imag	ing	
6. AUTOR(ES): Luis Felipe Silva Rezende S	oares			
7. INSTITUIÇÃO(ÕES)/ÓRGÃ Instituto Tecnológico de Ae	O(S) INTERNO(S)/DIVISÃO(ÕI ronáutica – ITA	ES):		
8. PALAVRAS-CHAVE SUGER EST; Spotlight; SAR; Conc				
(planeta); Processamento de 10. APRESENTAÇÃO: ITA, São José dos Campos	; Processamento de imagens; e dados; Engenharia eletrônic . Curso de Graduação em E	(X) ngenharia Eletrônica. Orient	Nacional () Internacional	
ITA, São José dos Campos. Curso de Graduação em Engenharia Eletrônica. Orientador: Prof. Dr. Renato Machado; coorientador: João Pedro Turchetti Ribeiro. Publicado em 2025. 11. RESUMO: Within the field of Synthetic Aperture Radar (SAR), its use for acquiring detailed images on Earth's surface has always been constrained by a particular trade-off - the one between maximum obtainable area and finest possible resolution. Techniques such as ScanSAR can achieve wide swaths of land but degrading significantly image resolution, while other methods such as Staring Spotlight yield detailed images with extremely limited surface area. With the usage of a novel pulse emitting technique - Concurrent Imaging - this thesis proposed and proves the feasibility of the Extended Staring Spotlight (EST): a new acquisition mode which yields double the size of a conventional Staring Spotlight scene, while maintaining its high-level of detail throughout the image.				
12. GRAU DE SIGILO: (X) OSTENS	IVO () RESER	EVADO () SEC	RETO	